université PARIS-SACLAY

Nucleon structure studies with CLAS at Jefferson Lab: Deeply Virtual Compton Scattering on nitrogen

Thèse de doctorat de l'université Paris-Saclay

École doctorale n°576 : Particules, Hadrons, Énergie et Noyau : Instrumentation, Image, Cosmos et Simulation (PHENIICS)
Spécialité de doctorat : Physique hadronique
Unité de recherche : Université Paris-Saclay, CNRS, IJCLab, 91405, Orsay, France
Référent : Faculté des sciences d'Orsay

Thèse présentée et soutenue à Paris-Saclay, le 7 juillet 2021, par

Mathieu EHRHART

Composition du Jury

Béatrice RAMSTEIN Directrice de recherche, Université Paris-Saclay	Présidente
Lamiaa EL FASSI Professeure, Mississippi State University	Rapporteur & Examinatrice
Stepan STEPANYAN Professeur, Old Dominion University	Rapporteur & Examinateur
Sergio SCOPETTA Professeur, Università degli Studi di Perugia	Examinateur

Direction de la thèse

Raphaël DUPRÉ Chargé de recherche, Université Paris-Saclay	Directeur de thèse
Zein-Eddine MEZIANI Senior Scientist, Argonne National Laboratory	Co-Encadrant de thèse

Thèse de doctorat

NNT : 2021UPASP052

À mes grands-parents

Acknowledgments

Here it is, the end of a journey. As with any adventure, the path taken is not always a flat and straight line. This journey took me to different places where I had the chance to be accompanied by incredible friends.

First and foremost, I would like to thank all the members of the jury, Lamiaa El Fassi, Stepan Stepanyan, Béatrice Ramstein, and Sergio Scopetta, for their time reviewing this thesis, as well as for their insightful comments and questions during the defense.

I cannot continue without giving my sincere gratitude to my thesis director Raphaël Dupré. From our first meeting as a bachelor student at Jefferson Laboratory to the smuggling of delicacies from Normandy into Newport News, and finally, these past few years at Orsay; thank you for being patient and for your continuous support during this adventure.

I am extremely thankful to Zein-Eddine Meziani for his supervision and for welcoming me to Argonne National Laboratory, where I had the chance to work among distinguished scientists and learned a lot. Thank you to everyone in the Medium Energy Physics group, especially Whitney Armstrong and Sylvester Joosten, for their assistance.

I have a special thought for Stephen Bueltmann, who acquainted me with the field of nuclear physics and Jefferson Laboratory while being a young student at Old Dominion University. You made me discovered a field that fulfilled my curiosity and gave me the opportunity to pursue it.

This thesis started in the former Institut de Physique Nucléaire d'Orsay where I spend some memorable moments. Thank you to all the permanent staff of the JLab group: Silvia Niccolai, Carlos Muñoz Camacho, Eric Voutier, and the latest member Mostafa Hoballah. A big thank you to Dominique Marchand for being always available to listen to students and give them good advice.

I must give special thanks to Pierre Chatagnon and Ho San Ko. What started as two offices mates quickly became travel companions and amazing friends. From the night trains of the Balkans to the mountains of South Korea, I cherished the time we spent in and out of the office. I will miss our after-work conversations around a beer, talking about some absurd experiment proposals or ideas, which now that I think about them were regularly food-oriented.

I wish good luck to the remaining students of the group and wish them well for the end of their thesis; thank you to Mylène Caudron, Lucien Causse, Sami Habet, and Mathieu Ouillon.

I was grateful to see you again Corentin Allaire (et son chapeau) and Julien Ripoche after our terrific time at CERN as summer students. Thank you for inviting me to the

weekly movie nights at LAL, which were not only about the movie being watched but more about the shared experience and feedback regarding the life of a Ph.D. student. So, thank you to Cloé Girard-Carillo, Antinéa Guerguichon, Christophe Goudet and Antoine Laudrain (and his impressive work endurance) for these moments. And a special thanks to Christina Agapopoulou for your high spirits and your special ability to understand a joke that no one else would get.

Additionally, I must thank Antoine Boulet for our numerous coffee breaks and friendship. After your departure from the laboratory, the long walks to the coffee machine were not the same, but I would still get the *Potage de Légumes* from time to time.

My time in Chicago was embellished by the moments spend with great friends. While not being a theoretical physicist, I much enjoyed our lunches and time out of the office with the theory group. Thank you to Bob Wiringa, Noemi Rocco, and Alessandro Lovato for that.

I want to express my gratitude for my compatriots and friends, Kévin Fossez and Steven Calvez, stuck together in Chicago during the pandemic. Our Saturday gatherings were always a pleasure and helped to keep the spirit up. Thank you, a lot, Steven, for giving me shelter during my last few months in Chicago.

I would like to thank Gabriel Charles; we got a chance to know each other since our tedious work removing the stickers of about 400 circuit boards from a detector and managed to follow each other ever since, whereas it was in Norfolk or finally in Orsay. And, of course, I will not forget to thank Olga Kochebina and our shared passion for coffee and carrot cakes at Café Stella.

Then, there is a Scottish guy, two Italians, and a bunch of Frenchs (yes, I know it sounds like the beginning of a bad joke). And while the name of our group is rather not suitable to be written here, you made the trips to JLab and the mighty resfac a pleasure. So, thank you Stuart Fegan, Ilaria Balossino, Giulio Mezzadri and Maxime Levillain.

I cannot conclude this list without thanking a dear friend met some 13 years ago. While we parted different ways and places after high school, we never diverged too much in opinions and personality. And when not talking about our next vacations, I valued our discussions about life and the world we live in, whether those discussions took place on the bank of the Seine, in the freezing temperature of Svalbard, or simply just by messages while being 7000 km away. Merci Sébastien!

Pour finir, je voudrais remercier les personnes les plus importantes de toutes, ma famille. Merci à mes parents pour m'avoir soutenu tout au long de ce périple, et merci pour les valeurs et l'éducation qui ont fait de moi la personne que je suis aujourd'hui. Je souhaite aussi remercier mes merveilleuses sœurs, dont je suis très fier de leur caractère, force et ambition. Et je finirais par ces quelques mots, simples mais résumant mon ressenti : Maman, Papa, Catherine et Mathilde, merci pour tout et je vous aime !

Les grandes personnes m'ont conseillé de laisser de côté les dessins de serpents boas ouverts ou fermés, et de m'intéresser plutôt à la géographie, à l'histoire, au calcul et à la grammaire. C'est ainsi que j'ai abandonné, à l'âge de six ans, une magnifique carrière de peintre. J'avais été découragé par l'insuccès de mon dessin numéro 1 et de mon dessin numéro 2. Les grandes personnes ne comprennent jamais rien toutes seules, et c'est fatigant, pour les enfants, de toujours et toujours leur donner des explications.

J'ai donc dû choisir un autre métier et j'ai appris à piloter des avions. J'ai volé un peu partout dans le monde. Et la géographie, c'est exact, m'a beaucoup servi. Je savais reconnaître, du premier coup d'oeil la Chine de l'Arizona. C'est très utile, si l'on est égaré pendant la nuit.

J'ai ainsi eu, au cours de ma vie, des tas de contacts avec des tas de gens sérieux. J'ai beaucoup vécu chez les grandes personnes. Je les ai vues de très près. Ça n'a pas trop amélioré mon opinion.

Quand j'en rencontrais une qui me paraissait un peu lucide, je faisais l'expérience sur elle de mon dessin numéro 1 que j'ai toujours conservé. Je voulais savoir si elle était vraiment compréhensive. Mais toujours elle me répondait : « C'est un chapeau. » Alors je ne lui parlais ni de serpents boas, ni de forêts vierges, ni d'étoiles. Je me mettais à sa portée. Je lui parlais de bridge, de golf, de politique et de cravates. Et la grande personne était bien contente de connaître un homme aussi raisonnable.

Antoine DE SAINT-EXUPÉRY – *Le Petit Prince*

Contents

Introduction

Protons and neutrons are the building blocks of matter and account for 99% of the mass of the visible universe. Until the early 1930s, the proton was thought to be an elementary point-like particle. However, Frisch and Stern [1], using diffraction experiments, measured the magnetic moment of the proton and found a result inconsistent with a point-like particle. In the 1950s, this result was confirmed by Hofstadter's electron elastic scattering (ES) experiments which measured the electromagnetic current spacial distributions and calculated the size of the proton to be of the order of 10^{-13} cm [2].

Following Hofstadter's experiments, electromagnetic probes have been widely used to study the structure of the proton. In the late 1960s, a new type of scattering was performed: the Deep Inelastic Scattering (DIS). Using higher energy lepton beams, these new experiments were able to probe smaller distances inside the nucleon and led to the discovery of the constituents of the nucleons, the quarks. Protons and neutrons are no longer considered fundamental building blocks of matter, but rather particles composed of quarks held up by gluons, the gauge boson of the strong interaction. DIS experiments allow for the extraction of Parton Distributions Functions (PDFs), which encode the probability density of finding a parton carrying a certain longitudinal momentum fraction of the nucleon.

The strong interaction confines the quarks into the nucleon and, at larger scale, binds the nucleons into atomic nuclei. After a series of DIS measurements on different nuclei, the properties of the quarks in bound nucleons were found to be different than the properties of quarks inside a free nucleon. Named after the experiment that first measured this behavior, the EMC effect uncovers phenomena inside the nucleus affecting the properties of quarks and how they compose the nucleons. Today, the EMC effect continues to be studied and various theoretical models attempt to explain this behavior. However, it remains elusive and we do not have a good understanding of these nuclear effects.

A new set of structure functions, called Generalized Parton Distributions (GPDs), were introduced in the late 1990s and correlate the longitudinal momentum of a parton and its transverse position. The GPDs are extracted from exclusive reactions, such as the Deeply Virtual Compton Scattering (DVCS, $ep \rightarrow e'p'\gamma$). While extensive physics programs aimed to measure DVCS on the proton have been carried out at different laboratories such as Jefferson Laboratory, few results exist of DVCS on nuclear targets. The measurements of GPDs on nuclei could be a different approach to study the EMC effect and understand the underlying structure of nucleons inside the nucleus.

Located in the United States, Jefferson Laboratory is designed to study the quarks inside the nucleon. The 6 GeV polarized electron beam fed 3 experimental halls (A, B and C), each housing a spectrometer. The Hall B CLAS detector was a large acceptance spectrometer, tailored to measured multiple final state particles at large angles. The measurement of GPDs is one of Jefferson Laboratory's focus and several DVCS results were published using the CLAS data.

The CLAS run 'eg1-dvcs' was a series of measurements aimed at the study of the GPDs with polarized protons using an ammonia (NH_3) polarized target. This thesis will extract DVCS observables on nitrogen using the NH_3 data to further our understanding of nuclear effects at the parton level. In order to analyze the incoherent DVCS channel, we will need to subtract the proton background and nitrogen events will be selected using a set of exclusivity cuts. We eventually want to obtain the Beam Spin Asymmetries of incoherent DVCS off nitrogen. This result can then be compared to the free proton data and the other incoherent nuclear DVCS results.

This manuscript is organized in five chapters:

- Chapter 1 is an introduction to lepton scattering on nucleons with an emphasis on the study of the nucleon structure inside the nucleus (EMC effect). The final part of this chapter will detail the properties of the GPDs and the DVCS reaction used to access them.
- Chapter 2 describes the facility and experimental apparatus used by the eg1-dvcs experiment. An introduction to the accelerator is made, followed by a presentation of the CLAS detector.
- Chapter 3 lists all the cuts used to identify the electron, the proton, and photon which are the final state particle of DVCS.
- Chapter 4 summarized the procedure applied in order to identify the incoherent nitrogen DVCS events. The method used to identify and subtract the hydrogen events is discussed, before the relevant cuts ensuring the exclusivity of the reaction are applied.
- Chapter 5 concludes with the results of the extracted nitrogen DVCS asymmetries. The results are also compared to the DVCS measurements on helium-4.

CHAPTER 1

The Structure of Nucleons

The constituents of the nucleons were historically named partons by Feynman [3], and a theoretical model arose from their discovery. The parton model successfully described how the partons are combined and make up nucleons. Ultimately, a new quantum field theory - called Quantum Chromodynamics - was developed to explain the mechanisms of the strong interaction, the force binding color charged quarks with their gauge bosons - the gluons. One of the main properties of QCD is asymptotic freedom and determined when perturbation theory (pQCD) can be used. At energies comparable to the nucleon mass, the coupling constant of QCD α_s is large and pQCD cannot be applied; while at higher energies, α_s becomes small enough for pQCD to be used. A second property of QCD is color confinement. The QCD potential increases with the distance until the energy is high enough to create a quark-antiquark. Therefore, the quarks cannot be isolated and must be combined in order to create neutrally color charged objects.

This chapter will review the basics of lepton-nucleon scattering experiments and how the structure of the nucleon is obtained from them. A brief overview of lepton scattering on an atom's nucleus will be addressed. And finally, the Deeply Virtual Compton Scattering (DVCS) will be discussed with the emphasis of such process on nuclei.

1.1

Elastic Scattering and Form Factors

Lepton elastic scattering off a nucleon target is defined as :

$$\mathrm{l}(k) + \mathrm{N}(p) \rightarrow \mathrm{l}'(k') + \mathrm{N}'(p') \tag{1.1}$$

where l is the incoming lepton of four-momentum k, N is the target nucleon of four-momentum p, l' is the scattered lepton of four-momentum k', and N' is the scattered

nucleon of four-momentum p'. Figure 1.1 is the Feynman diagram of the lepton-nucleon elastic scattering at leading order.

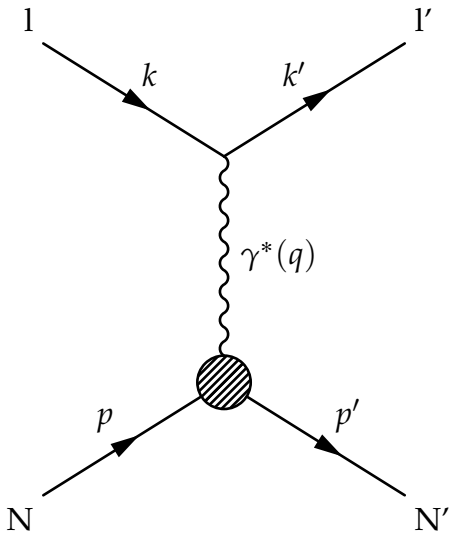

FIGURE 1.1 – Feynman diagram of a lepton-nucleon elastic scattering at leading order.

At leading order and in the Born approximation, the lepton and nucleon exchange momentum via a virtual photon γ^* of four-momentum q. The four-momentum squared of the virtual photon is defined as $q^2 = (k - k')^2$, which is always negative for elastic scattering. A positive variable, called the virtuality Q^2, is defined as :

$$\begin{aligned} Q^2 &\equiv -q^2 \\ &= -(k - k')^2 \\ &\overset{lab}{=} 4EE' \sin^2\left(\frac{\theta_e}{2}\right) \end{aligned} \tag{1.2}$$

where E is the energy of the incoming lepton, E' is the energy of the scattered lepton and θ_e is the scattered lepton angle. It should be pointed out that the last expression in equation 1.2 is how Q^2 is calculated in the laboratory frame for fixed target lepton-nucleon scattering.

For lepton scattering on a point-like particle, the cross section of the elastic process can the calculated using the Mott formula:

$$\left(\frac{d\sigma}{d\Omega}\right)_{\text{Mott}} = \frac{\alpha^2}{4E^2 \sin^4 \frac{\theta_e}{2}} \cos^2 \frac{\theta_e}{2} \tag{1.3}$$

where Ω is the solid angle of the scattered lepton and $\alpha = \frac{e^2}{4\pi}$ is the electromagnetic coupling constant.

The scattering of electrons on a hydrogen target (protons) at rest have been measured by Hofstadter in the 1950s, with electron energies ranging from 100 to 236 MeV [4]. Figure 1.2 shows how at large scattering angles, the measured cross section differed from the cross section calculated with the Mott formula. This discrepancy, at large Q^2, is one proof that the proton is not a point-like particle.

In order to extract information about the charge and magnetic moment distributions, some addition to the Mott formula is required. These additions are included in the Rosenbluth formula [5], which is expressed as:

$$\left(\frac{d\sigma}{d\Omega}\right)_{\text{Rosenbluth}} = \left(\frac{d\sigma}{d\Omega}\right)_{\text{Mott}} \frac{E'}{E}\left(\frac{G_E^2(Q^2) + \tau G_M^2(Q^2)}{1+\tau} + 2\tau G_M^2(Q^2)\tan^2\frac{\theta_e}{2}\right) \quad (1.4)$$

where $\tau = \frac{Q^2}{4m_N^2}$, m_N is the mass of the nucleon, $G_E(Q^2)$ and $G_M(Q^2)$ are respectively the Sachs electric and magnetic Form Factors (FFs).

$F_1(Q^2)$, the helicity conserving Dirac FF, and $F_2(Q^2)$, the helicity non-conserving Pauli FF, are related to the Sachs FFs as follows:

$$F_1(Q^2) = \frac{1}{\tau+1}\left(\tau G_M^2(Q^2) + G_E^2(Q^2)\right) \quad (1.5)$$

$$F_2(Q^2) = \frac{1}{\tau+1}\left(G_M^2(Q^2) - G_E^2(Q^2)\right) \quad (1.6)$$

Figure 1.3 shows the Sachs proton FFs measured and fitted for various experiments. In the limit $Q^2 \to 0$, the fitted values of $G_E^2(Q^2)$ and $G_M^2(Q^2)$ are 1 and 2.79 respectively, in agreement with the electric charge of the proton and the magnetic moment of the proton μ_p.

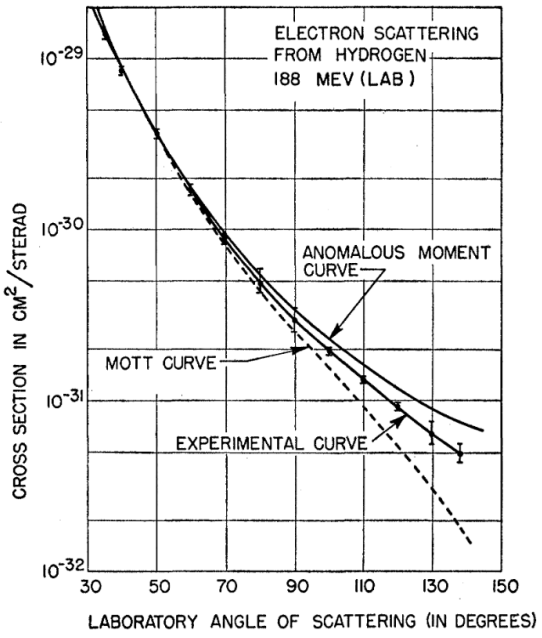

FIGURE 1.2 – Cross section of the elastic scattering as a function of the lepton scattering angle. Comparison between the Mott calculations, the anomalous moment curve and the experimental data of 188 MeV electron scattering from hydrogen (proton) [4].

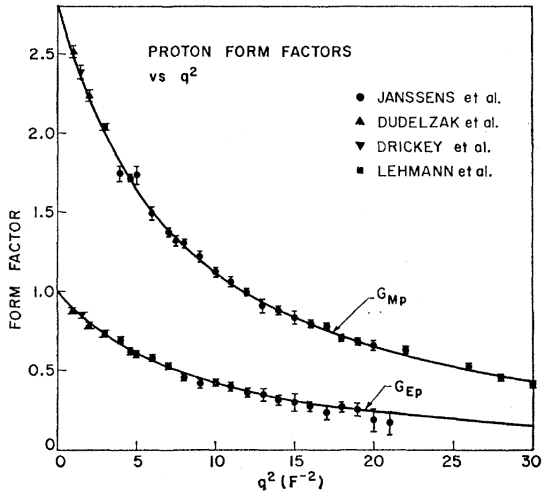

FIGURE 1.3 – The Sachs FFs as measured by various experiments as a function of Q^2 (in Fermi^{-2}). Figure from [6].

1.2

Deep Inelastic Scattering and Parton Distribution Functions

1.2.a – Structure Functions

The wavelength of the virtual photon is inversely proportional to the square root of the virtuality: $\lambda \propto 1/\sqrt{Q^2}$. Thus, as the energy of the incoming lepton increases, the wavelength of the virtual photon decreases, allowing to probe distances smaller than the size of the nucleon. For inelastic reactions, the $Q^2 > 1\,\mathrm{GeV}^2/c^2$ limit is the conventional starting point of the Deep Inelastic Scattering (DIS). In this process, the nucleon breaks up and creates an undefined final state X consisting of many particles (see figure 1.4):

$$\mathrm{l}(k) + \mathrm{N}(p) \rightarrow \mathrm{l}'(k') + \mathrm{X} \tag{1.7}$$

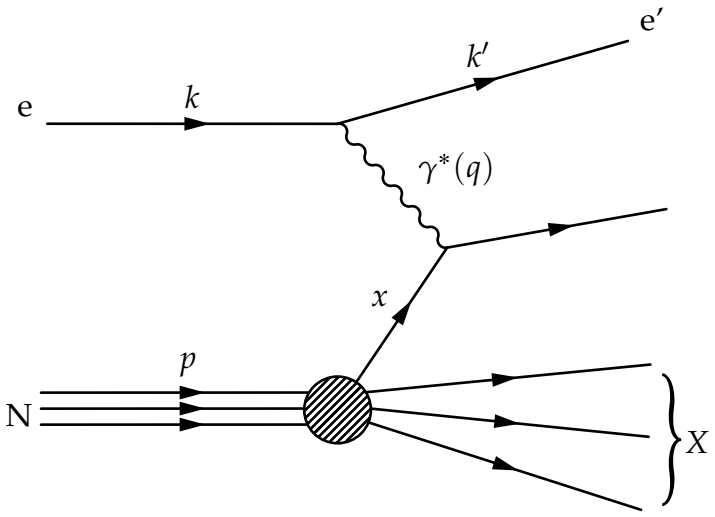

FIGURE 1.4 – Feynman diagram of an electron-nucleon deep inelastic scattering.

DIS is usually characterized by the following invariant kinematical quantities:

- Q^2 defined in equation 1.2
- $\nu \equiv \frac{p \cdot q}{m_N} \overset{lab}{=} E - E'$ is the energy transferred by the lepton via the virtual photon.
- $x_B \equiv \frac{Q^2}{2p \cdot q} = \frac{Q^2}{2M_N \nu}$ is the Bjorken scaling variable. At leading order, it is interpreted as the fraction of the nucleon's longitudinal momentum x carried by the struck quark in the infinite momentum frame[1].
- $y \equiv \frac{p \cdot q}{p \cdot k} \overset{lab}{=} \frac{\nu}{E}$ is called the inelasticity. It is the fractional energy lost by the lepton in the target rest frame.
- $W^2 \equiv (p+q)^2 = M_N^2 + 2M_N \nu - Q^2$ is the invariant mass squared of the hadronic final state X

For $x_B = 1$, which is equivalent to $W^2 = M_N^2$, the scattering is elastic, and the nucleon remains intact. For $1 < W^2 \lesssim 4\,\mathrm{GeV}/c^2$, the target nucleon can be excited into a resonance state. In DIS, we want to avoid these resonances and events are selected by applying a cut on the invariant mass $W > 2 - 3$ GeV/c^2, removing most of the resonances.

[1] In infinite momentum frame, the nucleon has a very large momentum along the z-axis, such that $p_z \gg (p_x, p_y)$ and therefore the transverse momentum $p_\perp$ can be neglected.

The cross section for lepton-nucleon scattering can be calculated using the following formula:

$$\frac{d\sigma}{d\Omega dE'} = \frac{\alpha^2}{Q^4}\frac{E'}{E}L_{\mu\nu}W^{\mu\nu} \tag{1.8}$$

where $L_{\mu\nu}$ is the leptonic tensor and $W^{\mu\nu}$ is the hadronic tensor.

If the lepton is unpolarized and its mass is neglected, the leptonic tensor is:

$$L_{\mu\nu} = 2\left(k^\mu k'^\nu + k^\nu k'^\mu - g^{\mu\nu}(k\cdot k')\right) \tag{1.9}$$

where $g^{\mu\nu}$ is the metric tensor.

For an unpolarized nucleon, the hadronic tensor can be parameterized as:

$$W_{\mu\nu} = \left(\frac{q_\mu q_\nu}{q^2} - g_{\mu\nu}\right)W_1(\nu, Q^2) + \left(P_\mu - \frac{P\cdot q}{q^2}q_\mu\right)\left(P_\nu - \frac{P\cdot q}{q^2}q_\nu\right)\frac{W_2(\nu, Q^2)}{M_N^2} \tag{1.10}$$

The resulting cross section is:

$$\frac{d\sigma}{d\Omega dE'} = \frac{\alpha^2}{4E^2\sin^4\frac{\theta_e}{2}}\left(W_2(\nu, Q^2)\cos^2\frac{\theta_e}{2} + 2W_1(\nu, Q^2)\sin^2\frac{\theta_e}{2}\right) \tag{1.11}$$

where W_1 and W_2 are structure functions depending on ν and Q^2.

A new set of structure functions with a dependence on x can be defined from W_1 and W_2:

$$\begin{aligned}\mathcal{F}_1(x, Q^2) &= M_N W_1(\nu, Q^2)\\ \mathcal{F}_2(x, Q^2) &= \nu W_2(\nu, Q^2)\end{aligned} \tag{1.12}$$

and an analog expression to the Rosenbluth formula is found by substituting equations 1.12 into equation 1.11:

$$\frac{d\sigma}{d\Omega dE'} = \frac{\alpha^2}{4E^2\sin^4\frac{\theta_e}{2}}\left(\frac{\mathcal{F}_2(x, Q^2)}{\nu}\cos^2\frac{\theta_e}{2} + 2\frac{\mathcal{F}_1(x, Q^2)}{M_N}\sin^2\frac{\theta_e}{2}\right) \tag{1.13}$$

1.2.b – The Parton Model

In the Bjorken limit $\{Q^2, \nu\} \to \infty$ and at a fixed x_B value, the DIS can be considered as the scattering of a lepton on a free quark. In this case, the DIS cross section on nucleon can be expressed as the sum of the elastic cross section of lepton on the different quark flavors:

$$\left(\frac{d\sigma}{d\Omega dE'}\right)_{N,\,\mathrm{DIS}} = \sum_q \int_0^1 dx\, e_q^2 f_q(x) \left(\frac{d\sigma}{d\Omega dE'}\right)_{q,\,\mathrm{ES}} \delta(x - x_B) \tag{1.14}$$

where e_q is the charge of the quark of flavor q, and $f_q(x)$ is the probability of finding a quark of flavor q carrying a longitudinal momentum fraction x, the so-called Parton Distribution Functions (PDFs).

After integration and comparing to equation 1.13, the $\mathcal{F}_1$ and $\mathcal{F}_2$ structure functions relate to the quark PDFs by the following relations:

$$\mathcal{F}_1(x) = \frac{1}{2} \sum_q e_q^2 f_q(x) \tag{1.15}$$

$$\mathcal{F}_2(x) = x \sum_q e_q^2 f_q(x) \tag{1.16}$$

The Callan-Gross relation is obtained from the two previous expression [7]:

$$\mathcal{F}_2(x) = 2x\mathcal{F}_1(x) \tag{1.17}$$

Since the PDFs can be compared to the ES of a lepton on a free quark, no Q^2 dependence is expected. The early DIS experiments agreed with this Q^2 independence. However, measurements made at high energy facilities unraveled a more complex picture (see figure 1.5). As Q^2 increases, more gluons are radiated, which will turn into $q\bar{q}$ pairs. This effect is particularly noticeable at low x where the valence quarks distributions decrease and the sea $q\bar{q}$ and gluon distributions increase (see figure 1.6). This evolution in Q^2 of the structure functions can be calculated using the DGLAP[1] equations [8].

[1] Dokshitzer–Gribov–Lipatov–Altarelli–Parisi

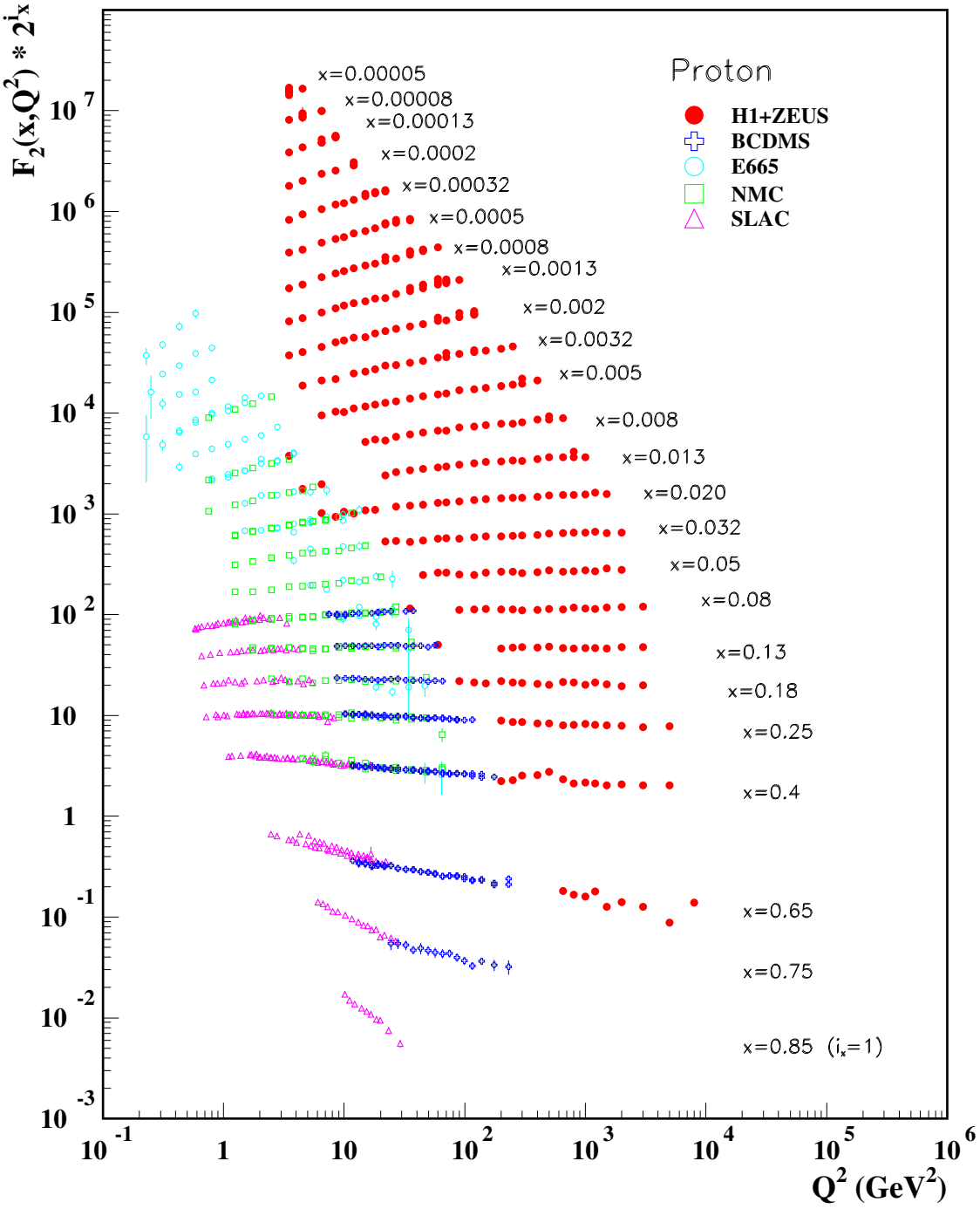

FIGURE 1.5 – $\mathcal{F}_2^p$ measured in electromagnetic scattering by electrons/protons collider or electrons/muons on fixed targets. Figure from [9].

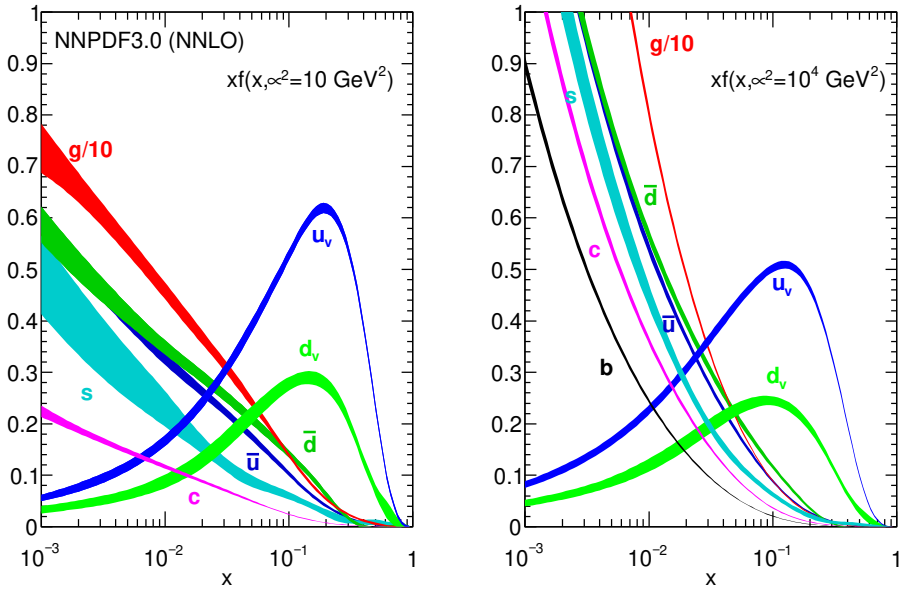

FIGURE 1.6 – Global fits of PDFs inside an unpolarized proton at two different Q^2 values. In the present case, at high x, we can notice that the density of u quark (2/3) and d quark (1/3) is coherent with valence quarks making up the proton. Figure from [9].

1.3

Lepton Scattering on Nuclei and EMC Effect

The European Muon Collaboration (EMC) measured DIS cross sections using a muon beam, ranging from 100 GeV to 280 GeV, on an iron and a deuterium target. The binding energy of nucleons inside the nucleus is of the order of a few MeV and is much lower than a nucleon mass (close to 1 GeV), therefore the comparison between cross sections in nuclear targets and cross section of the same number of free nucleons can be naively expected to be the same, and their ratio should tend to unity. In 1983, the EMC collaboration published the ratio $\mathcal{F}_2^{Fe}/\mathcal{F}_2^{D}$ and observed a downward slope as a function of x_B [10]. This unexpected result demonstrates the difference in nucleon structure between nucleons inside nuclei and free nucleons. For the past 35 years, several experimental programs measured similar behavior for various x_B range and nuclear targets at CERN, Desy, Fermilab, SLAC, and JLab. Selected results can be found in figure 1.7.

The distribution can be divided in four different regions:

- the shadowing region ($x \lessapprox 0.1$): the ratio is suppressed and increases until reaching unity around $x_B \approx 0.1$. If the number of nucleons in the nucleus A increases, the suppression increases as well. In this region, the contribution of the sea quarks is sizable (see figure 1.6), and one of the explanations for the shadowing effect is the greater overlap of sea quarks and gluons between nucleons at small x. Thus

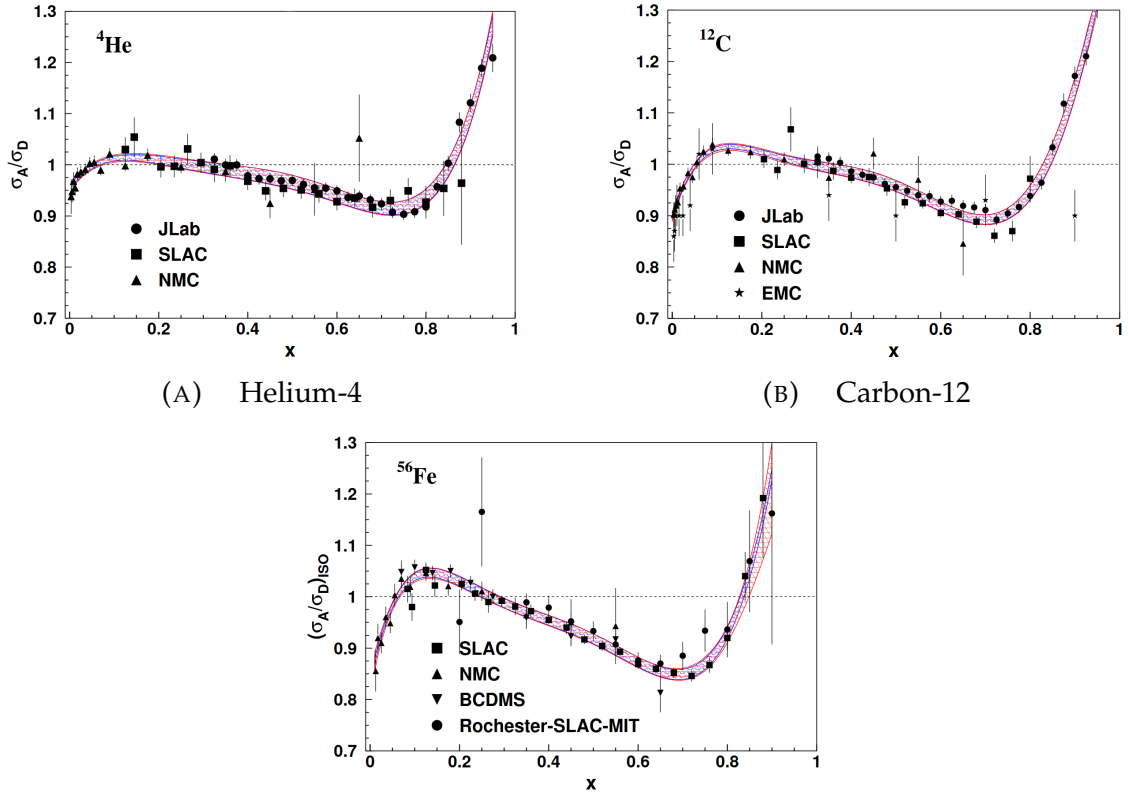

(A) Helium-4 (B) Carbon-12

(C) Iron-56

FIGURE 1.7 – Ratios of ^4He, ^{12}C and ^{56}Fe nuclei to deuterium DIS cross sections. The error bars represent both the statistical and systematic uncertainties. The red band is the uncertainty of the global fit. Figures taken from [11] using data from [12], [13], [14], [15], [16], [17], [18], [19] and [20]

increasing the density of sea quarks and gluons inside the nucleus;

- the anti-shadowing region ($0.01 \lessapprox x < 0.3$): the ratio is slightly enhanced and does not show any clear dependence on A;
- the EMC effect region ($0.3 < x < 0.8$): the ratio is suppressed, and increases for large values of A and x. Some of the models trying to explain the behavior of the ratio in this region will be detailed below;
- the Fermi motion region ($x > 0.8$): in this region the structure function $\mathcal{F}_2$ of free nucleons drops. However, $\mathcal{F}_2$ of nucleons inside the nucleus is dominated by the Fermi momentum contribution, for that reason the ratio drastically increases.

The following subsections will focus on the EMC effect, which is most relevant to this work, and will give a brief overview of some of the current theoretical models used to explain the EMC effect.

1.3.a – Dependence on the Nuclear Number and Density

The E139 experiment at SLAC measured the DIS cross section of various nuclear targets ranging from ^{4}He to ^{197}Au [14]. In their analysis, they looked at the slope dependence of the EMC ratio with respect to A. The data set was later completed by the Jefferson Laboratory E03-103 experiment which focused on light nuclei [12]. Figure 1.8 is a plot combining both data sets and is linearly fitted for $A \geqslant 12$.

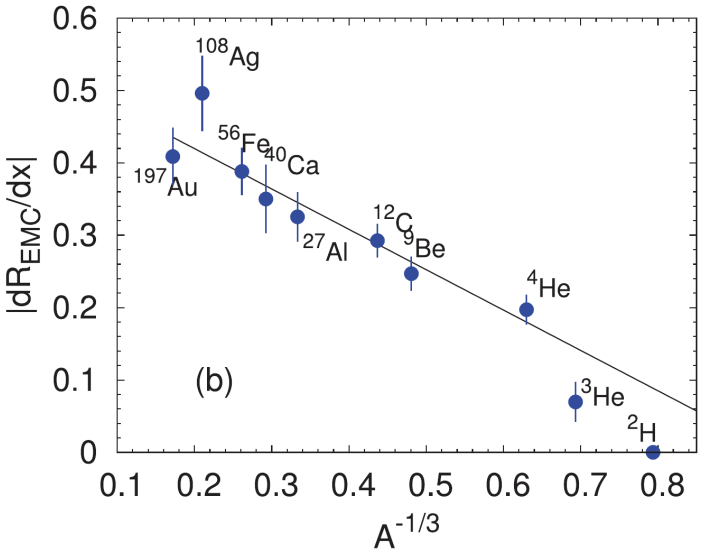

FIGURE 1.8 – Slope of the EMC ratio for different nuclei as a function of $A^{-1/3}$. The line is a linear fit for $A \geqslant 12$. Figure from [21].

The E03-103 experiment measured the EMC effect on light nuclei and compared the EMC ratio slope $|dR_{\text{EMC}}/dx|$ as a function of the average nuclear density [12] (see

figure 1.9). The EMC ratio slopes appear to be correlated to the average nuclear density, with the exception of ^{9}Be. The current explanation for this observation is that ^{9}Be could be thought as a cluster of two alpha particles and a neutron, hence possessing a larger "local" nuclear density. The nuclear density of heavy nuclei varies little with A, therefore this result supports the idea that the EMC effect is rather the consequence of local nuclear effect than a simple scaling of the atomic number and average nuclear density.

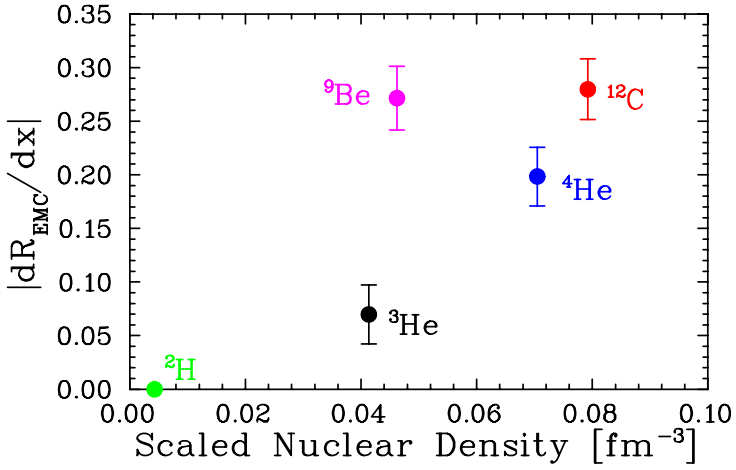

FIGURE 1.9 – The EMC slope of light nuclei as a function of the average nuclear density [12].

1.3.b – Short Range Correlations

By definition, the DIS kinematics on free nucleons restrict x to be smaller or equal to 1. However, it is possible for inclusive cross sections of a nucleus to reach values of x greater than 1. The result of experiments done at Jefferson Lab showed that the inclusive cross section ratio σ^A/σ^D rises until reaching a plateau for $x \gtrsim 1.5$ [22] (see figure 1.10)

The overlap of two nucleons wave-functions, known as Short Range Correlation (SRC) explains this plateau region. The SRC scale factor $a_2(A/d)$ is defined as the value of the ratio in this plateau region and expresses the relative probability of nucleons to be part of a SRC pair. If one plots the slope of the EMC ratio as a function of $a_2(A/d)$, a linear dependence is found and applies to light and heavy nuclei [23] (see figure 1.11). The discovery of a link between SRC numbers and the EMC slope has provided a new test for models on the EMC effect, but does not give a definite answer as to how it arises.

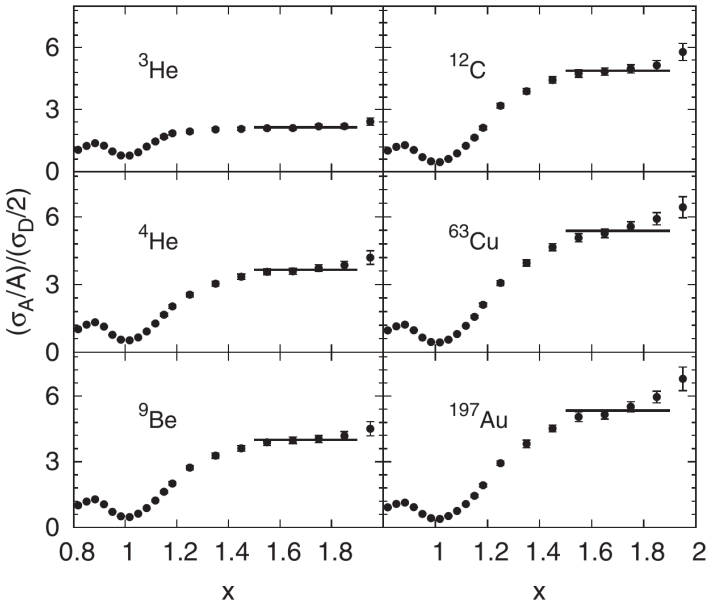

FIGURE 1.10 – Inclusive cross section ratio σ^A/σ^D for several nuclei as a function of x at $\theta_e = 18^\circ$ [22].

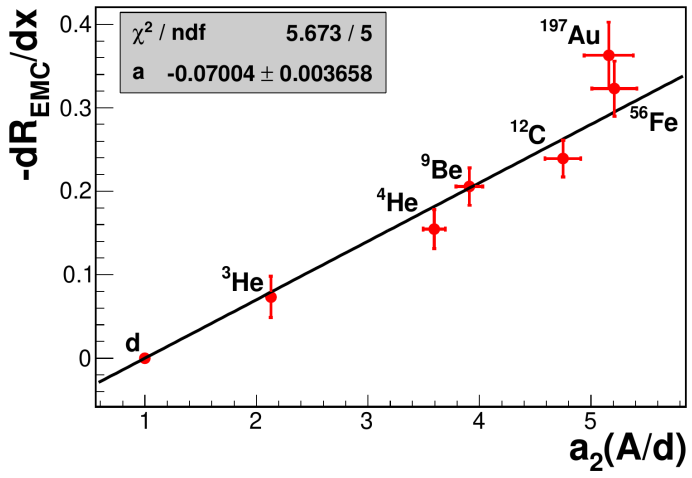

FIGURE 1.11 – The slope of the EMC effect as a function of the SRC scale factor$a_2(A/d)$. Figure from [23].

1.3.c – Theoretical Models

The EMC effect has remained a mystery for the past 35 years. We will present below a selection of models. Rather than being exclusive, we try to illustrate here the different ideas that have been explored in the past decades to explain the EMC effect.

Nuclear Binding

The kinematics used to calculate DIS cross sections assumed that the struck nucleon was on-shell, with $p = (M_N, \vec{p})$. However, the nucleons inside the nucleus are bound by an average negative binding energy $\langle\epsilon\rangle$, and the nuclear binding model proposes the binding energy must be included in the calculation of the nucleon momentum. The new $p' = (M_N + \langle\epsilon\rangle, \vec{p})$ four-momentum will scale the x value, which will become : $x' = Q^2/2p' \cdot q$ [24]. This rescaling of $\mathcal{F}_2$ in x can describe the behavior of the EMC and Fermi motion regions, however it fails to explain the rise in the anti-shadowing part (see figure 1.12) [25].

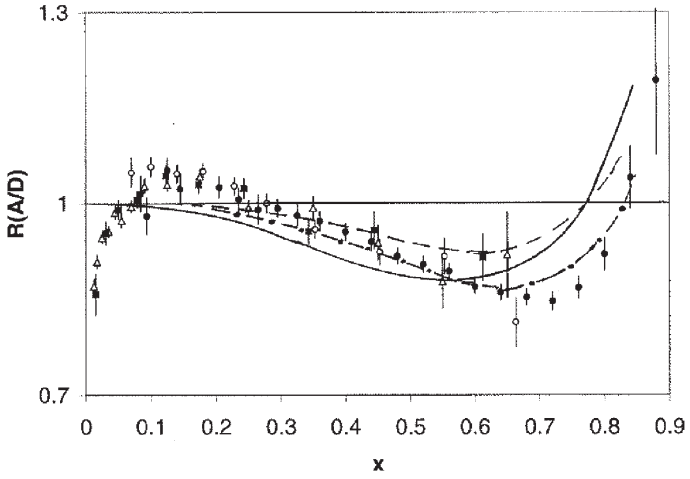

FIGURE 1.12 – Comparison of EMC ratios and nuclear binding models. Data from SLAC (•) [14], the EMC collaboration (▪) [26], the BCDMS collaboration (○) [20] and the NMC collaboration (▵) [13]. The full line is a model from [24], the dashed and dot-dashed lines are models from [27] using $\langle\epsilon\rangle = -26$ MeV and $\langle\epsilon\rangle = -39$ MeV respectively.

Pion Enhancement

At long range, the nucleons inside the nucleus are bound via the exchange of virtual mesons (predominantly pions). Therefore the total momentum of the nucleus could be shared between the nucleons and the virtual pions [28]. This model would lead to re-writing the $\mathcal{F}_2^A$ structure function as the sum of the nucleons and pion contributions:

$$\mathcal{F}_2^A(x) = \int_y^A dy\, f_N(y)\mathcal{F}_2^N\left(\frac{x}{y}\right) + \int_y^A dy\, f_\pi(y)\mathcal{F}_2^\pi\left(\frac{x}{y}\right) \tag{1.18}$$

If the pion field is enhanced, the model reproduced the EMC effect (see figure 1.13). However, it also predicts an increase of the sea quark distribution between the nucleons inside the nucleus and free nucleons. Drell-Yan results from Fermilab showed no enhancement of the sea quark contributions in bound nucleons for $0.1 < x < 0.3$ [29]. The SeaQuest experiment at Fermilab intent to confirm this result and probe the region $x > 0.3$ [30].

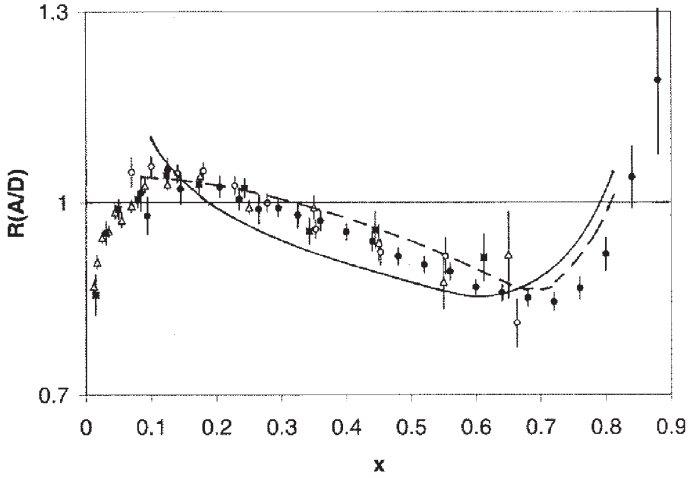

FIGURE 1.13 – Comparison of EMC ratios and pion enhancement models. Data from SLAC (•) [14], the EMC collaboration (▪) [26], the BCDMS collaboration (○) [20] and the NMC collaboration (▵) [13]. The full line is a model from [31], the dashed line is a model from [32].

Multi Quark Clusters

Close nucleons inside the nucleus could form multi-quark clusters, composed of $3n$ quarks (3, 6, 9, ...) [33]. Likewise to the pion enhancement, this model would modify the $\mathcal{F}_2^A$ structure function in equation 1.18, replacing the pion contribution with one from multi-quark clusters. Parametrization of the contribution of such clusters can be done in order to match the EMC effect (see figure 1.14), however no clear signature has been proposed to measure these multi-quark clusters [34].

Dynamical Rescaling

The $\mathcal{F}_2^A$ structure function of nucleus appears to be similar to the $\mathcal{F}_2^N$ structure function of free nucleons measured at higher Q^2 [36]. This model introduces a rescaling factor ξ_A which depends on Q^2 and varies for different nuclei (see figure 1.15):

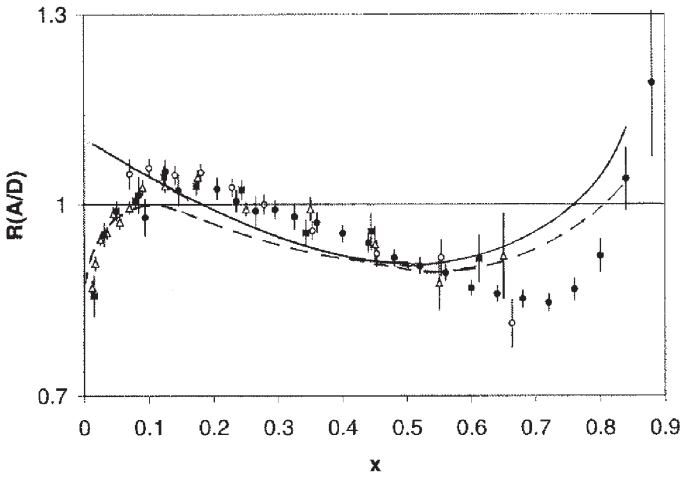

FIGURE 1.14 – Comparison of EMC ratios and multi quark clusters models. Data from SLAC (•) [14], the EMC collaboration (▪) [26], the BCDMS collaboration (○) [20] and the NMC collaboration (▵) [13]. The full line is a model from [33], the dashed line is a model from [35].

$$\mathcal{F}_2^A(x) = \mathcal{F}_2^N\left(x, \xi_A(Q^2)Q^2\right) \tag{1.19}$$

This rescaling is motivated by an hypothesized larger confinement area of quarks inside nucleus. Similarly to the Q^2 evolution of the free nucleon structure functions, ξ_A can be determined using the modified nuclear PDFs DGLAP equations [37].

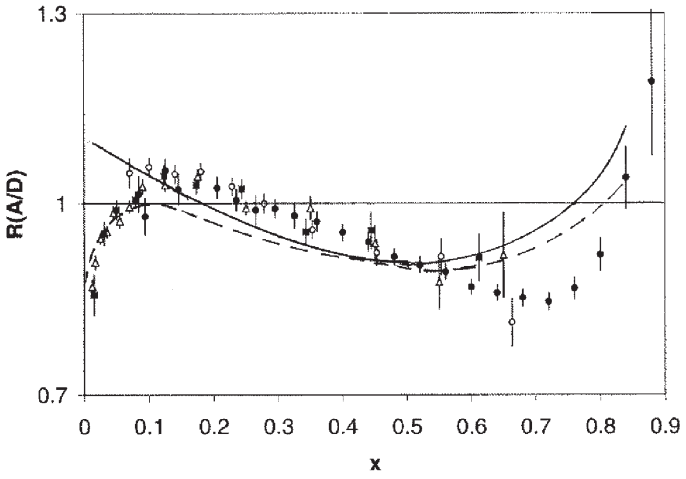

FIGURE 1.15 – Comparison of EMC ratios and dynamical rescaling models. Data from SLAC (•) [14], the EMC collaboration (▪) [26], the BCDMS collaboration (○) [20] and the NMC collaboration (▵) [13]. The full and dashed lines are models from [38] for different ranges of Q^2 corresponding to the SLAC and EMC data respectively.

1.4

Deeply Virtual Compton Scattering and Generalized Parton Distributions

1.4.a – Theory of GPDs

A new theoretical framework was introduced in the early 1990s which correlates the longitudinal momentum of a parton and its transverse position inside the nucleon: the Generalized Parton Distributions (GPDs) [39] [40] [41]. They are universal structure functions accessible through Deep Exclusive Scattering processes, such as the electroproduction of a real photon, the Deeply Virtual Compton Scattering (DVCS), and the electroproduction of a meson, the Deeply Virtual Meson Production (DVMP). The characteristics and features of the GPDs do not depend on the reaction used to measure them.

This work will focus on DVCS :

$$l(k) + N(p) \rightarrow l'(k') + N'(p') + \gamma(q') \tag{1.20}$$

where γ is a real photon of four-momentum q'.

In the Bjorken regime ($Q^2 \rightarrow \infty$ and $\nu \rightarrow \infty$), QCD factorization can be used to decomposed DVCS and DVMP processes into two parts: the "hard" interaction between the virtual photon and the struck quark, which is calculable using perturbative QCD, and the "soft" part parametrized by the GPDs [42] [43]. Figure 1.16 shows a Feynman diagram of DVCS at leading twist and leading order.

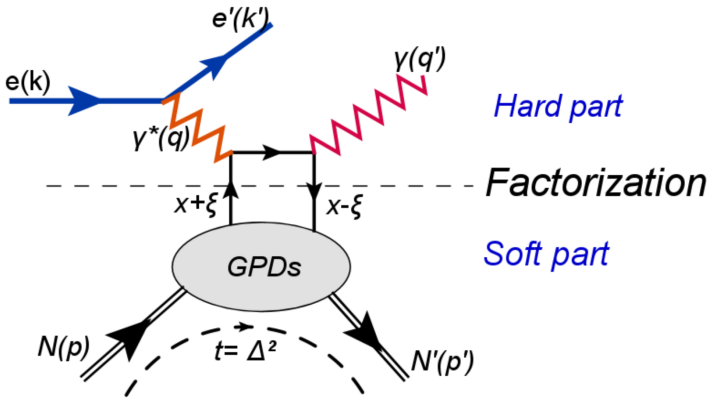

FIGURE 1.16 – Feynman diagram of the Deeply Virtual Compton Scattering at leading twist and leading order. Figure from [44]

Since the initial and final nucleons are collinear and along the z-axis, GPDs are parameterized in the light-cone coordinate system. Therefore a four-momentum vector in this frame can be written as : $a^{\pm} = (a^0 \pm a^3)/\sqrt{2}$, where the $+$ or $-$ sign represents the direction of the particle along the z-axis.

Within this formalism, GPDs are depending on three variables:

- $x = \dfrac{k^+}{P^+}$ is the average fractional momentum carried by the struck quark, where k is the average quark momentum and $P = \frac{1}{2}(p - p')$ is the average nucleon momentum;
- $t = (p' - p)^2 = \Delta^2$ is one of the three Mandelstam variables and represents the squared momentum transferred between the initial and final state of the nucleon;
- $\xi = -\dfrac{\Delta^+}{2P^+}$ is the skewness. $x + \xi$ is the longitudinal momentum fraction of the initial quark, while $x - \xi$ is the longitudinal momentum fraction of the final and reabsorbed quark. At leading order and in the Bjorken limit $\xi = \dfrac{x_B}{2 - x_B}$.

The GPDs are Fourier transform of non-local and non-diagonal QCD operators. Non-local means the initial and final quarks are created at different space-time coordinates, while non-diagonal refers to the momentum of the final nucleon being different than the momentum of the initial nucleon.

The variable x has a range of $[-1, 1]$, while ξ varies between $[0, 1]$. Therefore, three regions in x can be defined [45] (see figure 1.17):

- $x \in [-1, -\xi]$, the momentum fraction $x + \xi$ and $x - \xi$ are both negative and the GPDs describes the emission and re-absorption of an antiquark;
- $x \in [-\xi, \xi]$, the momentum fraction $x + \xi$ is positive, while $x - \xi$ is negative. This region exhibits the emission of a quark and re-absorption of an antiquark. Here the GPDs is limited to the probability amplitude of finding a $q\bar{q}$ pair in the nucleon;
- $x \in [+\xi, 1]$, the momentum fraction $x + \xi$ and $x - \xi$ are both positive and the GPDs describes the emission and re-absorption of a quark.

At leading twist and for a given quark flavor q, four chiral-even (meaning the helicity between the initial and final quarks is conserved) GPDs are introduced: $H^q(x, \xi, t)$, $E^q(x, \xi, t)$, $\tilde{H}^q(x, \xi, t)$ and $\tilde{E}^q(x, \xi, t)$. H^q and $\tilde{H}^q$ represent the GPDs when the helicity of the nucleon is preserved, while E^q and $\tilde{E}^q$ describe a flip. Moreover, H^q and E^q are defined by the sum of the quark and nucleon helicity states and therefore independent on the quark helicity; they are called unpolarized GPDs. $\tilde{H}^q$ and $\tilde{E}^q$ designate the helicity dependent polarized GPDs and are expressed by the difference of the quark and nucleon helicity states. Figure 1.18 highlights the four combinations of quark and nucleon of the GPDs.

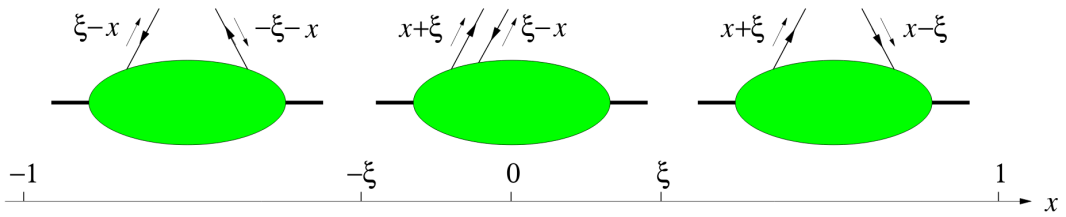

FIGURE 1.17 – The parton interpretation of GPDs in the three x-intervals [-1,$-\xi$], [$-\xi$,ξ], and [ξ,1]. Figure from [45].

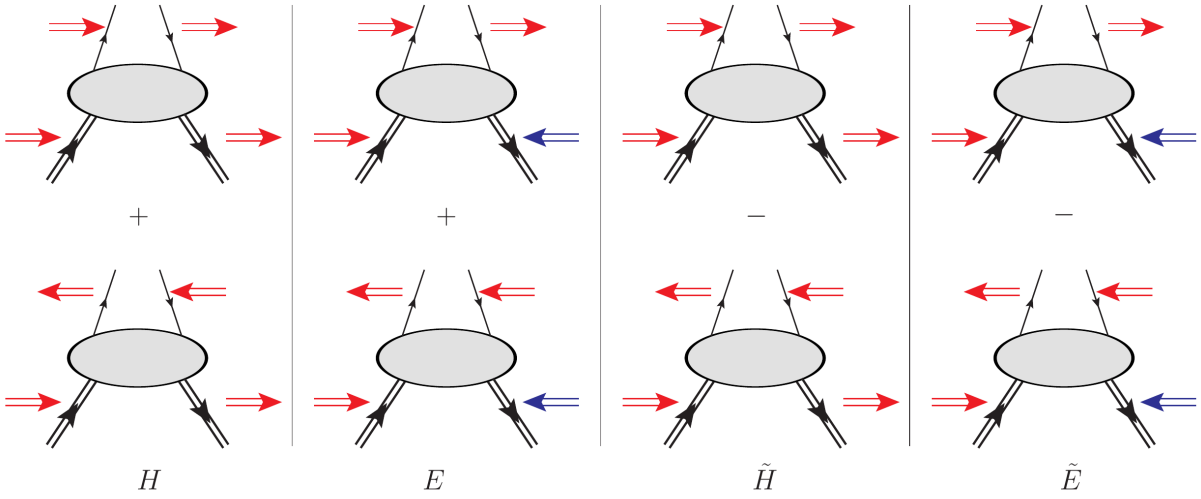

FIGURE 1.18 – The four GPDs H, E, $\tilde{H}$ and $\tilde{E}$ corresponding to the various quarks helicity and nucleon spin configurations.

Optical Theorem and Link with the PDFs

The GPDs are scattering amplitudes and in the forward limit ($\Delta = 0$), the optical theorem links H and $\tilde{H}$ to the unpolarized PDFs (q and $\bar{q}$) and polarized PDFs (Δq and $\Delta\bar{q}$) [46]:

$$H^q(x,0,0) = \begin{cases} q(x), & x > 0 \\ -\bar{q}(-x), & x < 0 \end{cases} \tag{1.21}$$

$$\tilde{H}^q(x,0,0) = \begin{cases} \Delta q(x), & x > 0 \\ -\Delta\bar{q}(-x), & x < 0 \end{cases} \tag{1.22}$$

1.4.b – Moments of GPDs and Polynomiality

Another property, which can be linked to Lorentz invariance is that the integration of the moment x^n of GPDs can be expressed as a polynomial in ξ [47]:

$$\begin{aligned} \int_{-1}^{+1} dx\, x^n H^q(x,\xi,t) &= a_0(t) + a_2(t)\xi^2 + a_4(t)\xi^4 + ... + a_n(t)\xi^n \quad \text{for } n \text{ even} \\ \int_{-1}^{+1} dx\, x^n H^q(x,\xi,t) &= a_0(t) + a_2(t)\xi^2 + a_4(t)\xi^4 + ... + a_{n+1}(t)\xi^{n+1} \quad \text{for } n \text{ odd} \end{aligned} \tag{1.23}$$

For finite momentum transfer t, the first moment of GPDs ($n = 0$) is related to the FFs and does not depend on ξ [48]:

$$\int_{-1}^{+1} dx H^q(x,\xi,t) = F_1^q(t), \qquad \int_{-1}^{+1} dx E^q(x,\xi,t) = F_2^q(t), \tag{1.24}$$

$$\int_{-1}^{+1} dx \tilde{H}^q(x,\xi,t) = G_A^q(t), \qquad \int_{-1}^{+1} dx \tilde{E}^q(x,\xi,t) = G_P^q(t) \tag{1.25}$$

where G_A^q and G_P^q are axial and pseudo-scalar FFs respectively. They are accessible in reactions where the elastic scattering occurs through the exchange of a neutral weak boson instead of a virtual photon.

1.4.c – Ji's Sum Rule

The spin of the nucleon can be decomposed as the sum of quarks and gluons contributions to the angular momentum of the nucleon, respectively J^q and J^g :

$$\frac{1}{2} = J^q + J^g \tag{1.26}$$

The total spin contribution of quarks can be expressed as $J^q = \frac{1}{2}\Delta\Sigma + L_q$, where $\frac{1}{2}\Delta\Sigma$ is the contribution of the quark spin to the nucleon spin and L_q is the contribution of the quarks orbital momentum to the nucleon spin. $\Delta\Sigma$ is the sum of all the quark flavors polarized PDF Δq measured using polarized DIS experiments: $\Delta\Sigma = \sum_i \int_{-1}^{+1} dx \Delta q_i(x)$. This term was measured experimentally and is estimated to be responsible for about 30% of the total spin of the nucleon [32].

In the forward limit ($t \to 0$), the total angular momentum carried by the quarks can be expressed using the GPDs second moment in x, this is known as the Ji Sum Rule [49].

$$J^q = \frac{1}{2}\sum_q \int_{-1}^{+1} dx\, x\, [H^q(x,\xi,0) + E^q(x,\xi,0)] \tag{1.27}$$

Similarly to the quarks and at small x, the gluon contribution J^g can also be calculated using Ji sum rule and the gluon GPDs following a similar formula as equation 1.27.

1.4.d – Impact Parameter

The momentum transfer Δ can be decomposed as two components : a longitudinal contribution Δ_L and a transverse contribution $\Delta_\perp$. When $\xi \to 0$, the longitudinal contribution Δ_L also tends toward zero and $t = \Delta_\perp^2$. It is possible to take a Fourier transform of $H^q(x, 0, \Delta_\perp^2)$ [50] [51] :

$$H^q(x, b_\perp) = \int \frac{1}{(2\pi)^2} e^{ib_\perp \Delta_\perp} H^q(x, 0, \Delta_\perp^2) \tag{1.28}$$

where the impact parameter $b_\perp$ is the quark transverse position.

Nucleon tomography is the study of GPDs where a 3-dimensional picture of the nucleon is drawn (2 spacial dimensions and 1 momentum dimension). Figure 1.19 illustrates and compare the information encoded in the FFs, PDFs and GPDs.

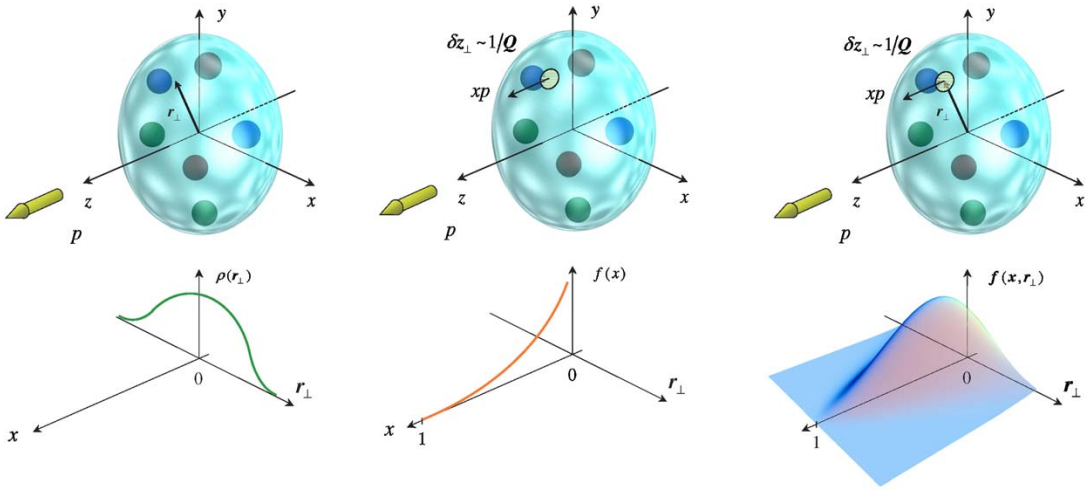

FIGURE 1.19 – Comparison between three structure functions. From left to right: the Form Factors accessible via Elastic scattering, the Parton Distribution Functions from Deep Inelastic Scattering, and the Generalized Distribution Function from Deep Exclusive Scattering (DVCS, DVMP, ...). Figure from [52].

1.5

Accessing the GPDs via DVCS

As seen previously, the GPDs depend on three variables: x, ξ and t. While ξ and t are experimentally accessible in DVCS, the variable x can not be extracted and is integrated over in the DVCS amplitude [46]. The following expressions are encoding the GPDs of the DVCS amplitude for spin 1/2 particles:

$$\begin{aligned}\mathcal{M}_{\text{DVCS}} \propto & \int_{-1}^{1} dx \left[\frac{1}{x-\xi+i\epsilon}+\frac{1}{x+\xi-i\epsilon}\right] \\ & \{\, H^n_{\text{DVCS}}(x,\xi,t)\bar{N}(p')\gamma n N(p) + E^n_{\text{DVCS}}(x,\xi,t)\bar{N}(p')i\sigma^{\kappa\lambda}\frac{n_\kappa \Delta_\lambda}{2m}N(p)\,\} \\ & + \int_{-1}^{1} dx \left[\frac{1}{x-\xi+i\epsilon}-\frac{1}{x+\xi-i\epsilon}\right] \\ & \{\, \tilde{H}^n_{\text{DVCS}}(x,\xi,t)\bar{N}(p')\gamma n\gamma_5 N(p) + \tilde{E}^n_{\text{DVCS}}(x,\xi,t)\bar{N}(p')\gamma_5\frac{\Delta\cdot n}{2m}N(p)\,\}\end{aligned} \tag{1.29}$$

The factor $\frac{1}{x\pm\xi\mp i\epsilon}$ arises from the quark operator and makes the integral complex. It is usually decomposed into a real part, which is the principal value integral, and an imaginary part:

$$\int_{-1}^{1} dx\, \frac{H(x,\xi,t)}{x-\xi\,\mathrm{i}\,\epsilon} = \mathcal{P}\int_{-1}^{1} dx\, \frac{H(x,\xi,t)}{x-\xi} - i\pi H(\xi,\xi,t) \tag{1.30}$$

1.5.a – Compton Form Factors

From equations 1.29 and 1.30, eight quantities only depending on ξ and t can be defined and are named Compton Form Factors (CFFs) [46]:

$$\mathcal{H}_{\mathrm{Re}}(\xi,t) = \mathcal{P}\int_0^1 dx\ \left[H(x,\xi,t) - H(-x,\xi,t)\right] C^+(x,\xi) \tag{1.31}$$
$$\mathcal{H}_{\mathrm{Im}}(\xi,t) = H(\xi,\xi,t) - H(-\xi,\xi,t)$$
$$\mathcal{E}_{\mathrm{Re}}(\xi,t) = \mathcal{P}\int_0^1 dx\ \left[E(x,\xi,t) - E(-x,\xi,t)\right] C^+(x,\xi) \tag{1.32}$$
$$\mathcal{E}_{\mathrm{Im}}(\xi,t) = E(\xi,\xi,t) - E(-\xi,\xi,t)$$
$$\tilde{\mathcal{H}}_{\mathrm{Re}}(\xi,t) = \mathcal{P}\int_0^1 dx\ \left[\tilde{H}(x,\xi,t) + \tilde{H}(-x,\xi,t)\right] C^-(x,\xi) \tag{1.33}$$
$$\tilde{\mathcal{H}}_{\mathrm{Im}}(\xi,t) = \tilde{H}(\xi,\xi,t) + \tilde{H}(-\xi,\xi,t)$$
$$\tilde{\mathcal{E}}_{\mathrm{Re}}(\xi,t) = \mathcal{P}\int_0^1 dx\ \left[\tilde{E}(x,\xi,t) + \tilde{E}(-x,\xi,t)\right] C^-(x,\xi) \tag{1.34}$$
$$\tilde{\mathcal{E}}_{\mathrm{Im}}(\xi,t) = \tilde{E}(\xi,\xi,t) + \tilde{E}(-\xi,\xi,t)$$

where $C^{\pm} = \frac{1}{x-\xi} \pm \frac{1}{x+\xi}$. The imaginary part of the CFFs represent the GPDs at the line $x = \pm\xi$.

1.5.b – DVCS Cross Section

The differential cross section for the electroproduction of photons is given by the following expression [40]:

$$\frac{d\sigma}{dx_B\, dy\, dt\, d\phi\, d\phi_e} = \frac{\alpha^3 x_B y}{16\pi^2 Q^2\sqrt{1+\epsilon^2}} \left|\frac{\mathcal{T}}{e^3}\right|^2 \tag{1.35}$$

where ϕ is the angle between the hadronic and leptonic planes (see figure 1.20 and [53] for the convention used), ϕ_e is the azimuthal angle of the scattered lepton, e is the elementary charge, $\mathcal{T}$ is the amplitude and $\epsilon = 2x_B\frac{m_N}{Q^2}$.

In addition to the DVCS, another process has to be included in the calculation of the amplitude $\mathcal{T}$: the Bethe-Heitler (BH) reaction. In this process, a photon is emitted by the incoming or the scattered electron, leading to a similar final state $ep \to e'p'\gamma$. Figure 1.21 shows Feynman diagrams of the DVCS and BH.

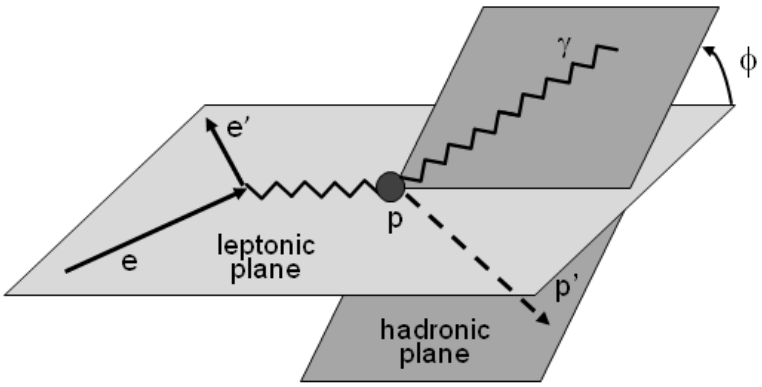

FIGURE 1.20 – 3D illustration of the leptonic and hadronic planes in DVCS, where ϕ is the angle separating the two planes.

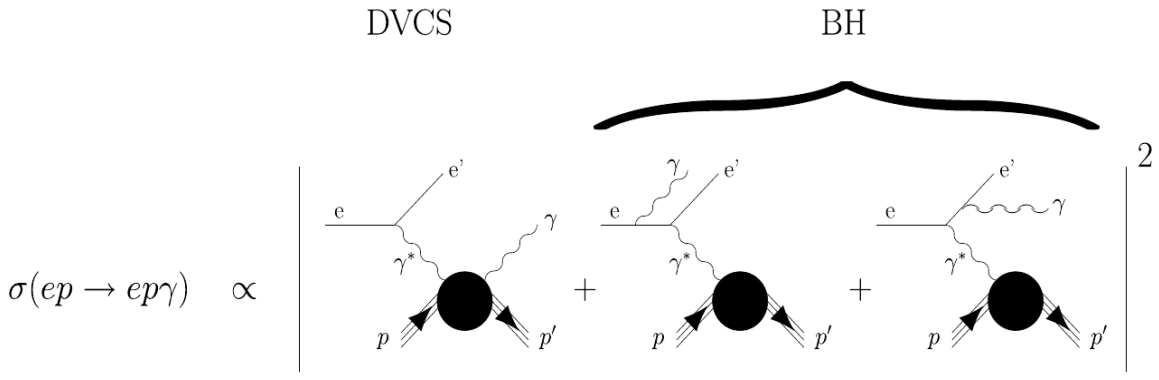

FIGURE 1.21 – Feynman diagrams at leading order of the reactions contributing to the cross section of the electroproduction of photons. Figure from [46].

The amplitude in equation 1.35 becomes:

$$\begin{aligned} |\mathcal{T}|^2 &= |\mathcal{T}_{DVCS} + \mathcal{T}_{BH}|^2 \\ &= |\mathcal{T}_{DVCS}|^2 + |\mathcal{T}_{BH}|^2 + \mathcal{I} \end{aligned} \tag{1.36}$$

where $\mathcal{I}$ is the interference term: $\mathcal{I} = \mathcal{T}_{DVCS}\mathcal{T}^*_{BH} + \mathcal{T}^*_{DVCS}\mathcal{T}_{BH}$.

At leading twist, the amplitudes of equation 1.36 can be decomposed, using the BMK[1] formalism [40], as a sum of Fourier harmonics:

$$\begin{aligned} |\mathcal{T}_{\mathrm{BH}}|^2 &= \frac{1}{x_B^2\, y^2\, (1+\epsilon^2)^2\, t\, \mathcal{P}_1(\phi)\mathcal{P}_2(\phi)} \left\{ c_0^{\mathrm{BH}} + \sum_{n=0}^{2} c_n^{\mathrm{BH}} \cos(n\phi) + s_n^{\mathrm{BH}} \sin(n\phi) \right\} \\ |\mathcal{T}_{\mathrm{DVCS}}|^2 &= \frac{e^6}{y^2\, Q^2} \left\{ c_0^{\mathrm{DVCS}} + \sum_{n=0}^{2} c_n^{\mathrm{DVCS}} \cos(n\phi) + s_n^{\mathrm{DVCS}} \sin(n\phi) \right\} \\ |\mathcal{I}|^2 &= \frac{\pm e^6}{x_B^2\, y^3\, t\, \mathcal{P}_1(\phi)\mathcal{P}_2(\phi)} \left\{ c_0^{\mathcal{I}} + \sum_{n=0}^{3} c_n^{\mathcal{I}} \cos(n\phi) + s_n^{\mathcal{I}} \sin(n\phi) \right\} \end{aligned} \tag{1.37}$$

where $\mathcal{P}_1(\phi)$ and $\mathcal{P}_2(\phi)$ are BH propagators. A detailed definition and explanation of the Fourier harmonics coefficients c_n and s_n can be found in [40] and varies depending on experimental factors such as the target and beam polarizations. The BH Fourier coefficients are calculated using the Dirac and Pauli FFs.

1.5.c – Observables

The sensitivity to a specific CFF part depends on the experimental conditions. In the case of the scattering of a polarized beam on an unpolarized target, two quantities can be extracted: $\sigma_{\mathrm{unpol}} = \sigma^+ + \sigma^-$ and $\sigma_{\mathrm{pol}} = \sigma^+ - \sigma^-$, where the $+$ and $-$ sign represent opposite beam helicities. As discussed previously and illustrated in figure 1.18, the GPDs describe a combination of quark/nucleon helicity configurations. For the most part, the cross section σ_{unpol} gives access to the real part of the amplitude $\sigma_{\mathrm{unpol}} \propto |\mathcal{T}_{\mathrm{BH}}|^2 + 2\,\mathcal{T}_{\mathrm{BH}}\ \mathrm{Re}(\mathcal{T}_{\mathrm{DVCS}}) + |\mathcal{T}_{\mathrm{DVCS}}|^2$, while σ_{pol} is sensitive to the imaginary part $\sigma_{\mathrm{pol}} \propto 2\,\mathcal{T}_{\mathrm{BH}}\ \mathrm{Im}(\mathcal{T}_{\mathrm{DVCS}})$.

This work will extract Beam Spin Asymmetries (BSA) which offers some advantages over the cross section observables introduced above: it can be expressed as a linear combination of CFFs and it has the advantage of canceling some normalization factors, such as the detector acceptance. BSAs - also written A_{LU} - are defined as:

[1] Belitsky-Müller-Kirchner

$$A_{\mathrm{LU}} = \frac{\sigma^{+} - \sigma^{-}}{\sigma^{+} + \sigma^{-}} \tag{1.38}$$

The first and second subscript letters are the polarization states of the beam and target respectively. The letter 'L 'means that the beam/target is longitudinally polarized and 'U' indicates an unpolarized beam/target. Beam Spin Asymmetry (BSA) A_{LU} is mostly sensitive to $\mathcal{H}_{\mathrm{Im}}$, the Target Spin Asymmetry (TSA) A_{UL} to $\mathcal{H}_{\mathrm{Im}}$ and $\tilde{\mathcal{H}}_{\mathrm{Im}}$, and the Double Spin Asymmetry (DSA) A_{LL} to $\mathcal{H}_{\mathrm{Re}}$ and $\tilde{\mathcal{H}}_{\mathrm{Re}}$.

1.6

The eg6 Experiment

The eg6 experiment took place at Jefferson Laboratory in 2009 and was the first experiment dedicated to measure nuclear DVCS on helium-4 using the 6 GeV electron beam. It used the CLAS detector with a similar setup as the eg1-dvcs experiment, which is the focus of this work. In addition to the standard CLAS detectors, the eg6 experiment used a Radial Time projection Chamber (RTPC), located around the target area, in order to detect low energy recoiled nucleus. By measuring the recoiled helium nucleus, the eg6 experiment measured both the coherent ($e^{4}\mathrm{He} \rightarrow e'^{4}\mathrm{He}'\gamma$) and the incoherent ($ep_{^4He} \rightarrow e'p'\gamma$) DVCS channels.

Since Helium-4 is a spin-0 nucleus, only two GPDs have to be measured in the coherent channel. The incoherent channel was also measured and the results of the eg6 analysis will be presented below and we will discuss how they motivate the present work [44].

Figures 1.22 and 1.23 represent the asymmetries at 90° along result from the HERMES experiment [54] and theoretical predictions. Finally, the ratio of asymmetries at 90° between the incoherent nuclear DVCS and DVCS on free proton is presented in figure 1.24. As the EMC effect, this test is used to highlight nuclear effects using DVCS and GPDs.

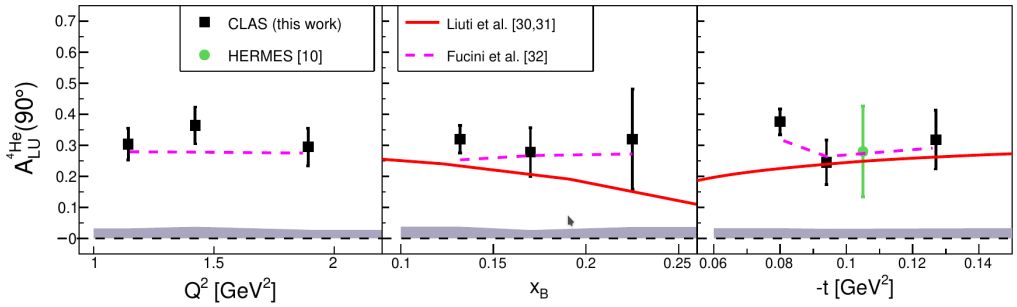

FIGURE 1.22 – $A_{LU}^{coherent}$ at 90°, as a function of Q^2, x_B and -t. The black points are the result of the eg6 experiment with the error bars being the statistical uncertainty and the grey band being the systematic uncertainty [55]. The green points are the result of the HERMES experiment [54]. The red line is one theoretical calculation by Liuti et al. [56] and the magenta line is the theoretical calculation by Fucini et al. [57]

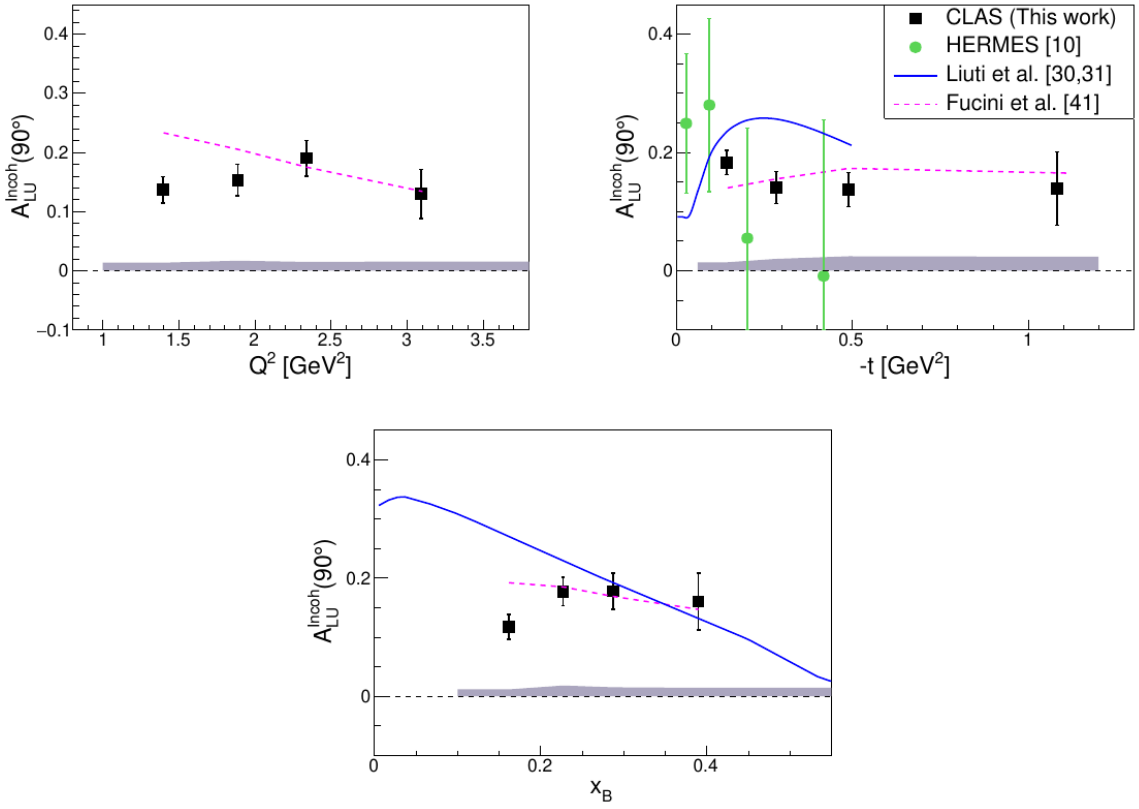

FIGURE 1.23 – $A_{LU}^{incoherent}$ at 90°, as a function of Q^2, x_B and -t. The black points are the result of the eg6 experiment with the error bars being the statistical uncertainty and the grey band being the systematic uncertainty [55]. The green points are the result of the HERMES experiment [54]. The blue line is one theoretical calculation by Liuti et al. [56] and the magenta line is the theoretical calculation by Fucini et al. [58]

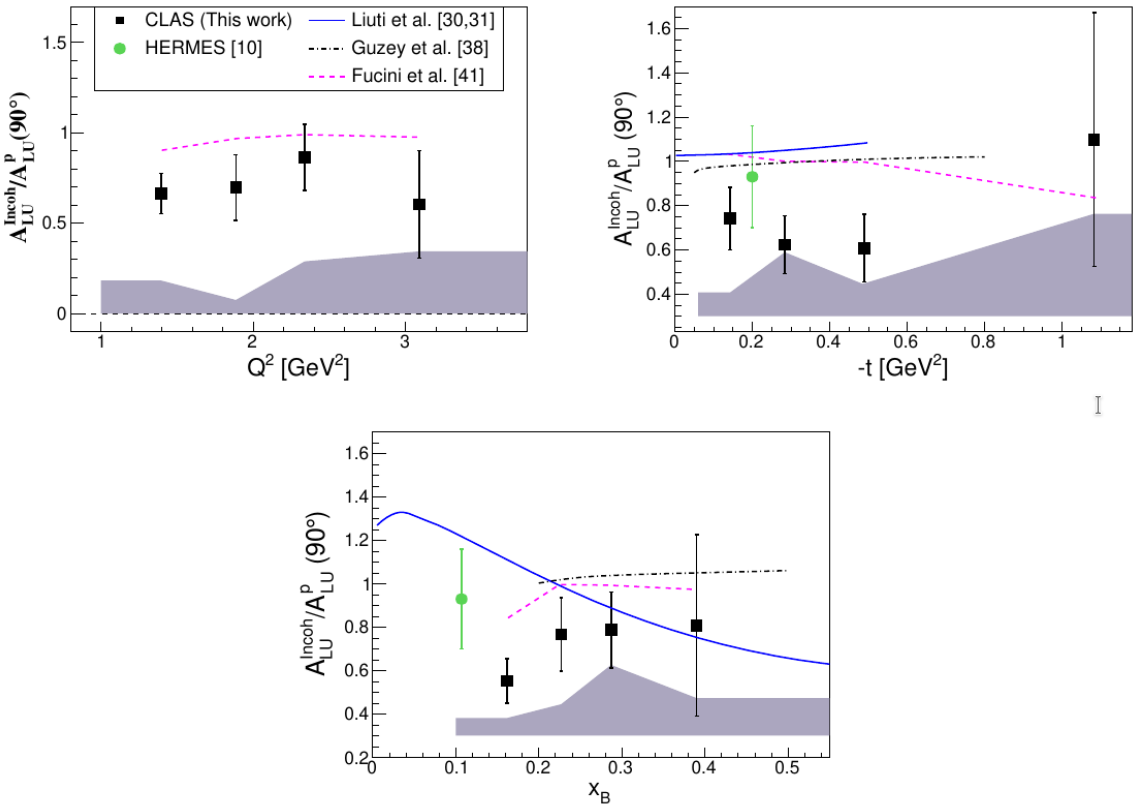

FIGURE 1.24 – Ratios of A_{LU} at 90° between bound nucleons and free nucleons, as a function of Q^2, x_B and -t. The black points are the result of the eg6 experiment with the error bars being the statistical uncertainty and the grey band being the systematic uncertainty [55]. The green points are the result of the HERMES experiment [54]. The blue line is one theoretical calculation by Liuti et al. [56], the black line is the results from Guzey [59], and the magenta line is the theoretical calculations by Fucini et al. [58]

CHAPTER 2

The CLAS detector at Jefferson Laboratory

The eg1-dvcs experiment took place in 2009 at the Thomas Jefferson National Accelerator Facility (Jefferson Lab or JLab), in Virginia, USA. This chapter will begin by giving a brief overview of the Continuous Electron Beam Accelerator Facility (CEBAF), Jefferson Laboratory's main accelerator, and will then focus on the CEBAF Large Acceptance Spectrometer (CLAS) where the experiment was carried out. Designed to measure DVCS events on polarized protons, the eg1-dvcs experiment required non-standard CLAS instruments; a solenoid, a longitudinally polarized target and an inner calorimeter were added to the apparatus.

2.1

The Continuous Electron Beam Accelerator Facility

Jefferson Laboratory was founded in the mid-1980s as the Continuous Electron Beam Accelerator Facility to study nuclear matter and its fundamental structure. At the time of completion, CEBAF was one of the first large scale accelerators to use Superconducting Radio Frequency (SRF) technology to accelerate electrons. The original design was an accelerator capable of delivering a 4 GeV electron beam to three different experimental halls (A, B and C) simultaneously. In 1994, the first 4 GeV beam was sent to hall C and was, in 2000, upgraded to 6 GeV. Another upgrade of the accelerator was completed in 2017 which doubled the beam energy to 12 GeV. The upgrade was also accompanied by the addition of a new experimental hall (Hall D) and an upgrade of the CLAS detector. We will discuss here the machine and detectors as they were at the time of the experiment.

Each experimental hall hosts unique instruments and has dedicated physics programs. Hall A and C are each equipped with two arm spectrometers extending outwards from the target which rotates around it depending on the angle of the particles being measured. The detectors were designed to achieve luminosities in the order of

10^{38}cm^{-2}s^{-1}. The two spectrometers of Hall A were identical and intended to measure the momentum of particles with high resolution, while Hall C had one spectrometer capable of measuring high momentum particles and another one focused on lower momentum particles. The CLAS detector was located in Hall B and had a larger acceptance. It was capable of identifying and measuring multiple particles in the final state with a luminosity in the order of 10^{34}cm^{-2}s^{-1}. More details on the CLAS detector will be given later in this chapter.

2.1.a – The Accelerator

The accelerator is mainly composed of three parts (see figure 2.1) : the injector, two linear accelerators (linacs) connected via recirculating arcs, and a beam switchyard. [60]

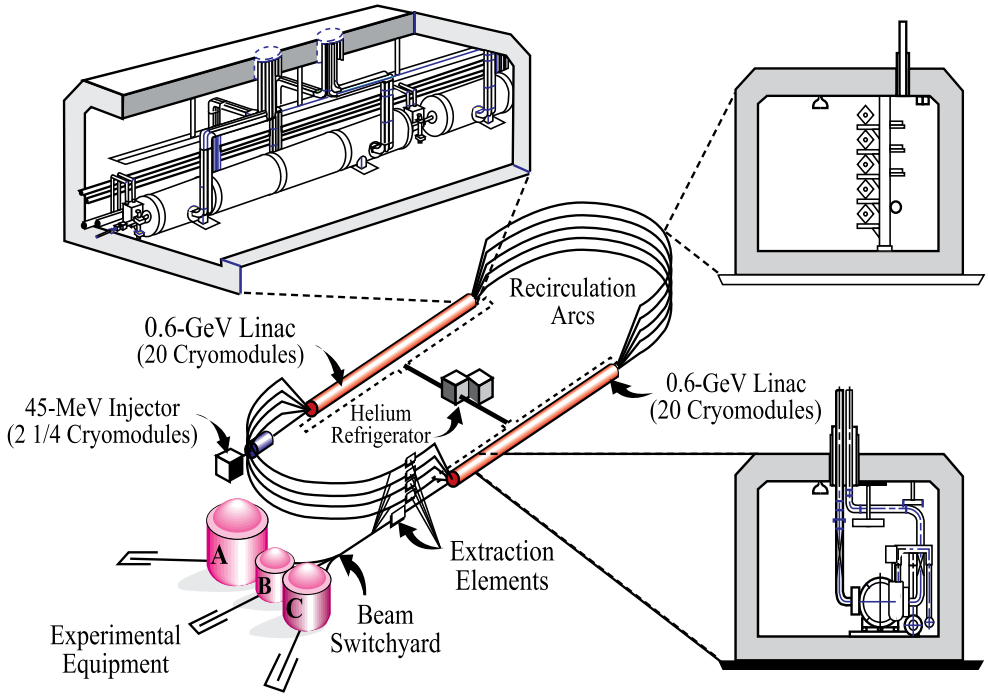

FIGURE 2.1 – Diagram of CEBAF at Jefferson Laboratory

The accelerator's injector produces electrons by pulsing a polarized laser on a Gallium Arsenide (GaAs) photocathode. This process creates 100 keV longitudinally polarized electrons [61]. The electrons then pass through a chopper which splits the beam into bunches of 499 MHz. To achieve beam delivery to the three halls simultaneously, three different lasers (one for each halls) are used to create interlaced beams (see figure 2.2). The result is a final 1497 MHz beam (3×499 MHz). Before sending the beams to the linacs, the bunches are accelerated using radio frequency (RF) cavities and reach an energy of 45 MeV. An important feature of this three laser configuration is the ability to tune the current sent to each experimental halls independently.

Next, the beam is fed to the north linac and starts a 1.4 km journey around the "race-

track" (nickname of the two linacs and circulating arcs because of their shape). Each linac pass increases the energy of the beam by 600 MeV. The linacs are composed of superconducting RF cavities bundled into 20 cryomodules. Since the accelerating cavities need to be as efficient as possible to avoid energy loss and heat, niobium was used for its superconducting properties. Indeed, when cooled down to 2 K, niobium becomes superconducting which allows the accelerator to run at a 100% duty cycle. In order to achieve and maintain this constant low temperature, the cavities inside cryomodule are surrounded by a bath of liquid helium provided by two helium refrigerators located onsite.

The recirculating arcs transport the beam between the linacs. Before reaching one arc, the beam is separated by a magnetic field depending on its momentum, it is then steered into the appropriate magnets to make a 180° turn. The electrons can travel up to 5 times around the accelerator to reach the desired energy, up to 6 GeV. Before delivery to the halls, a switchyard splits the 1497 MHz beam into three 499 MHz beams (corresponding to a continuous beam delivery with bunches every 2 ns) that are distributed to their respective halls. Table 2.1 summarizes some key parameters of the accelerator.

Electron energy, E [GeV]	$0.5 \leqslant E \leqslant 6.0$
Average Current [μA]	200
Transverse emittance (95%, 1 GeV) [m]	2×10^{-9}
Energy spread (95%)	1×10^{-4}
Duty factor	100%
Simultaneous beams	3
Simultaneous energies	$\leqslant 3$

TABLE 2.1 – Summary of CEBAF beam characteristics.

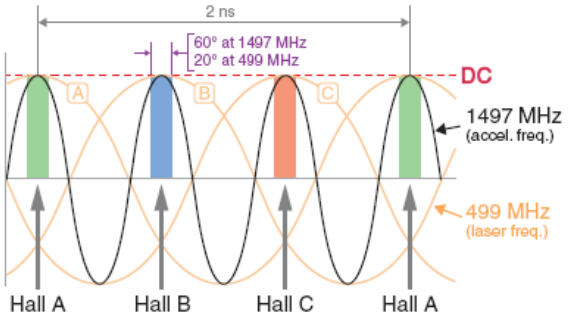

FIGURE 2.2 – Overview of CEBAF beam.

2.1.b – The Hall B Beamline

Once delivered to Hall B, the beam must be checked and monitored to ensure it meets the detectors and experiment requirements. Table 2.2 summaries the Hall B beam requirements and figure 2.3 gives an overview of the Hall B beamline. [62]

A Møller polarimeter, located upstream of the target is used to measure the beam polarization during dedicated runs. The beam interacts with an iron foil target of 25μm, which can be polarized longitudinally to the beam in either direction. Then, the recoiled electrons are deflected from the beam by a couple of quadrupole magnets and are measured by two scintillators located on both sides of the beamline. The beam polarization is calculated using the asymmetry between the two scintillator counts.

Beam Position Monitors (BPMs) are RF cavities allowing for a precise measurement

	Range	Precision	Monitor
Energy	$0.8 - 6.0$ GeV	$\delta E/E < 0.1\%$	Beam orbit stability
Polarization	$40 - 85\%$	$\delta P/P < 0.3\%$	Møller polarimeter
Position	± 3 mm off target center	100 μm	Beam Position Monitors
Width	$\sigma < 250$ μm	10 μm	Wire scans
Beam halo	1 : 100000		Wire scans
Current	$1 - 30$ nA	$< 1\%$	Faraday cup

TABLE 2.2 – Summary of the Hall B electron beam properties.

of the beam position and currents. Three BPMs, located upstream of the target, let the experiment operators check if the beam is centered and matches the current requirement. The current can also be cross-checked with the value obtained from the Faraday cup (which will be discussed shortly after).

Wires - arranged in devices called harps - move through the beam and measure the profile of the beam, giving information about its size and its position. These harps are made of tungsten and iron wires oriented in two orthogonal directions and perpendicular to the beam direction. The wires move using stepper motors and when the beam hits the wires, scattered electrons are detected by photomultiplier tubes (PMTs). A 2-dimensional picture of the beam is generated using the electron count from the PMTs and the wire location from the motors. Three harps are located upstream of the target.

Located right at the beam dump, the Faraday cup measures the current through an electrical feedback. This massive 4000 kg lead block is located downstream of the target and is also used to accurately calculate the accumulated charge (luminosity) over a given run period.

Finally, a raster system was installed for the eg1-dvcs experiment. Polarized targets lose polarization when heated. Therefore this raster system, composed of magnets, moves the beam in a circular pattern around the target. Later, the magnet setting information is used to correct the beam position on the target as well as the vertex of reconstructed particles.

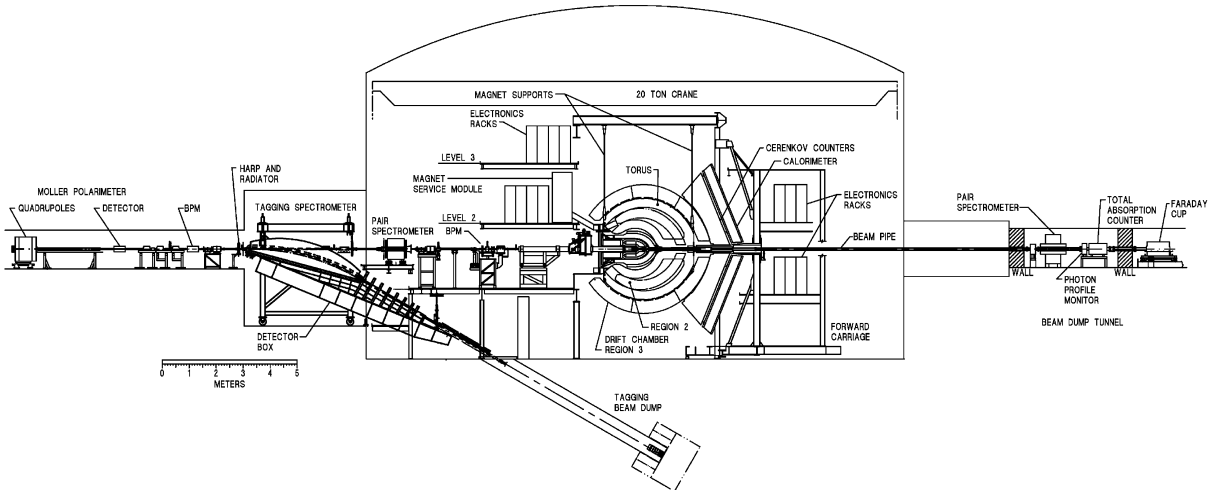

FIGURE 2.3 – Schematics of the Hall B beamline. Figure from [62].

2.2

CEBAF Large Acceptance Spectrometer

Traditional two arms spectrometers allow for smaller and optimized detectors. However they are limited in terms of the number of final particles being measured and phase space being covered. The 2π CEBAF Large Acceptance Spectrometer (CLAS) intends to fill that gap. Since its physics program is broad, ranging from spectroscopy to the study of the nucleon structure, the CLAS detector is tailored to cover a wide range of measurements. In order to reconstruct particles, key information are obtained from various detectors (see figure 2.4):

- charged particles trajectories are obtained from the drifts chambers (DC) located inside a magnetic field which is generated by the Torus magnet;
- electron, pion and photon energies can be measured with the electromagnetic calorimeters (EC);
- when the two previous values are not enough to dissociate the particle type between two candidates (for example between an electron and a negative pion), the Cherenkov counters (CC) can help to distinguished them.

2.2.a – The Torus Magnet

At the heart of CLAS is a toroidal superconducting magnet, creating an azimuthal magnetic field. The magnetic field bends charged particles toward or away from the

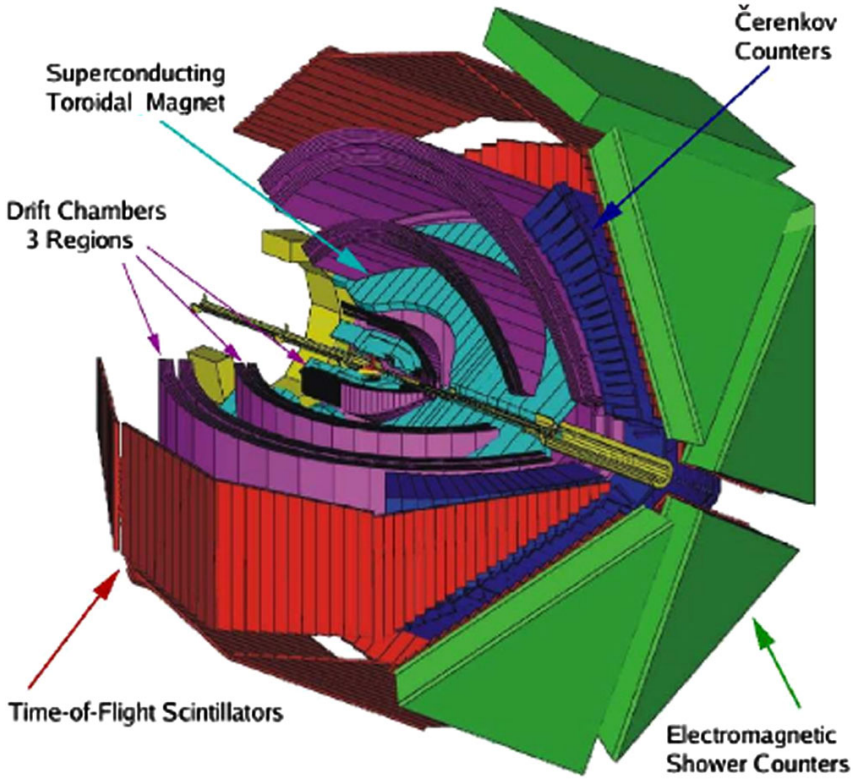

FIGURE 2.4 – Diagram of CLAS.

beamline without changing the azimuthal angle. The momenta of charged particles will also change the bending radius of the trajectories according to the following equation:

$$R = \frac{p}{q \times B}, \tag{2.1}$$

where R is the bending radius of the trajectory, B is the magnetic field, p is the momentum and q is the charge of the particle.

The toroidal field is generated by 6 kidney-shaped superconducting coils positioned symmetrically around the beam pipe creating 6 independent sectors inside which all the detectors are located [62]. The shape of the coils creates an integral magnetic field of 2.5 T m (at 3860 A) field in the forward direction and drops to 0.6 T m at 90° scattering. The figures 2.5 and 2.6 show the magnetic field configuration. Additionally, the polarity of current can be changed to bend the trajectories differently. Each configuration, in-bending or out-bending, depends on the experiment and the required acceptance for negative and positive particles.

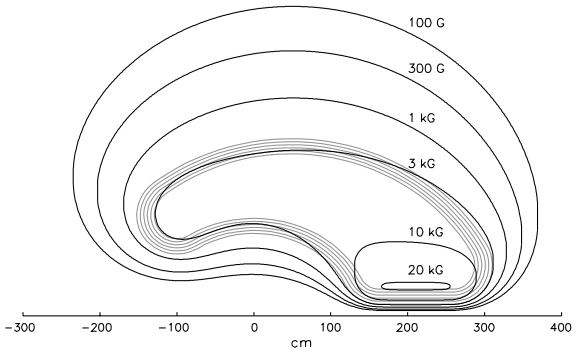

FIGURE 2.5 – Magnetic field contours between two coils and with the projection of a coil.Figure from [62]

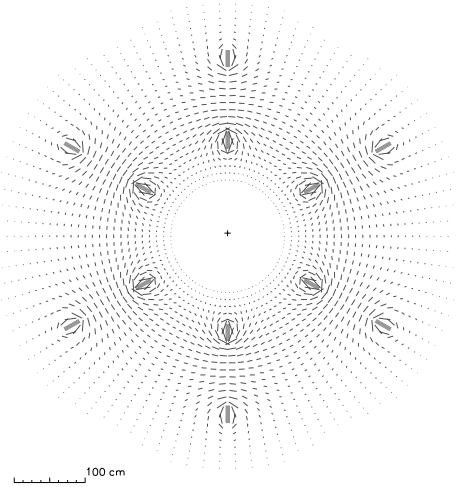

FIGURE 2.6 – Magnetic field vectors for the CLAS toroid transverse to the beam and centered on the target. The cross sections of the 6 coils are also shown. Figure from [62].

2.2.b – Drift Chambers

Each sector has 3 different drift chamber "regions" located at three different radial positions from the center of CLAS. Region 1 (R1) is the closest to the center and surrounds the target area, where the magnetic field is low. Region 2 (R2) is located in the center between two Torus coils, in an area of high magnetic field. Finally, Region 3 (R3) is located outside the coils (see figure 2.7). The drift chambers track particles of momenta over 200 MeV/c and with polar angles ranging from 8° to 142°, while covering up to 80% of the azimuthal angle [63].

Figure 2.8 shows the "two superlayers" design of the region 3 drift chambers. Each superlayer has six layers (execpt for the Region 1 drift chambers, which are made of four layers), and are composed of sense (anode) and field (cathode) wires. The sense wire sits at the center of a hexagon, with the corner of this hexagon being field wires. The honeycomb structure helps with the reconstruction while keeping a uniform electric field throughout the chamber. The wires in the neighboring superlayer are offset by a 6° stereo angle to obtain better azimuthal information about the particle.

A gas mixture of 90% argon and 10% CO_2 was used for its drift velocity and operating voltage properties. As a particle enters the drift chamber, the gas will ionize creating electron/ion pair. The difference of potential between the field and sense wire will cause the fast electrons to drift towards the sense wire, ionizing and generating new electrons in their path (creating an electron avalanche), while the heavy and slow ions drift toward the field wires. During the reconstruction, the wire location, as well as the drift time information, are used to calculate the particle trajectory with an average precision of 300 μm.

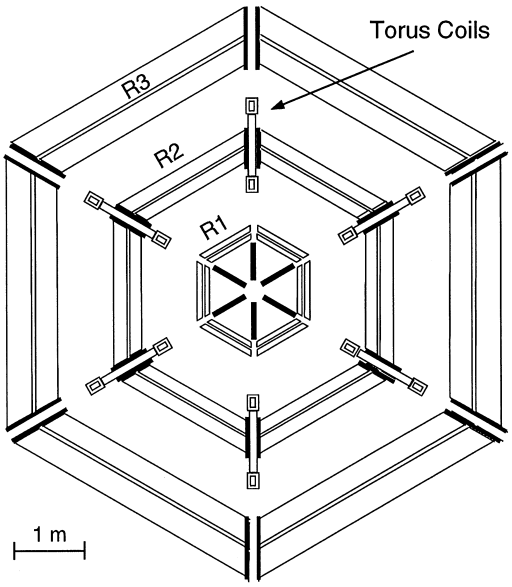

FIGURE 2.7 – Cross section of the CLAS drift chamber system along the beamline. Figure from [63].

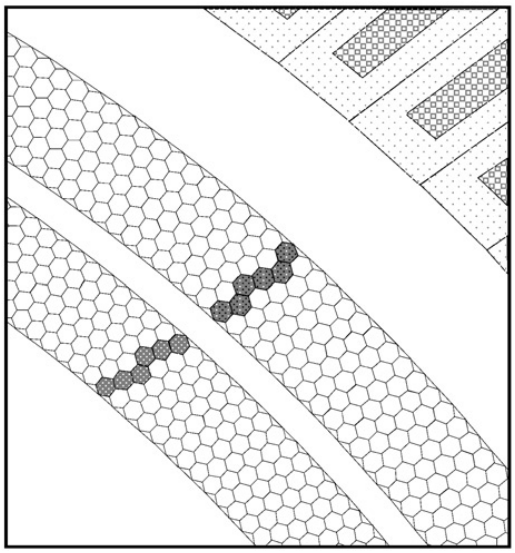

FIGURE 2.8 – Diagram of the region 3 drift chamber of CLAS. The shaded hexagons represent a reconstructed particle. Figure from [63].

2.2.c – Electromagnetic Calorimeters

The energy of electrons and photons is obtained with the electromagnetic calorimeters. The CLAS sampling calorimeter is an aggregation of alternating lead and scintillator layers, totaling to 16 radiation lengths, and covering the polar angle from 8° to 45°. Each sector of the EC is composed of 39 layers of 2.2 mm thick lead and 10 mm thick scintillators. Layers are stacked and alternatively rotated by 120° (see figure 2.9). These 3 orientations (u, v and w) provide stereo information on the location of the interaction [64].

Particles entering the EC will interact with lead, producing an electromagnetic shower which will be detected by the PMTs located at the edges of the scintillators. For analysis purposes, a distinction is made between the first 5 layers and the rest of the detector, namely the inner detector and outer detector respectively. Minimum ionizing particles, such as pions, will deposit their energy constantly along the EC, while electrons leave almost all their energy in the inner part of the EC. Therefore, dividing the EC in two parts helps with the identification of pions. The sampling fraction of the calorimeter is about 0.3 and corresponds to the ratio of the energy deposited in the scintillators to the total energy of the particle. The energy deposited is recorded, as well as the timing and position of the interaction. Table 2.3 highlights some of the parameters of the EC.

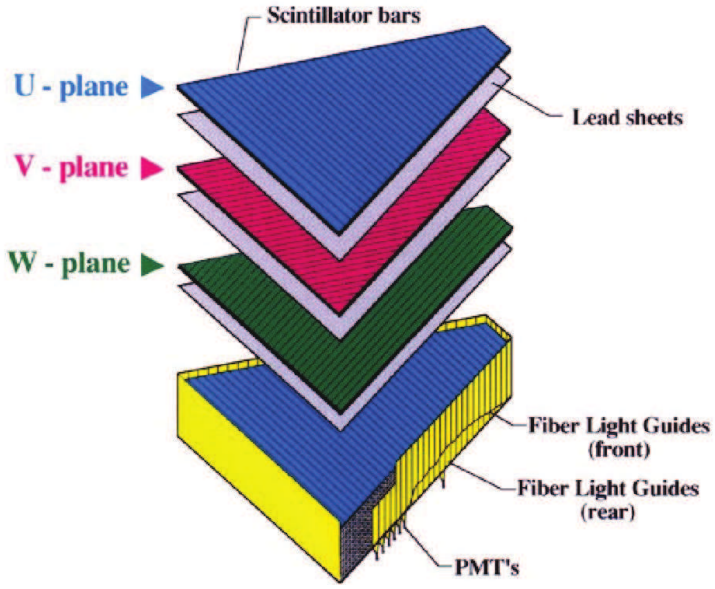

FIGURE 2.9 – Exploded view of one CLAS electromagnetic calorimeter. Figure from [64].

Minimum electron energy	500 MeV
Minimum photon energy	200 MeV
e/γ energy resolution	$\sigma/E \leqslant 0.1/\sqrt{E[GeV]}$
Position resolution	$\delta r \approx 2$ cm at 1 GeV
π/e rejection	$> 99\%$ at $E \geqslant 1$ GeV
Two photon decay mass resolution	$\delta m/m \leqslant 0.15$
Time-of-flight resolution	≈ 1 ns

TABLE 2.3 – Key parameters of the CLAS electromagnetic calorimeters.

2.2.d – Cherenkov Counters

In order to distinguish electrons from low energy ($E < 2.5$ GeV) negative pions, the Cherenkov counters (CC) must be used. Cherenkov light is emitted when a particle is traveling faster than the speed of light in a given medium ($\beta > c/n$, with n being the refractive index in that medium). The CLAS CCs measure the number of photo-electrons emitted by each particles passing through it [65].

Each sector's CC is composed of a mirror system focusing and steering the emitted Cherenkov light onto 36 PMTs located at the edge of the detector. The angular coverage of the CCs is up to 45° for polar angles and 80% for azimuthal angles. Figure 2.10 shows a typical electron event, while figure 2.11 is a schematic view of one CC sector.

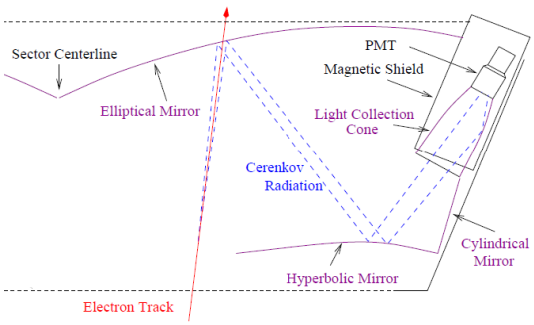

FIGURE 2.10 – Typical electron event measured by the CCs. Figure from [65].

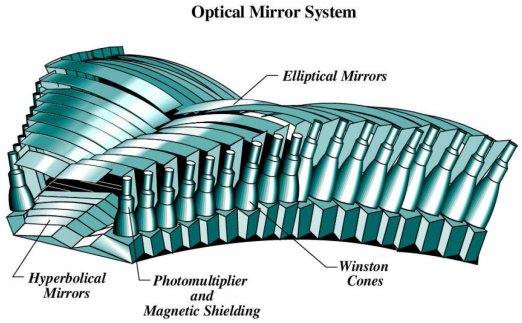

FIGURE 2.11 – Schematic view of one CC sector. Figure from [65].

Since the CCs need to help distinguish between electrons and negative pions below 2.5 GeV, the choice of gas is important. Perfluorobutane (C_4F_{10}) was chosen as the radiator gas. With a high refraction index (n = 1.00153), photons will be emitted for pion momenta greater than 2.5 GeV/c. The momentum threshold can be calculated for various particle masses (m_0) using the following formula:

$$p > \frac{m_0}{\sqrt{n^2 - 1}} \tag{2.2}$$

Timing and position information is also recorded and the CC system is also used as a trigger for electron scattering experiments.

2.2.e – *Scintillator Counters*

Scintillator counters (SC) are located beyond the drift chambers and offer a similar coverage (polar angles ranging from 8° to 142°). They measure precisely the particles time, allowing for the identification of different hadrons (π, K and p) when correlated with the momentum information from the DCs. The timing resolutions vary from 120 ps to 250 ps at large polar angles. The SCs are composed of scintillator paddles with PMTs attached at each end (see figure 2.12) [66].

The SCs can also be used to calculate the start time (electron time) of each event using the following formula :

$$t_{start} = t_{SC} - \frac{d_{SC}}{c}, \tag{2.3}$$

where t_{SC} is the measured time, and d_{SC} is the distance from the target to the interaction location on a scintillator paddle. This position information can be obtained by comparing the measured times of the two PMTs located at both ends of the scintillator.

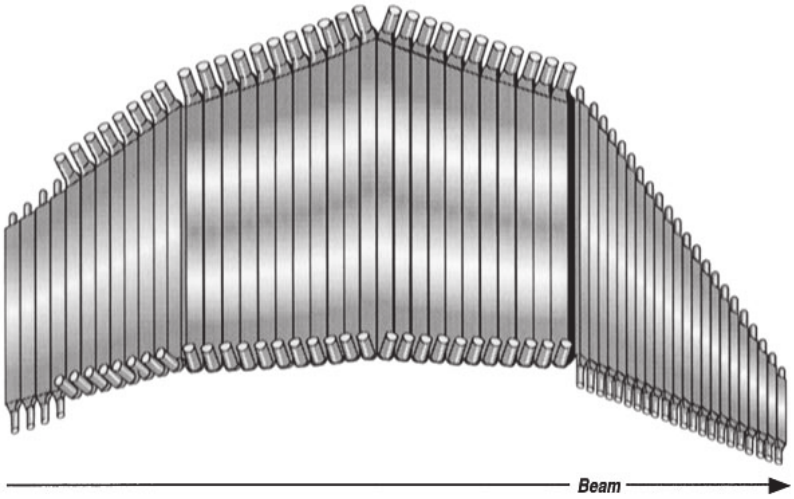

FIGURE 2.12 – Schematic drawing of one sector of the scintillator counter.Figure from [66].

2.2.f – Inner Calorimeter

In order to identify photons from DVCS events emitted at small angles, the eg1-dvcs experiment used an inner calorimeter (IC) located in the forward region and around the beamline. The IC is composed of 424 lead-tungsten ($PbWO_4$) crystals with an avalanche photo-diode at the end of each crystal. Located at 57.95 cm or 67.97 cm from the target depending on the experimental conditions of the eg1-dvcs runs, it offers a polar angle coverage between $\sim 4^\circ$ and $\sim 16^\circ$. Figures 2.13 and 2.14 are pictures of the inner calorimeter.

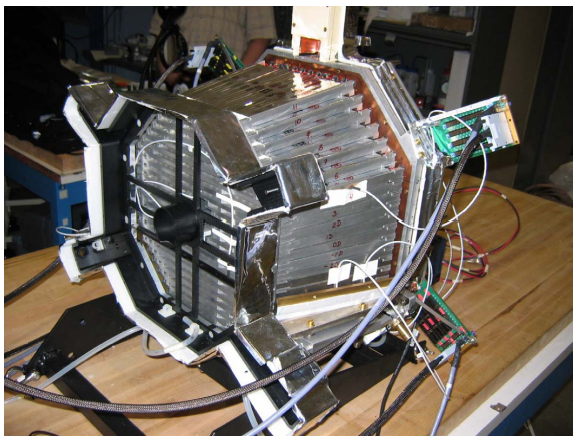

FIGURE 2.13 – Picture of the front of the inner calorimeter.

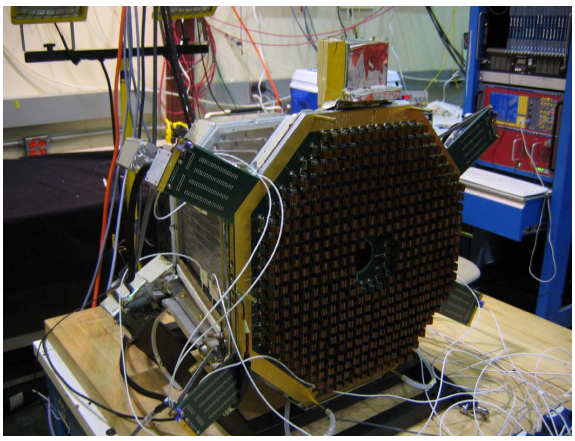

FIGURE 2.14 – Picture of the back of the inner calorimeter.

The IC can measure photons above 15 MeV with an energy resolution $\sigma/E \approx \sqrt{4}\%$ at 1 GeV.

2.2.g – *Polarized Target*

The eg1-dvcs experiment was designed to measure DVCS events from longitudinally polarized protons. Therefore a polarized target was added to the apparatus [67]. Solid state ammonia ($^{14}NH_3$) was used as a target and was polarized using dynamic nuclear polarization (DNP) (see figure 2.15). $^{14}NH_3$ was chosen for its high proton content, high polarization capability (> 90%) and resilience against radiation.

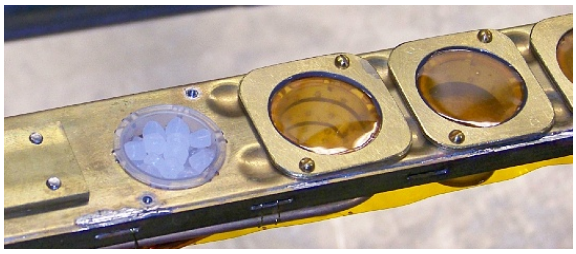

FIGURE 2.15 – Photography of the target insert with one cell being filled with $^{14}NH_3$.

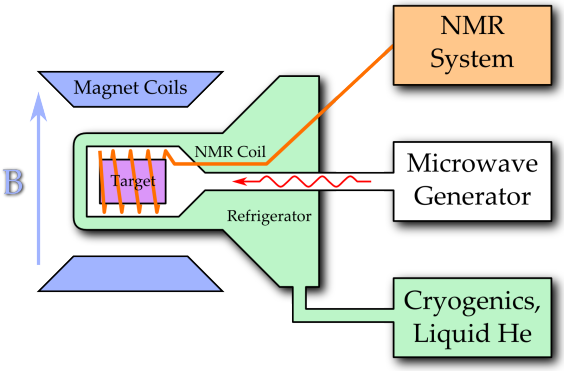

FIGURE 2.16 – Simplified diagram of a polarized target apparatus.

DNP relies on the transfer of polarization from the electron in $^{14}NH_2$ paramagnetic radicals to the $^{14}NH_3$ nuclei. Paramagnetic radicals are introduced by irradiating $^{14}NH_3$ beforehand. The unpaired electrons in the $^{14}NH_2$ can be easily polarized in a low temperature ($\sim$ 1 K) and high magnetic field environment ($\sim$ 5 T). Simultaneous spin flip of the electrons and nucleons can be induced using microwave. Since electrons have a shorter relaxation time than nuclei, the operation can be repeated to reach the desired polarization. Finally, the polarization of the target can the measured using Nuclear Magnetic Resonance (NMR). Figure 2.16 is a simplified diagram of the polarized target apparatus.

The polarized target was placed inside a Niobium-Titanium superconducting solenoid producing a 5 T magnetic field (parallel to the beam). It is a key component in the process of DNP used to polarize the target, but also helps to reduce noise in the region 1 DCs. Indeed, low energy Møller electrons are produced when the beam interacts with electrons from the target. These Møller electrons can make it to the region 1 DCs, hence increasing their occupancies. The solenoid bends the low energy electrons to small polar angles and therefore deflects them along the beamline and in the forward direction.

The eg1-dvcs experiment polarized target also required the installation of:

- a liquid helium refrigerator to cool down the magnet and the target. Figure 2.17 is a diagram of the target cooling system;

- a tunable microwave system;
- a NMR system to monitor the polarization by measuring the impedance of the inductor surrounding the target.

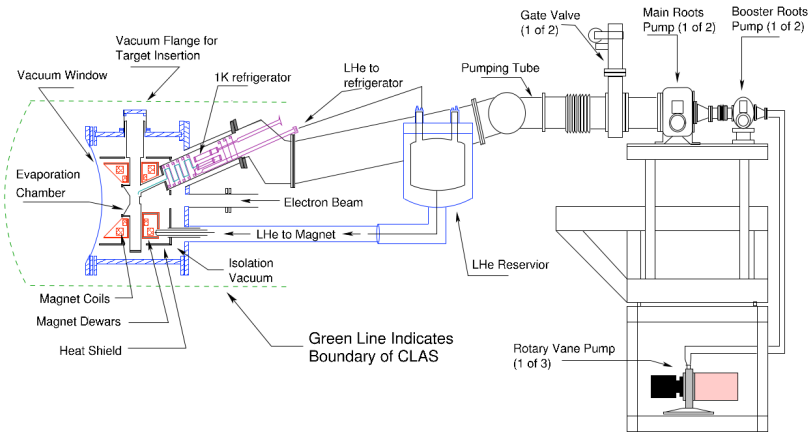

FIGURE 2.17 – Layout of the polarized target cryostat. Figure from [67].

2.2.h – *Trigger*

The CLAS data acquisition (DAQ) used two levels trigger system. The level 1 trigger gathers information from fast detectors such the EC, CC and SC. When energy is deposited in the EC and a signal from the PMTs of the CCs passed a set threshold, the event is flagged as a potential candidate. The level 2 trigger monitors the DCs and is activated when probable tracks are found and if the level 1 trigger was initiated. In the case both conditions are met, the event is saved, otherwise the signals are unused and cleared [62].

CHAPTER 3

Particle Identification

The eg1-dvcs experiment took data from January to September 2009, and was divided in three parts (A, B and C). Part A and B used the $^{14}NH_3$ polarized target at various detector settings and beam energies, while part C used a $^{14}ND_3$ polarized target to measure neutron DVCS. The part C data was not included in this analysis. Data using a carbon target was also taken, in order to estimate and remove the background from the nitrogen events in the analysis on the proton. About 10% of part A an B was taken using a carbon target. Table 3.1 summarizes the experiment configuration for part A and B.

Part	Beam Energy [GeV]	Target z position [cm]	Torus current [A]	Run Numbers
A	5.887 4.730	-57.95	2250.0	[58708 - 59161] [59162 - 59220]
B	5.887	-67.97	2250.0 -2200.0	[59221 - 59977] [60006 - 60184] [59978 - 60005]

TABLE 3.1 – Experimental configuration of part A and B of eg1-dvcs.

To identify incoherent DVCS events, three particles must be detected : the scattered electron, the recoiled proton and a real photon. This sections describe how the data is prepared before explaining how the final particles are identified, following the same procedure used by the original proton DVCS analysis [68].

3.1

Preparing the Data

3.1.a – Reconstruction and Skimming

The raw data from the CLAS detectors need to be reconstructed into more useful and more practical variables. During this step of the analysis, Time-to-digital (TDC) and charge-to-digital (QDC) values are being corrected, using each detector calibration, and converted into observables such as particle hits, energy deposited, etc. Variables, such as the momentum and charge, are also calculated and stored.

Once this conversion happened, the large amount of data needs to be reduced in order to remove unwanted events and efficiently perform the analysis. A filtering program "nt22maker" is used to achieve this need. nt22maker creates root files for each run and stores the information if at least one electron, one proton and one photon candidate are found and match the following conditions :

Electron

- Charge $q = -1$. The charge is calculated using the curvature of the particles trajectories in the drift chambers, sitting in a magnetic field;
- Information available in the DCs, CCs and ECs. This condition ensures that the particles pass the minimum threshold set for each detectors, matching an electron candidate;
- Momentum $p > 0.5$ GeV/c;
- Ratio of the energy deposited and momentum $E_{EC}/p > 0.2$;
- The angular match between the CC and SC: $CC_{C2} < 0.15$. This cut avoids random coincidences as electrons are expected to hit the SC at maximum 2 paddles away from from the trajectory matching a hit in the CC.

Proton

- Charge $q = 1$. As for the electrons, the proton trajectories measured by the DC are curved in the magnetic field. The orientation of the curvature is opposite to the electrons;
- Momentum $p > 0.5$ GeV/c/

Photon

- From the EC:
  - Charge $q = 0$
  - Energy $E > 0.2$ GeV
- From the IC:
  - Energy $E > 0.1$ GeV

3.1.b – Data Quality

Before proceeding to the particle identification, the quality of the data is checked for missing information in the online database or DAQ issues. For example, if no target polarization or Faraday cup information is found, the files are discarded.

Finally, an electron rate study was performed by grouping runs with similar experimental conditions and calculating the electron rates. Then, an abnormal rates is defined if a file rate falls beyond 5σ of the mean electron rate for its group, indicating a malfunction in the detectors. Files matching this description are also discarded. Details about this process can be found in [69].

3.1.c – Raster Correction

As explained in section 2.1.b, the polarization of the target will drop if the beam hits at the same spot. To remedy this situation, a set of raster magnets are installed right before the target to slightly move the beam circularly around the target material. The magnets currents are saved (in the form of an ADC values) and the beam position (in x and y) at the target is corrected. Finally, momenta are recalculated using this new beam position and the information from the DCs [70]. Figure 3.1 shows the target z-vertex position versus ϕ, before and after the raster correction, for negative particles.

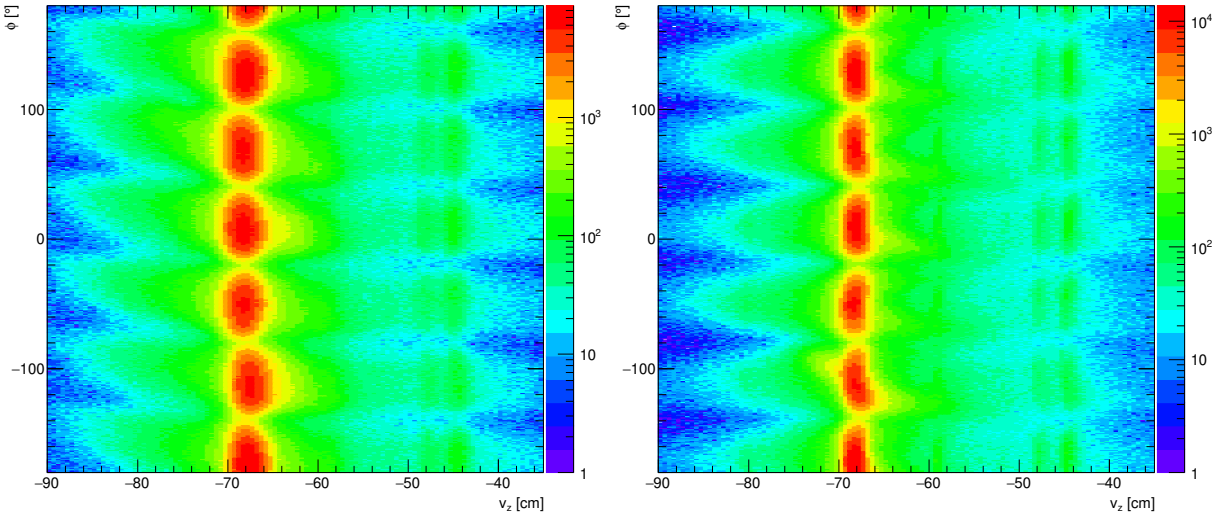

FIGURE 3.1 – Reconstructed z-vertex for negative particles before (left) and after (right) the raster correction.

3.2

Electron Identification

The electron identification cuts are chosen to meet two main requirements: separate electrons from negative pions (π^-) and reject particles hitting the edges of a detector where its efficiency is lower. Hence the particle hitting the edges have a high probability of being erroneously reconstructed, making the identification unreliable in this region. Table 3.2 lists all the variables and cuts applied to identified electrons. The cuts will be discussed in the following subsections.

Variable	Cut
Charge	q = -1
Momentum	$p > 0.8$ GeV/c
Inner EC energy	$E_{EC,inner} > 0.06$ GeV
Vertex	$\lvert v_z - z_{target}\rvert \leqslant 3$ cm
Timing	$\lvert t_{CC} - t_{SC}\rvert \leqslant 2$ ns
EC fiducial cuts	$40 < u < 400$ cm $0 < v < 360$ cm $0 < w < 390$ cm IC shadowing cuts

TABLE 3.2 – Summary of all electron identification cuts.

3.2.a – Momentum Cut

The Electromagnetic Calorimeter was designed to detect particles above 0.5 GeV/c, and is less efficient at low momentum. Therefore, a cut at $p > 0.8$ GeV/c is applied to ensure a reliable energy reconstruction of the electrons, as well as to minimize radiative effects such as Møller electrons and electrons from secondary interactions.

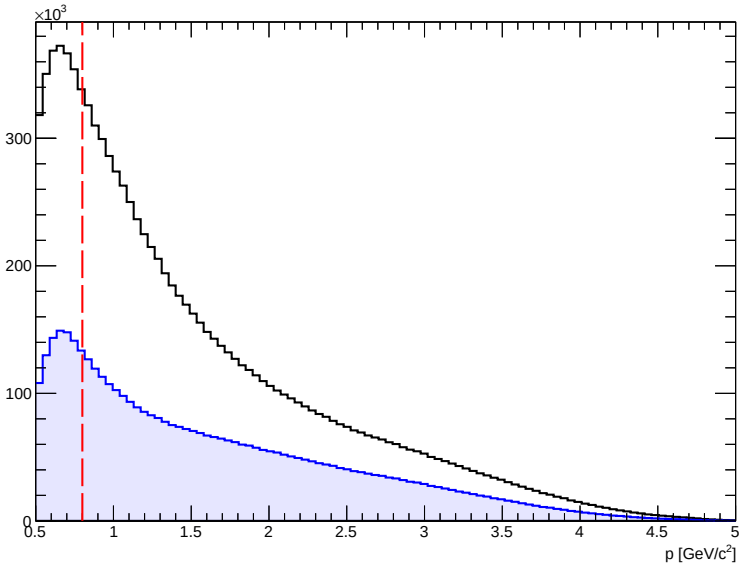

FIGURE 3.2 – Momentum distributions of negatively charged particles. The blue histogram is the momentum distribution with all the electrons identification cuts except the momentum cut, while the black histogram is the same distribution without any cuts. The red line is the cut at $p = 0.8$ GeV/c.

3.2.b – EC Energy Cut

Pions are considered minimum ionizing particles (MIPs) and will deposit energy while passing through a detector around 2 MeV/cm. Since the inner part of EC is 15 cm in thickness, pions going through this detector will deposit on average 30 MeV. Figure 3.3 shows the deposited energy of negative particles in the inner EC. A peak at 30 MeV is clearly visible, therefore a cut at 60 MeV is applied to remove the pions. Figure 3.3 also illustrates how the other cuts applied remove a significant number of pions in our data.

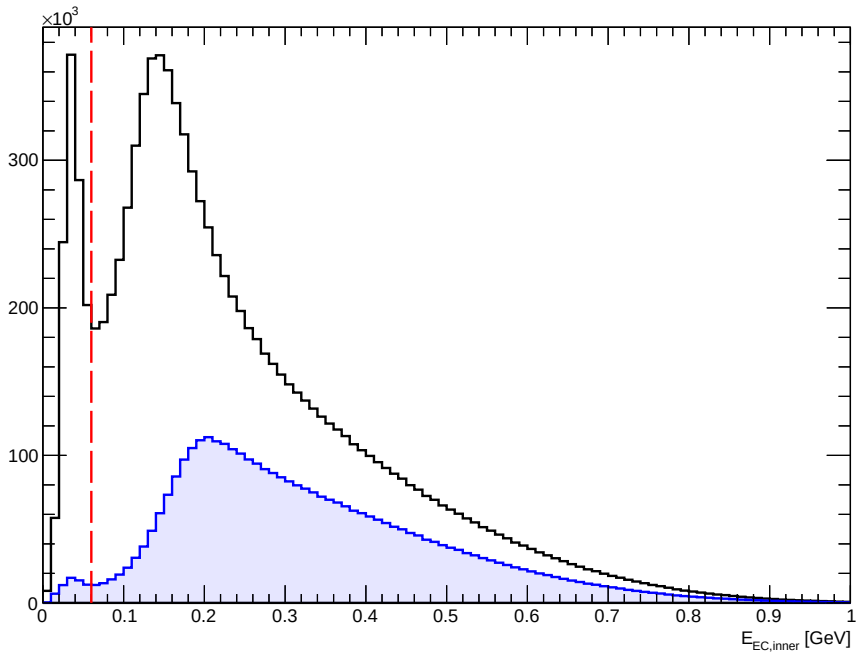

FIGURE 3.3 – Distributions of deposited energy in the inner part of the EC ($E_{EC,\,\text{inner}}$) for negatively charged particles. The blue histogram is the distribution with all the electrons identification cuts except the $E_{EC,\,\text{inner}}$ cut, while the black histogram is the same distribution without any cuts. The red line is the cut at $E_{EC,\,\text{inner}} = 0.06$ GeV/c^2.

3.2.c – Vertex Cut

A cut on the z-component of the reconstructed vertex ensures that reconstructed events are the product of an interaction happening inside the target and not interactions of the beam with materials outside the target. The cut is defined as $|v_z - z_{\text{target}}| \leqslant 3$ cm, where v_z is the reconstructed vertex with respect to the center of CLAS and its coordinate system, and where z_{target} is the distance from the nominal center of CLAS to the target (see table 3.1). Figure 3.4 shows a 1 dimension distribution of the z-coordinate of the corrected vertex ($|v_z - z_{\text{target}}|$), and a 2 dimension histogram of the same quantity versus ϕ.

3.2.d – Timing Cut

A cut on the time difference between the SC and CC is applied to discard random coincidences and ensure that the identified electron belongs to the correct event. A new variable Δt_{CC-SC} is defined as:

$$\Delta t_{CC-SC} = t_{CC} - \frac{r_{CC}}{c} - \left(t_{SC} - \frac{r_{SC}}{c}\right) \tag{3.1}$$

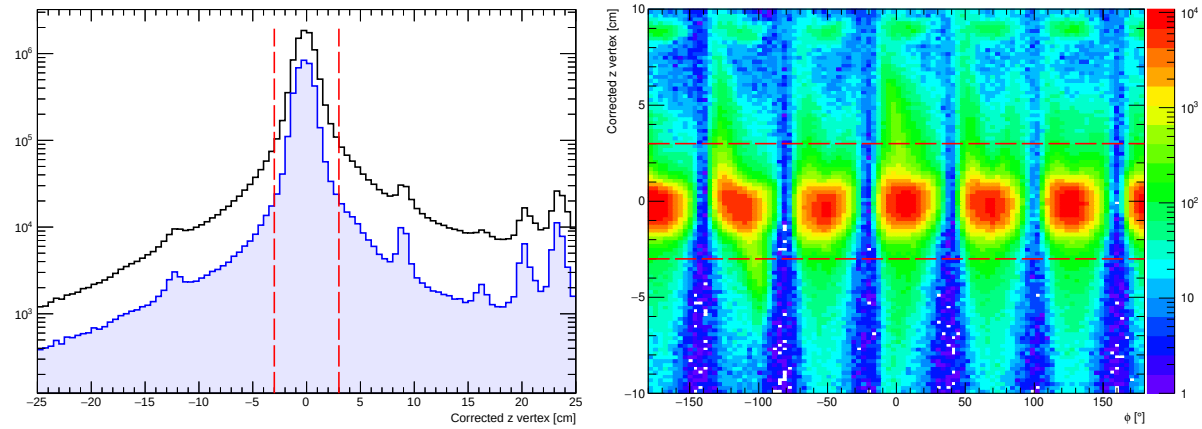

FIGURE 3.4 – Reconstructed z-vertex for negative particles (left) : the blue distribution is all negative particles after the electron identification cuts except the $|v_z - z_{target}| \leqslant 3$ cm (logarithmic scale), and the black histogram is the same distribution without any cuts. On the right is a 2 dimensional histogram with the reconstructed vertex distribution (same as the blue histogram on the left) versus the angle ϕ. The six sectors of CLAS are well identified in the plot.

where t_{CC} and t_{SC} are respectively the hit time since the start of the event for the Cherenkov counters and the scintilator counters. Similarly, r_{CC} and r_{SC} are the path length between the target and each detector. A 4 ns window centered around 0 helps removing pileups, particles from multiple additional interactions (see figure 3.5).

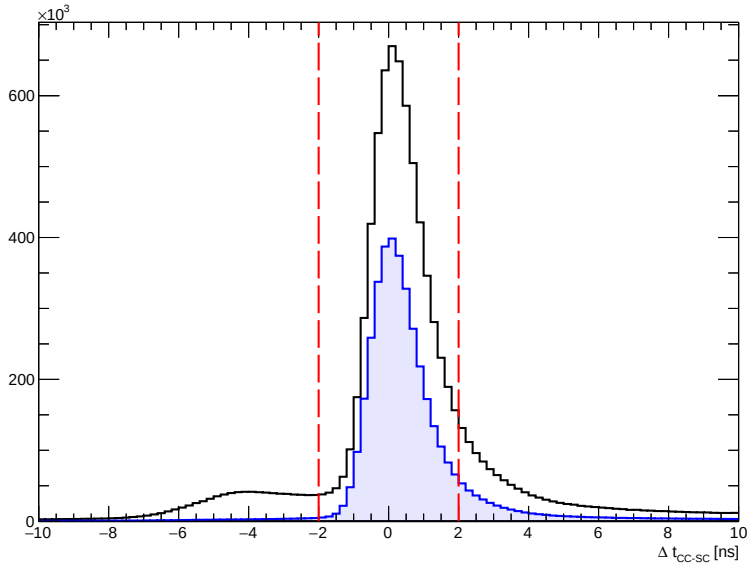

FIGURE 3.5 – Δt_{CC-SC} distributions: the blue distribution is all negative particles after the electron identification cuts except $|\Delta t_{CC-SC}| < 2$ ns (red lines), while the black distribution is the same distribution without any cuts.

3.2.e – EC Fiducial Cuts

Particles hitting the edges of the EC

Electromagnetic showers for particles hitting the edges of the EC can be only partially detected. Without all the information about the shower, particles cannot be reconstructed correctly. Therefore, fiducial cuts removing particles registering a signal at the edges of the calorimeter is introduced. A conversion of coordinates is applied by relating the hit location of the particle in the CLAS coordinate system to the u, v and w system, where each axis correspond to the hit location with respect to the side of an EC sector. Figure 3.6 shows the applied cuts using the u, v and w coordinate system.

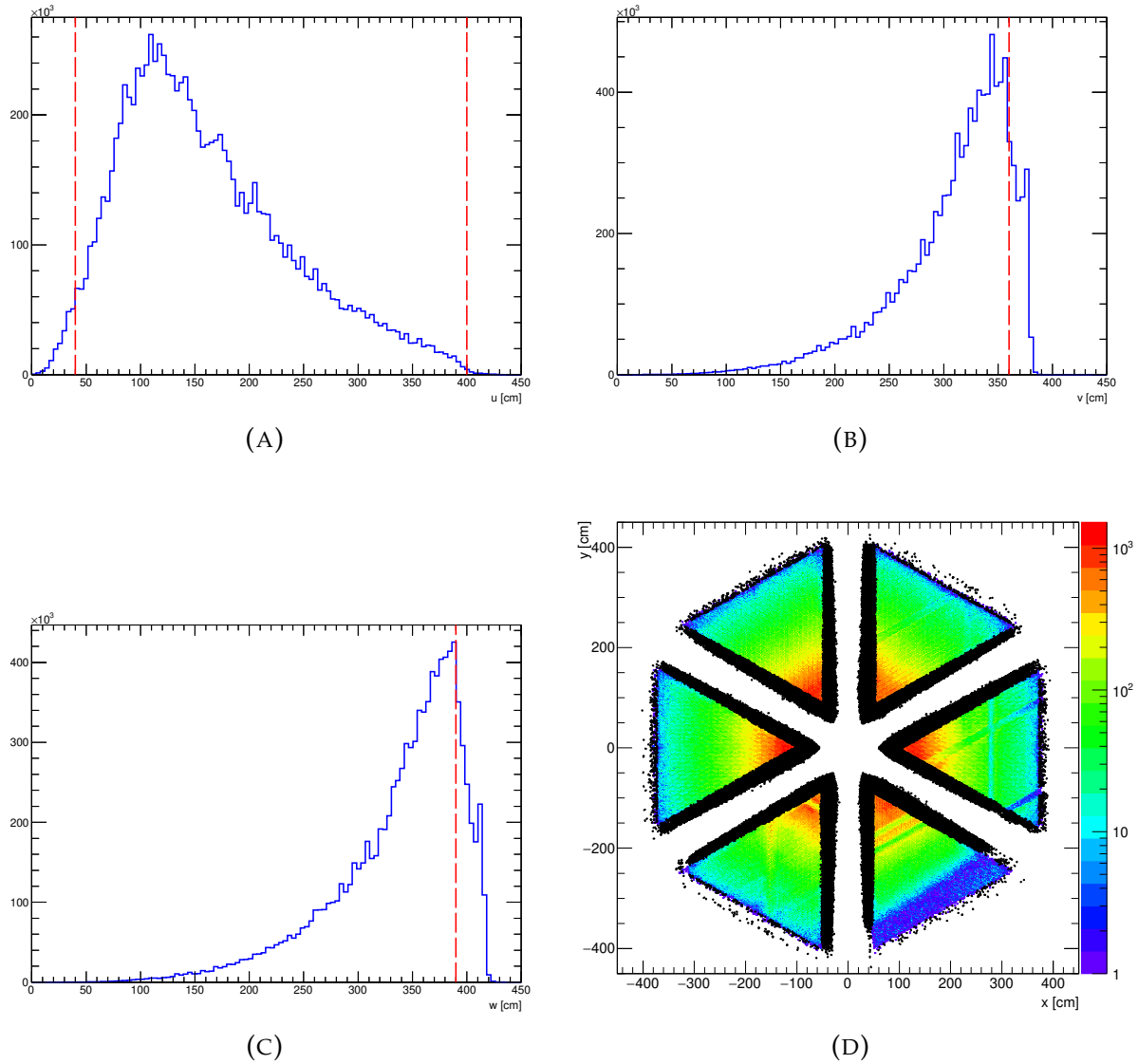

(A) (B)

(C) (D)

FIGURE 3.6 – Figures A, B, C are projections of EC particle hits onto the u, v and w coordinate system. Figure D is the xy distribution of hits in the EC, the colored events are negative particles passing the EC fiducial cuts and the black edges are events which did not pass.

Particles hitting the IC

The material of the IC blocks particles with low θ angles. Those particles will likely hit the IC or its frame and therefore lose energy before being detected by the EC. To remove particles which will be mis-reconstructed because of this interaction, a fiducial cut removes the events that would hit part of the IC [71] (see figure 3.7).

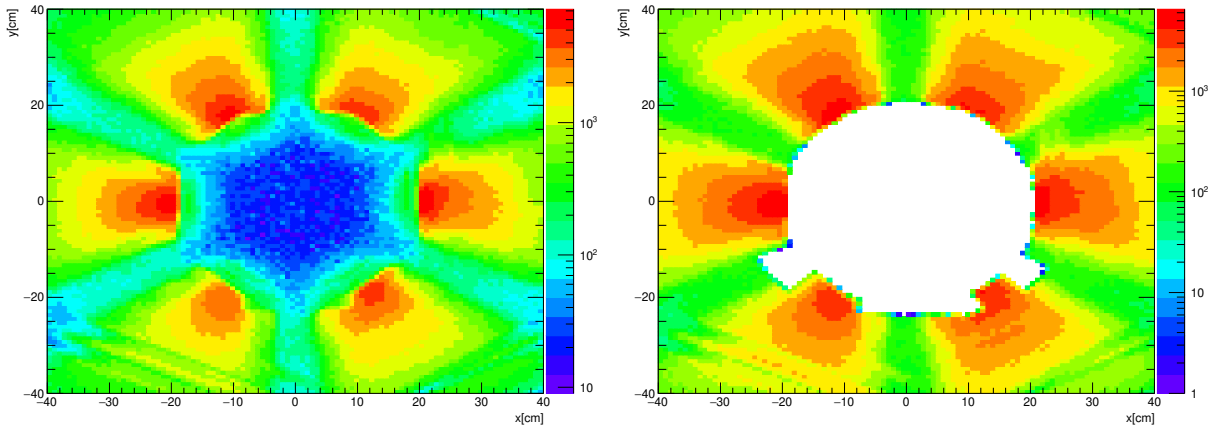

FIGURE 3.7 – xy distribution of negative particle hits at the first layer of the DC. The left plot is the distribution without the IC shadowing fiducial cut and the right plot has the cut applied.

3.3

Proton Identification

The identification of protons is performed on events where one and only one electron was identified. Protons must be distinguished from various mesons (π^+, K^+, ...) and heavier ions. Table 3.3 lists all the variables and cuts applied to identify protons.

Variable	Cut
Charge	q = 1
β	$\lvert\beta_{\text{calculated}} - \beta_{\text{measured}}\rvert \leqslant 0.05$
Vertex	$\lvert v_z - z_{\text{target}}\rvert \leqslant 4$ cm
IC shadowing fiducial cuts	

TABLE 3.3 – Summary of all proton identification cuts.

3.3.a – β cut

In order to separate protons from other positive particle we compare the β calculated from measured time and hit location at the SC (β_{SC}) to the β calculated using the momentum measured by the DC (β_{DC}). The variables are defined as:

$$\beta_{SC} = \frac{r_{SC}}{(t_{SC} - t_{\text{event}})\, c} \tag{3.2}$$

where r_{SC} and t_{SC} are the path length and time from the target to the SC respectively. t_{event} is the event start time obtained from the electron: $t_{\text{event}} = t_{SC,e^-} - \frac{r_{SC,e^-}}{c}$.

$$\beta_{DC} = \frac{p}{\sqrt{p^2 + M_p^2}} \tag{3.3}$$

where p is the momentum calculated from the curvature of the track measured in the DC.

We show in figure 3.8 β_{SC} as a function of the momentum p (measured by the DC). The black line is the β_{DC} calculated using only the momentum reconstructed (see Eq. 3.3), and the two red lines are the applied cuts, $|\beta_{SC} - \beta_{DC}| < 0.05$.

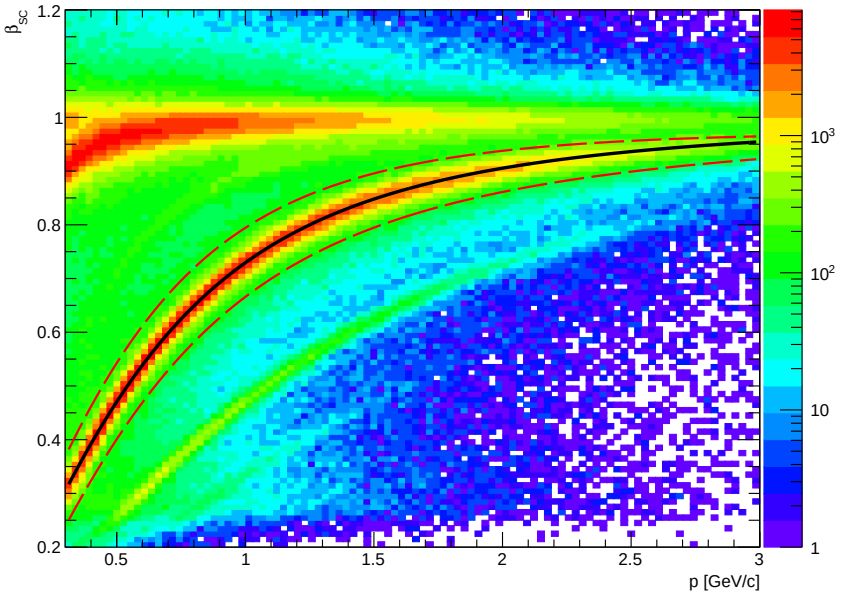

FIGURE 3.8 – β_{SC} as a function of the momentum p: the black line is β_{DC} and the events between the two red curves are events passing this cut.

3.3.b – Vertex Cut

In order to select protons originating from the target, a cut on the z-component of the reconstructed vertex is applied : $|v_z - z_{target}| \leqslant 4$ cm (see figure 3.9). The low energy of the protons impact the resolution and the precision at which the vertex is reconstructed. Therefore, the vertex cut applied to the protons is larger than the vertex cut applied for the electrons (see figure 3.4).

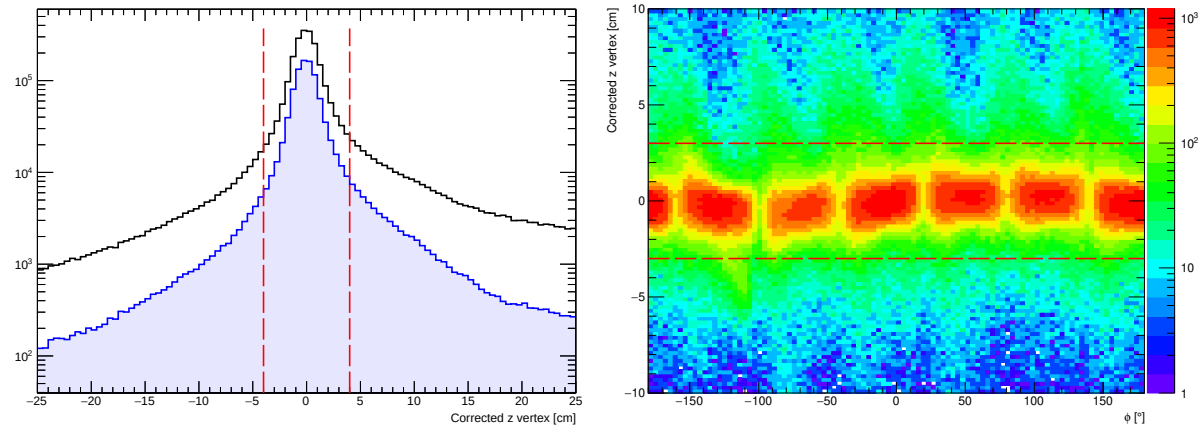

FIGURE 3.9 – Reconstructed z-vertex for positive particles (left) : the blue distribution is all positive particles after the proton identification cuts except the $|v_z - z_{target}| \leqslant 4$ cm (logarithmic scale) , and the black histogram is the same distribution without any cuts. On the right is a 2 dimensional histogram with the reconstructed vertex distribution (same as the blue histogram on the left) versus the angle ϕ.

3.3.c – IC Shadowing Fiducical Cuts

The same procedure as the electron identification is applied to remove proton candidates which could have hit the IC or its surrounding structure and be misreconstructed. The cuts is applied on the reconstructed position of the proton at the first layer of the DC (see figure 3.10).

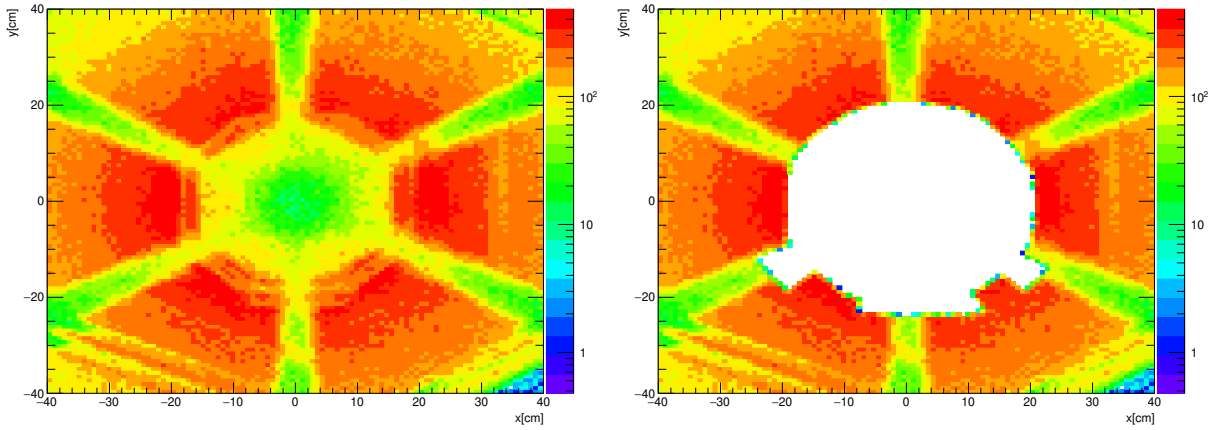

FIGURE 3.10 – xy distribution of positive particle hits at the first layer of the DC. The left plot is the distribution without the IC shadowing fiducial cut and the right plot has the cut applied.

3.4

Photon Identification

Photons can be detected by two different detectors, the EC and the IC. As a reminder, the EC will detect photons with large θ angles, while the IC will detect photons closer to the beam. The prerequisite for this step is the previous identification of only one electron and only one proton in the event. While several photons may be identified as a result of the photon identification cuts, a final cut will be applied in the next stage of the analysis to only keep the highest energy photon.

3.4.a – EC Photons

Here is an overview of the cuts applied in order to identify photon hitting the EC:

Variable	Cut
Charge	q = 0
Energy	$E_\gamma > 0.25$ GeV
β	$\beta > 0.92$
EC fiducial cuts	$40 < u < 400$ cm $0 < v < 360$ cm $0 < w < 390$ cm
IC shadowing fiducial cuts	

TABLE 3.4 – Summary of all photon identification cuts for the EC.

Energy cut

The energy of the photon can be calculated using the total deposited energy in the EC and the detector sampling fraction. Previous analyses of the eg1-dvcs data calculated the sampling fraction to be 0.2765 [68]. Therefore the total energy of a photon candidate is defined as:

$$E_\gamma = \frac{E_{EC,\text{total}}}{0.2765} \tag{3.4}$$

Low energy photons can be difficult to reconstruct by a sampling calorimeter such as the EC. Indeed, at low energy, lead layers can absorb most of the energy of the photon, making it difficult to get a reliable measurement from the scintillator layers. While the reconstruction and the skimming of the data already apply a cut on photon energy at $E_{EC,\text{total}} > 0.25$, some of the photon make it past this preliminary filter. Hence using the corrected EC energy (see eq. 3.4), a cut $E_\gamma > 0.25$ GeV is applied. Moreover, during the event selection, a much larger cut at 1 GeV will be applied when isolating DVCS events and will be discussed in the next chapter. Figure 3.11 is a distribution of the energies of the neutral particles detected by the EC.

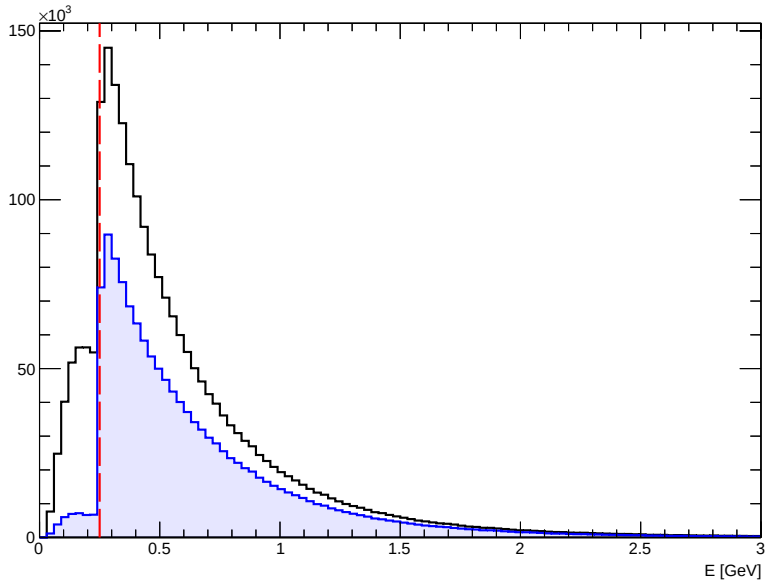

FIGURE 3.11 – Total energy E_γ distributions: the blue distribution is all neutral particles after the photon identification cuts except $E_\gamma > 0.25$ GeV (red lines), while the black distribution is the same distribution without any cuts.

β Cut

Photons and other neutral particles detected by the EC can be separated by their respective β. β for neutral particles can the calculated using the timing of the EC and

the distance between the target and the hit position of the particle in the EC (see figure 3.12). Using the event start time from the electron, $t_{\text{event}} = t_{SC,e^-} - \frac{r_{SC,e^-}}{c}$, particles with $\beta_{EC} > 0.92$ are kept and β_{EC} is defined as :

$$\beta_{EC} = \frac{r_{EC}}{(t_{EC} - t_{event})\, c} \tag{3.5}$$

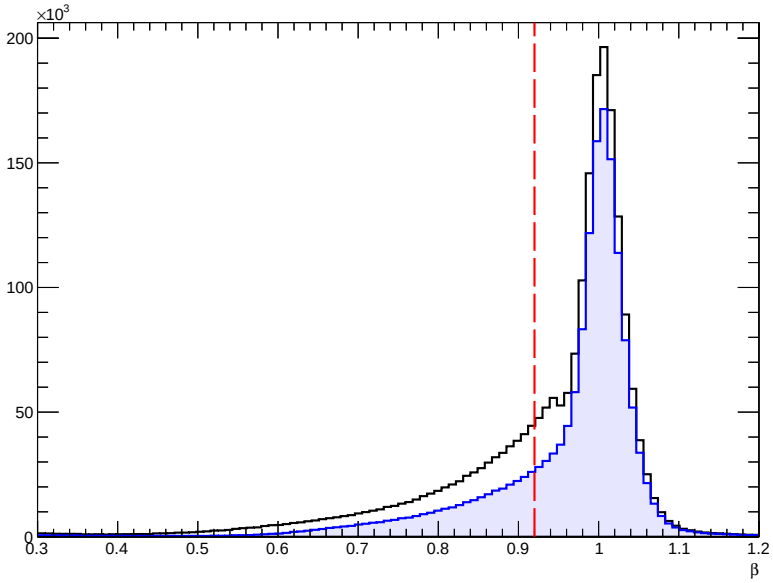

FIGURE 3.12 – β_{EC} distributions: the blue distribution is all neutral particles after the photon identification cuts except $\beta_{EC} > 0.92$ (red line), while the black line is the same distribution without any cuts.

EC Fiducial Cuts

To avoid reconstructing incorrectly photons hitting the edge of the EC, the same electron identification fiducial cuts is applied for the photons (see section 3.2.e). The result is showed in figure 3.13.

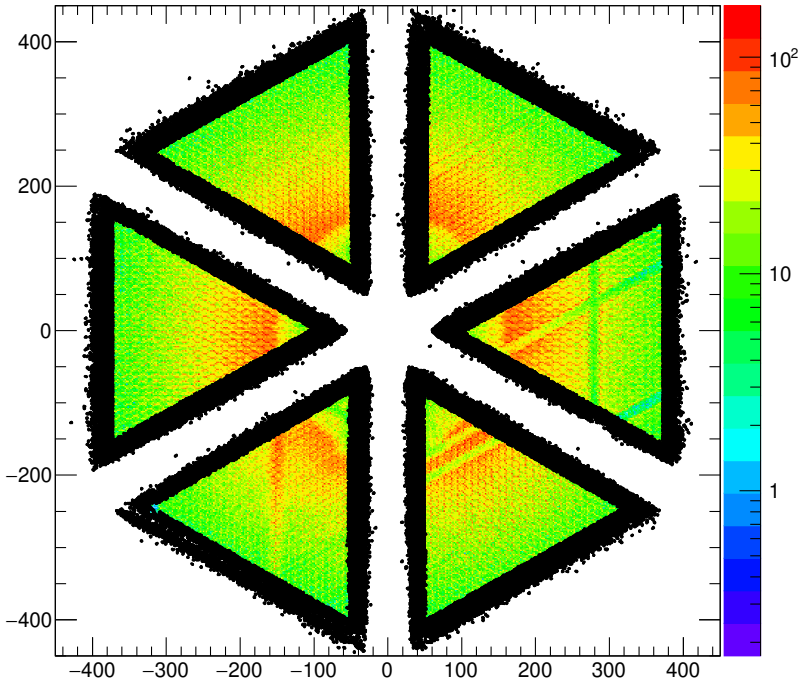

FIGURE 3.13 – xy distribution of hits in the EC, the colored events are neutral particles passing the EC fiducial cuts and the black edges are particles which did not pass.

IC shadowing fiducical cuts

Since the tracks of neutral particles are not measured by the DC, the position of the photons at the IC need to be calculated. The x and y coordinates of the photons at the IC is calculated using the following formulas:

$$x_{\mathrm{IC}} = x_{\mathrm{EC}} \cdot \frac{d_{\mathrm{IC}}}{d_{\mathrm{EC}}} \tag{3.6}$$

$$y_{\mathrm{IC}} = y_{\mathrm{EC}} \cdot \frac{d_{\mathrm{IC}}}{d_{\mathrm{EC}}} \tag{3.7}$$

where x_{EC} and y_{EC} are the hit locations of the photons in the EC, and d_{EC} and d_{IC} are the distance from the photons reconstructed vertex to the EC and IC respectively. The same fiducal cut used for the electrons and protons is applied to remove the particles that would hit the material of the IC (see figure 3.14).

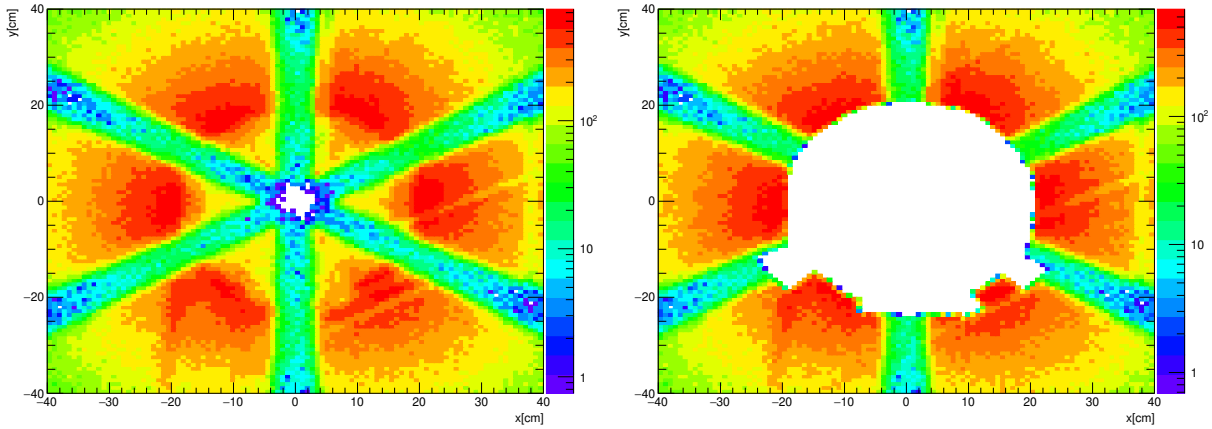

FIGURE 3.14 – xy position of neutral particle position at the first layer of the DC. The left plot is the distribution without the IC shadowing fiducial cut and the right plot has the cut applied.

3.4.b – IC Photons

The IC is a standalone detector and does not depend on the other CLAS detectors to identify photons. Compared to a sampling calorimeter, the lead-tungsten crystals of the IC absorb all the energy of the electromagnetic shower, requiring little to no corrections to measure the energy of photon candidate.

The list of cuts for the photon identification in the IC is as follow:

Variable	Cut
Energy	Part A $E_\gamma > 0.35$ GeV + Møller cut
	Part B $E_\gamma > 0.30$ GeV + Møller cut
IC fiducial cuts	

TABLE 3.5 – Summary of all photon identification cuts for the IC.

Energy cuts

Because of this proximity with the beam, the Møller electrons are the main background of the IC (especially at small angle θ). To reduce this background a set of cuts on the energy was chosen and is composed of two components : a fixed energy cut applies for the whole detector as well as an energy cut as a function of θ (see figure 3.15). Since Part A and B used two different target locations, the set of cuts are slightly different:

- Part A:

$$E > 0.35\,\text{GeV}$$
$$\theta > -\frac{6.5}{1.2}E + 7.5$$

- Part B:

$$E > 0.30\,\text{GeV}$$
$$\theta > -\frac{6.5}{1.6}E + 6.5$$

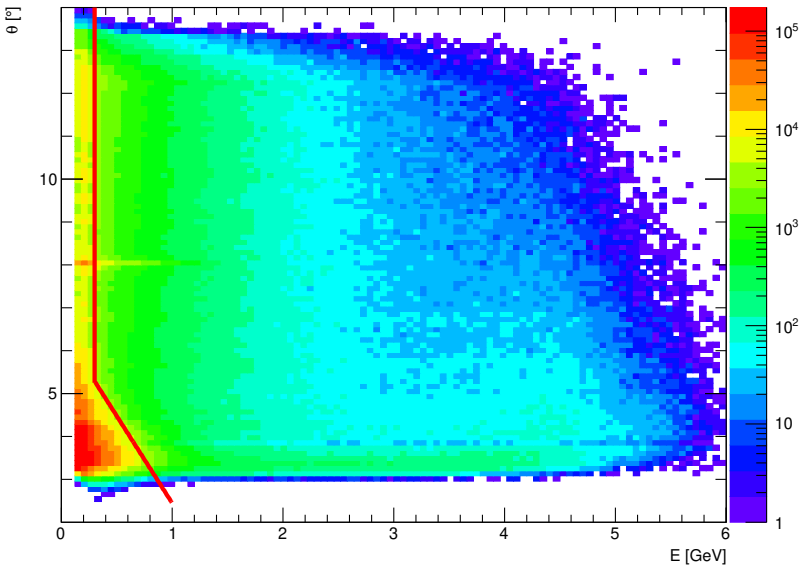

FIGURE 3.15 – 2 dimensional histogram showing the correlation between the angle θ and the energy measured for part B events. The red line is the energy cuts used to remove low energy photons and Møller background.

IC fiducial cuts

Photons hitting the edge of the IC cannot be reconstructed appropriately as they only deposit a portion of their energy inside the crystals. Those photons are removed using a fiducial cut applied on the inner and the outer edge of the IC. Figure 3.16 illustrates this cut.

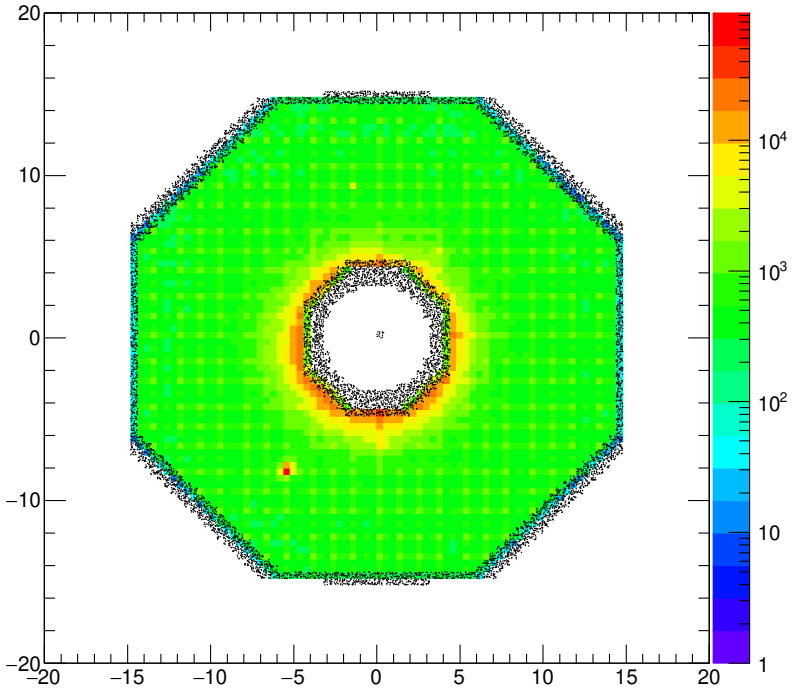

FIGURE 3.16 – xy distribution of hits in the IC, the colored events are photons passing the IC fiducial cuts and the black edges are particles which did not pass.

CHAPTER 4

Event Selection

The previous chapter described the identification and the preselection of particles to match DVCS requirements. However, further cuts must be applied to select incoherent DVCS events and ensure the exclusivity of the reaction. This chapter will detail the procedure used to select incoherent DVCS events on nitrogen from the eg1-dvcs NH_3 data, while rejecting DVCS on proton events.

First, a momentum correction is applied to correct for the energy lost by the electrons and protons when passing through the detectors. Then, the events are sorted by a preliminary set of cuts which guarantees that the events kinematic is consistent with DVCS and removes background events such as hadronic resonances.

The exclusivity distributions of DVCS events on nucleus will be wider as a consequence of effects such as Fermi motion and Final State Interactions (FSI). This characteristic allows for the selection of nitrogen DVCS events by subtracting the hydrogen events from the data, which have narrower exclusivity distributions. The hydrogen events are identified using the same procedure as the original proton DVCS analysis [68]. We used the carbon data as a way to determine a preliminary set of exclusivity cuts to apply to the nitrogen. The hydrogen events are then subtracted and new exclusivity cuts are calculated to isolated incoherent DVCS nitrogen events.

4.1

Preliminary Corrections and Cuts

4.1.a – Momentum Corrections

The momentum of charged particles is calculated using the trajectories measured by the DC inside the magnetic field. Charged particles, electrons and protons, will lose energy when passing various detector materials, which is not accounted for in the

reconstruction of a particle's momentum. Particles with low energy are particularly affected by this effect. A momentum correction is applied by comparing simulated data and reconstructed momentum. Reference [68] explains the process in more details and defines the following equation to correct the momentum of electrons and protons (the parameters of the equation are listed in table 4.1):

$$p_{\text{corr}} = p \cdot \left(a + \frac{b}{p} - \frac{c}{p^2} + \frac{d}{p^3} \right) \tag{4.1}$$

	Electrons		Protons	
	Part A	Part B	Part A	Part B
a	0.999452	0.9997360	0.997204	0.992767
b	0.00615979	0.0105136	0.00562253	0.0147232
c	0.00304068	0.00515416	0.00348868	0.0084665
d	0	0	0.00229922	0.0032769

TABLE 4.1 – Momentum correction parameters for the electrons and protons.

4.1.b – Kinematic Cuts

Events with only one electron, one proton and one photon are kept for the rest of the analysis. If more than one photon is detected for a given event, the most energetic photon is selected. After this selection of events, matching a DVCS final state, a series of preliminary cuts ensure that the reconstructed particles match the kinematic requirement of DVCS events:

- $Q^2 > 1$ GeV^2/c^2 and $Q^2 < -t$ guarantee that the event is within the Bjorken scaling regime and that the DVCS handbag formalism applies;
- $W^2 > 4$ GeV^2 removes events from the resonance region;
- $E_\gamma > 1$ GeV acts as a preliminary cut to select DVCS events, which are expected to have high energy photons.

4.2

Exclusivity Variables

DVCS events are selected by cutting on a set of exclusivity variables. Since all the final particles are measured, the conservation of momentum and energy must be respected. Therefore each variable has an expected value which will be used as a starting point to determine the cuts ensuring the exclusivity of the reaction. This section will define the variables used and will list their expected values.

Measured four momentum vectors

As a reminder, the incoherent DVCS reaction is:

$$\mathrm{e}(P_e) + \mathrm{p}(P_p) \rightarrow \mathrm{e}'(P_{e'}) + \mathrm{p}'(P_{p'}) + \gamma(P_\gamma) \tag{4.2}$$

The previous four momentum vectors are calculated using the information from the accelerator or measured by the detectors as follows:

$$\begin{aligned}
P_e &= (0, 0, E_{\text{beam}}, E_{\text{beam}}) \\
P_p &= (0, 0, 0, M_p) \\
P_{e'} &= \left([c_{x,e} \cdot p_e],\ [c_{y,e} \cdot p_e],\ [c_{z,e} \cdot p_e],\ p_e\right) \\
P_{p'} &= \left([c_{x,p} \cdot p_p],\ [c_{y,p} \cdot p_p],\ [c_{z,p} \cdot p_p],\ \sqrt{p_p^2 + M_p^2}\right) \\
P_{\gamma,\text{EC}} &= \left([c_{x,\gamma} \cdot E_\gamma],\ [c_{y,\gamma} \cdot E_\gamma],\ [c_{z,\gamma} \cdot E_\gamma],\ E_\gamma\right) \\
P_{\gamma,\text{IC}} &= \left([\hat{r}_{x,\gamma} \cdot E_\gamma],\ [\hat{r}_{y,\gamma} \cdot E_\gamma],\ [\hat{r}_{z,\gamma} \cdot E_\gamma],\ E_\gamma\right)
\end{aligned} \tag{4.3}$$

where E_{beam} is the beam energy, M_p is the mass of the proton, $c_{x,y,z}$ is the cosine of the particle's direction, and p is the particle's momentum. If the photon is detected by the EC, the four momentum vector is calculated using the previously introduced variables. However in the case where the photon is detected by the IC, a unit vector $\hat{r}$ is calculated using the hit position on the IC.

Missing Masses

The missing mass squared variables are defined as:

$$\begin{aligned} MM_X^2(ep) &= \left(P_X^{ep}\right)^2 \\ MM_X^2(e\gamma) &= \left(P_X^{e\gamma}\right)^2 \\ MM_X^2(ep\gamma) &= \left(P_X^{ep\gamma}\right)^2 \end{aligned} \tag{4.4}$$

using the following vectors:

$$\begin{aligned} P_{\gamma^*} &= P_e - Pe' \\ P_X^{ep} &= P_e + P_p - \left(P_{e'} + P_{p'}\right) \\ P_X^{e\gamma} &= P_e + P_p - \left(P_{e'} + P_\gamma\right) \\ P_X^{ep\gamma} &= P_e + P_p - \left(P_{e'} + P_{p'} + P_\gamma\right) \end{aligned} \tag{4.5}$$

Since the DVCS channel is exclusive and must respect conservation laws, the values of the missing masses squared are predicted: $MM_X^2(ep) = 0\ \text{Gev}^2/\text{c}^4$ returns the mass squared of the photon, $MM_X^2(e\gamma) = 0.880\ \text{Gev}^2/\text{c}^4$ returns the mass squared of the proton, and $MM_X^2(ep\gamma) = 0\ \text{Gev}^2/\text{c}^4$ since this is the full system and no other particle should be present.

Coplanarity

If the event is from a DVCS reaction, the proton, photon and virtual photon must be in the same plane. The coplanarity $\Delta\phi$ is defined as the angle between the planes formed by the $\left(\vec{P}_p, \vec{P}_\gamma\right)$ and $\left(\vec{P}_p, \vec{P_{\gamma^*}}\right)$, which must be zero for DVCS events. It is calculated using the following formula:

$$\Delta\phi = \text{atan2}\left\{ \frac{\|\vec{P}_p\|\, \vec{P_{\gamma^*}} \cdot \left(\vec{P}_p \times \vec{P}_\gamma\right)}{\left(\vec{P_{\gamma^*}} \times \vec{P}_p\right) \cdot \left(\vec{P}_p \times \vec{P}_\gamma\right)} \right\} \tag{4.6}$$

Cone angle

The cone angle $\theta_{\gamma,epX}$ is the angle between the reconstructed photon, calculated using the measured electron and proton, and the detected photon. Again, for a DVCS event, the $\theta_{\gamma,epX}$ must be zero:

$$\theta_{\gamma,epX} = \cos^{-1}\left(\frac{\vec{P_X^{ep}} \cdot \vec{P}_\gamma}{\|\vec{P_X^{ep}}\| \cdot \|\vec{P}_\gamma\|} \right) \tag{4.7}$$

The selection of DVCS events is made by choosing a set cut on the exclusivity variables defined in this section. Applying cuts on several variables, and around their

respective expected values, guarantees the exclusivity of the DVCS reaction. It is noteworthy to mention that some expected values are shifted due to detectors resolutions and calibrations. The shifts experienced by some variables are estimated using the published results of the proton eg1-dvcs analysis as well as the eg6 ^{4}He DVCS analysis [44].

4.3

Hydrogen Exclusivity Cuts

In order to isolate nitrogen events from the NH_3 data, the hydrogen events must be identified and subtracted. This section will be a summary of the steps taken to identify the hydrogen events, more details are found in the dedicated analysis note [68]. Since the resolution and calibration accuracy are different between the EC and IC, the events will be separated depending on which detector measure the photon. Moreover, the eg1-dvcs run was divided in two parts (A and B), therefore a total of four different sets of cuts was selected and applied.

A narrow peak, centered at zero, is found in the NH_3 $MM_X^2(e\gamma)$ distribution corresponding to the hydrogen DVCS events (see figure 4.1). This variable was the starting point of the hydrogen analysis exclusivity cuts search. After an estimation and subtraction of the nitrogen background using the carbon data, events within the 3σ of the Gaussian fit on $MM_X^2(ep)$ peak were kept. A similar fitting procedure was applied on three other exclusivity variables: $\theta_{\gamma,epX}$, $\Delta\phi$ and $p_{\perp,X}(ep\gamma X)$. Table 4.2 lists all the cuts calculated and applied to identify the hydrogen events by the original proton DVCS analysis [68].

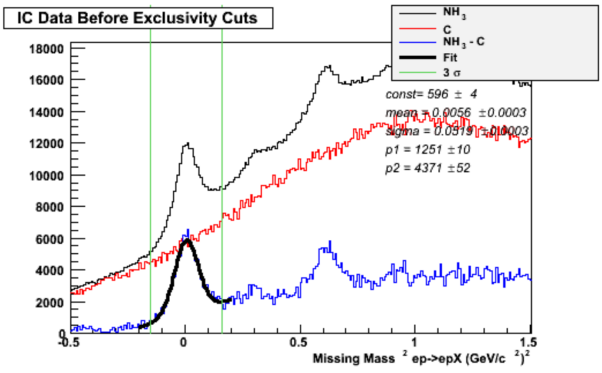

FIGURE 4.1 – $MM_X^2(e\gamma)$ IC events, without any exclusivity cuts. The black curve is the NH_3 data, the red curve is the carbon data and the blue curve is the NH_3 data after the carbon subtraction. The peak, centered at zero, is fitted using a Gaussian and the green vertical lines represent the $\pm 3\sigma$ window.

Variable	IC		EC	
	Part A	Part B	Part A	Part B
MM^2 (ep) [Gev^2/c^4]	[-0.167, 0.181]	[-0.150, 0.161]	[-0.105, 0.164]	[-0.114, 0.167]
$\theta(\gamma, epX)$ [°]	< 1.055	< 0.976	< 2.52	< 2.38
$\Delta\phi$ [°]	[-1.773, 1.647]	[-1.495, 1.289]	[-1.686, 1.782]	[-1.875, 1.979]
$p_{\perp,X}(ep\gamma X)[GeV]$	< 0.096	< 0.095	< 0.284	< 0.279

TABLE 4.2 – Hydrogen cuts used by the original DVCS analysis for the IC and EC topologies and differentiated by part A and B of the experiment [68].

As a cross check, a comparison between the four exclusivity variable distributions obtained by the previous hydrogen analysis and the distribution obtained by this analysis are exhibited in figures 4.2, 4.3, 4.4 and 4.5. The results of this work are in agreement with the original proton analysis.

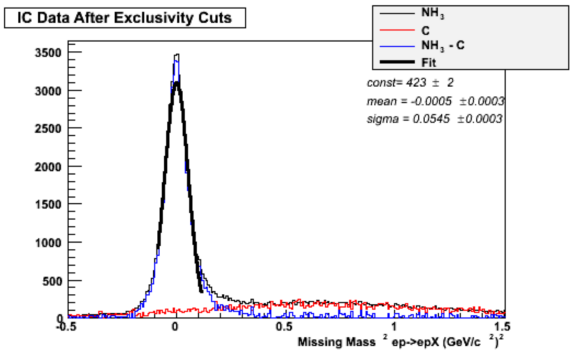

(A) IC: original proton analysis

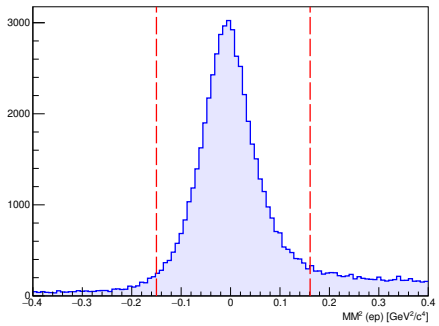

(B) IC: nitrogen analysis (this work)

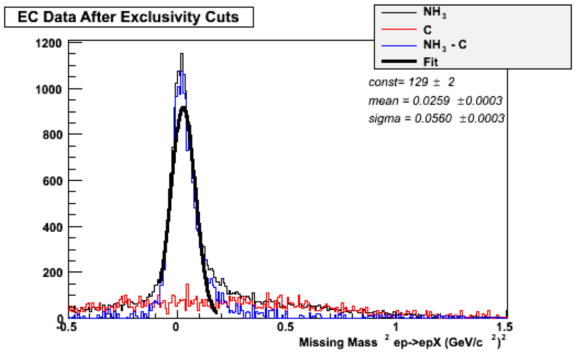

(C) EC: original proton analysis

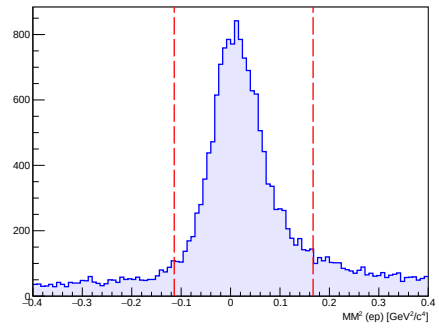

(D) EC: nitrogen analysis (this work)

FIGURE 4.2 – Comparison of the $MM^2(ep)$ distributions after applying the exclusivity cuts to identify the hydrogen events, except the $MM^2(ep)$ cut. On the left is the original proton analysis results [68]. The black line is the NH_3 distribution, the red line is the carbon distribution, the blue line is the NH_3 data with the carbon subtraction and the thicker black line is the result of the Gaussian fit. On the right is the result obtained by this work with the vertical red lines being the $MM^2(ep)$ exclusivity cut for reference.

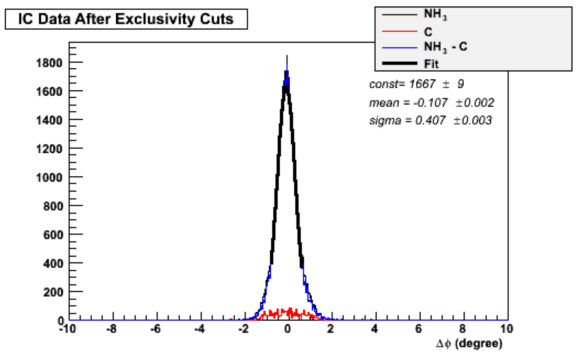

(A) IC: original proton analysis

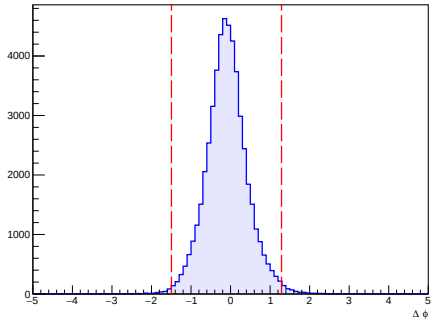

(B) IC: nitrogen analysis (this work)

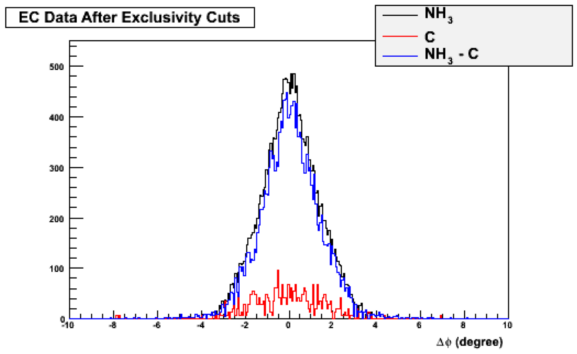

(C) EC: original proton analysis

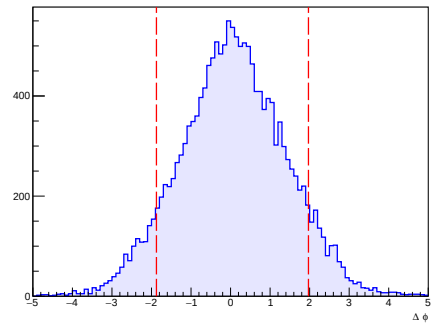

(D) EC: nitrogen analysis (this work)

FIGURE 4.3 – Comparison of the $\Delta\phi$ distributions after applying the exclusivity cuts to identify the hydrogen events, except the $\Delta\phi$ cut. On the left is the original proton analysis results [68]. The black line is the NH_3 distribution, the red line is the carbon distribution, the blue line is the NH_3 data with the carbon subtraction and the thicker black line is the result of the Gaussian fit. On the right is the result obtained by this work with the vertical red lines being the $\Delta\phi$ exclusivity cut for reference.

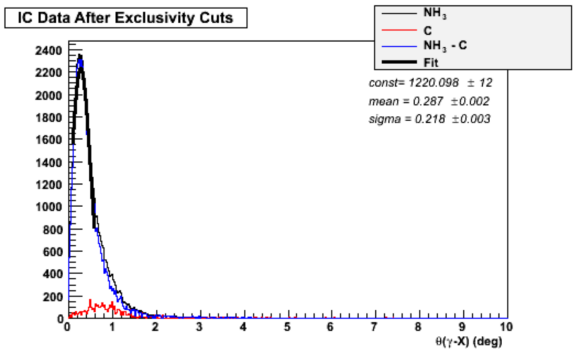

(A) IC: original proton analysis

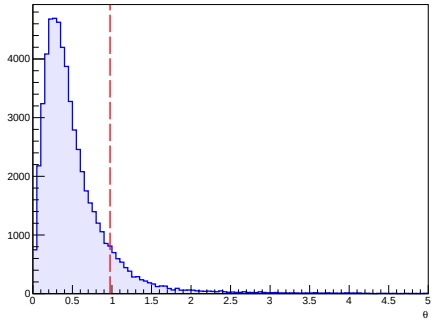

(B) IC: nitrogen analysis (this work)

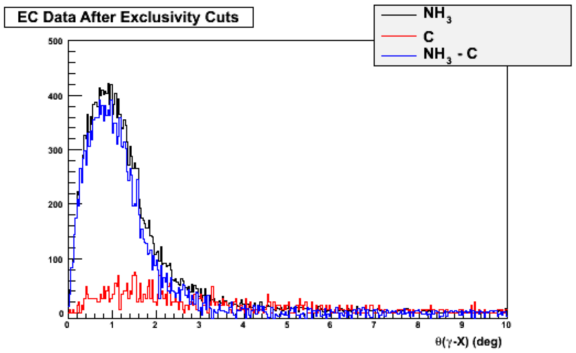

(C) EC: original proton analysis

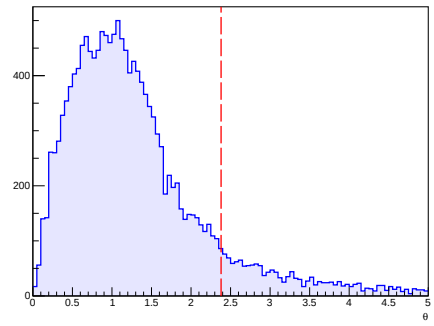

(D) EC: nitrogen analysis (this work)

FIGURE 4.4 – Comparison of the $\theta_{\gamma,epX}$ distributions after applying the exclusivity cuts to identify the hydrogen events, except the $\theta_{\gamma,epX}$ cut. On the left is the original proton analysis results [68]. The black line is the NH_3 distribution, the red line is the carbon distribution, the blue line is the NH_3 data with the carbon subtraction and the thicker black line is the result of the Gaussian fit. On the right is the result obtained by this work with the vertical red lines being the $\theta_{\gamma,epX}$ exclusivity cut for reference.

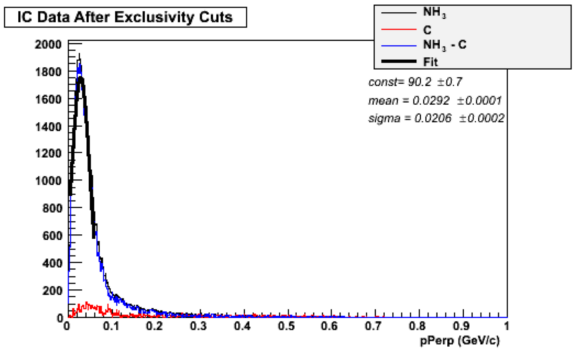

(A) IC: original proton analysis

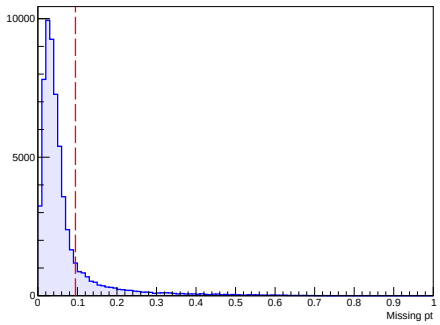

(B) IC: nitrogen analysis (this work)

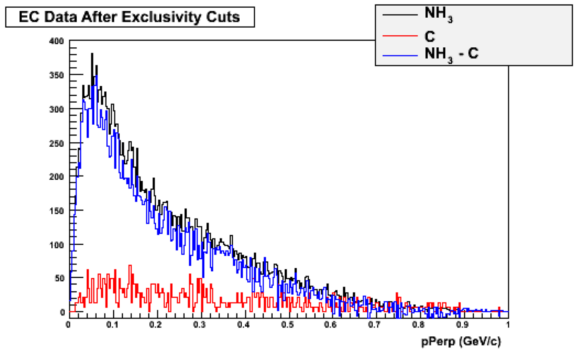

(C) EC: original proton analysis

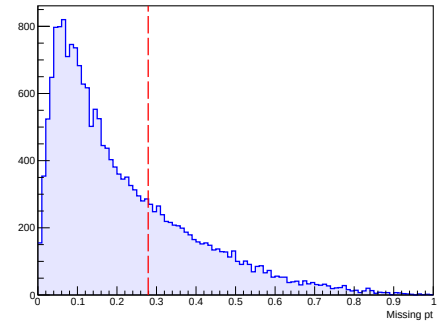

(D) EC: nitrogen analysis (this work)

FIGURE 4.5 – Comparison of the $p_{\perp,X}(ep\gamma X)$ distributions after applying the exclusivity cuts to identify the hydrogen events, except the $p_{\perp,X}(ep\gamma X)$ cut. On the left is the original proton analysis results [68]. The black line is the NH_3 distribution, the red line is the carbon distribution, the blue line is the NH_3 data with the carbon subtraction and the thicker black line is the result of the Gaussian fit. On the right is the result obtained by this work with the vertical red lines being the $p_{\perp,X}(ep\gamma X)$ exclusivity cut for reference.

The hydrogen analysis used only four exclusivity cuts, however for the nitrogen event selection we will add cuts on the missing masses squared $MM^2_X(ep\gamma)$ and $MM^2_X(e\gamma)$, and the missing energy. This approach further ensures the exclusivity of the events and will be discussed below.

For reference, we show, in figures 4.6 and 4.7, the $MM^2_X(ep\gamma)$, $MM^2_X(e\gamma)$ and the missing energy distributions, which were not shown in the proton analysis note [68]. Although, the $MM^2_X(ep\gamma)$ is centered on its expected value (0), the $MM^2_X(e\gamma)$ and missing energy were shifted from their theoretical values by around 0.2 GeV^2/c^4 and 0.2 GeV respectively. This offset is the result of detector calibration issues or alignment.

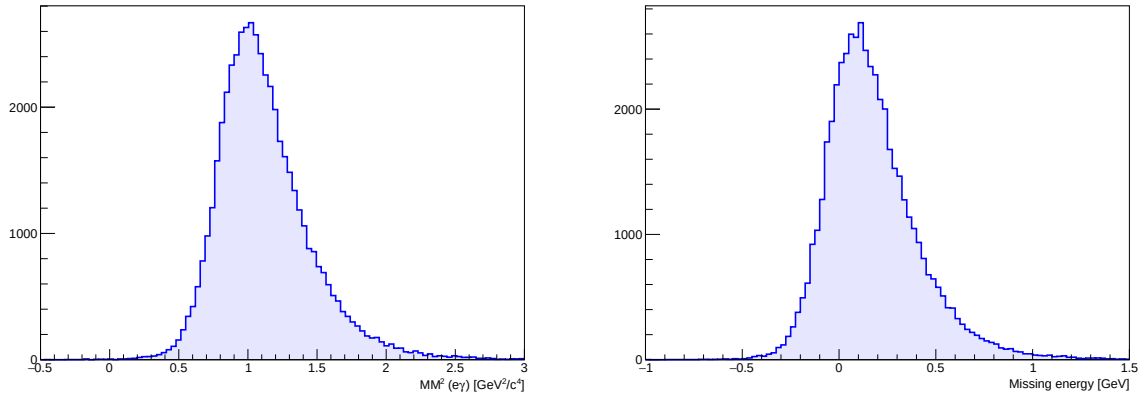

FIGURE 4.6 – Left: IC $MM^2_X(e\gamma)$ distribution after all hydrogen exclusivity cuts. Right: IC Missing energy distribution after all hydrogen exclusivity cuts.

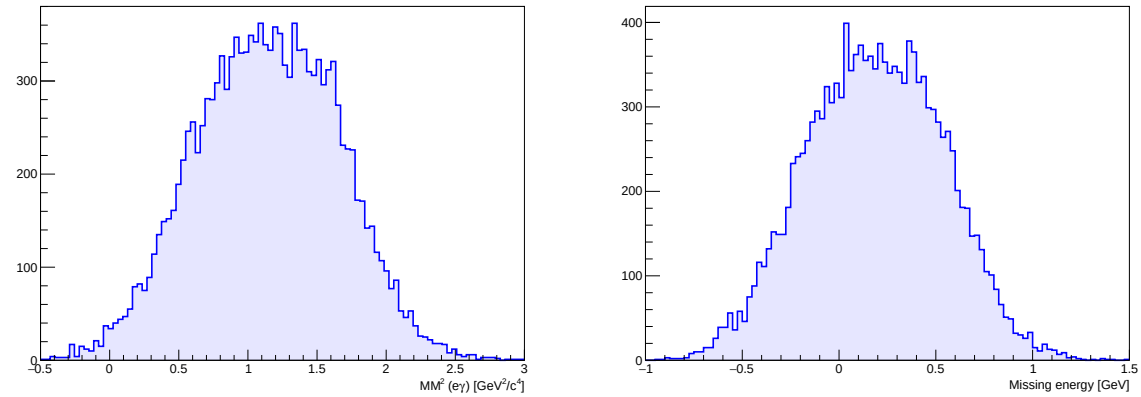

FIGURE 4.7 – Left: EC $MM^2_X(e\gamma)$ distribution after all hydrogen exclusivity cuts. Right: EC Missing energy distribution after all hydrogen exclusivity cuts.

4.4

Carbon Exclusivity Cuts

Before subtracting the hydrogen events from the NH_3 data, a study to determine the exclusivity cuts on the carbon data was made. While only representing 10% of the data taken, the carbon data offers two advantages: there are no protons in the sample and carbon is a nucleus of similar size to nitrogen. Therefore, the carbon exclusivity cuts can later be applied to the nitrogen.

As discussed previously on the selection of hydrogen events, some of the exclusivity variable distributions are shifted from their expected values. By narrowly cutting on $\Delta\phi$, $\theta_{\gamma,epX}$, $MM^2_X(ep\gamma)$ and $p_{\perp,X}(ep\gamma X)$, which will guarantee a near clean sample of DVCS events, the center of the other exclusivity variable distributions is studied. Figures 4.8 and 4.9 shows the exclusivity variables when narrow cuts are applied to the carbon data.

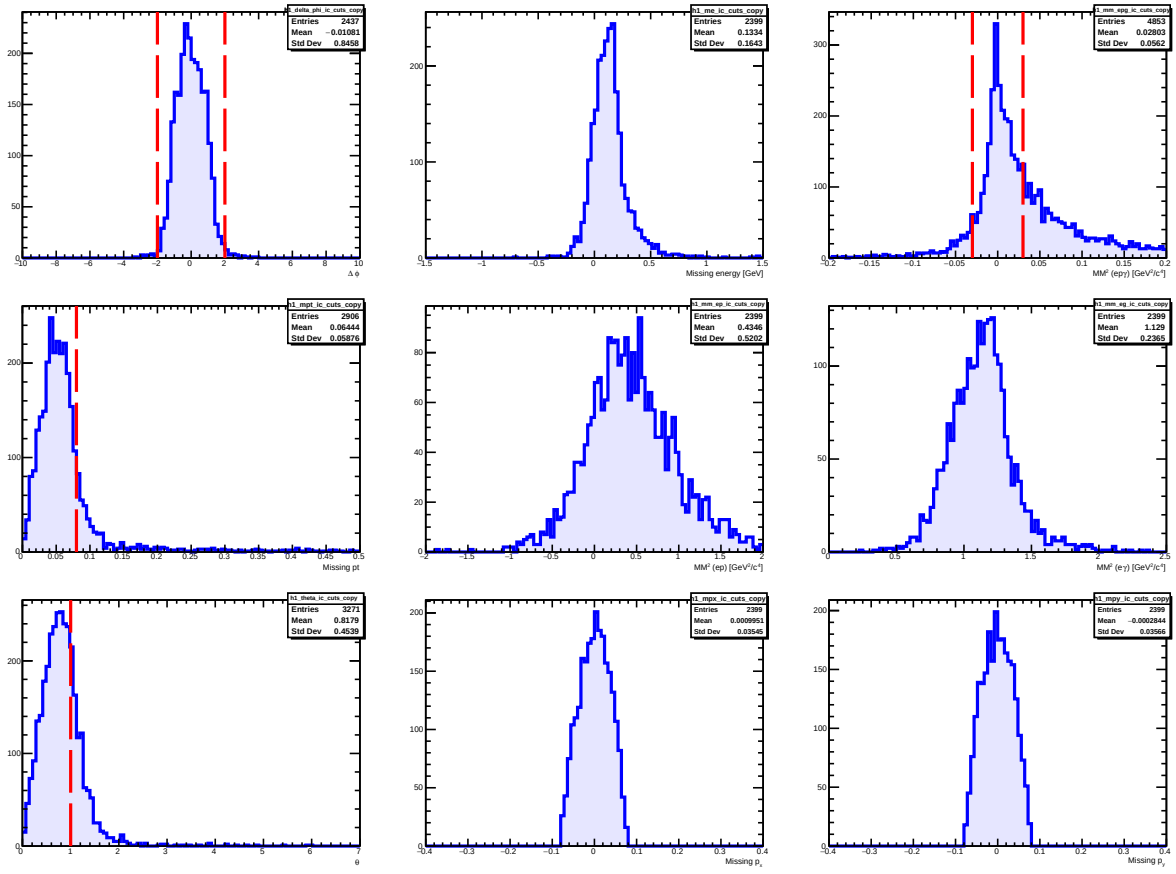

FIGURE 4.8 – Part B - IC carbon DVCS event distributions of the coplanarity $\Delta\phi$, cone angle $\theta_{\gamma,epX}$, missing masses squared, missing energy and momentum (p_x and p_y) and missing transverse momentum $p_{\perp,X}(ep\gamma X)$. The vertical line are the narrow cuts applied to study the center of the exclusivity variable distributions.

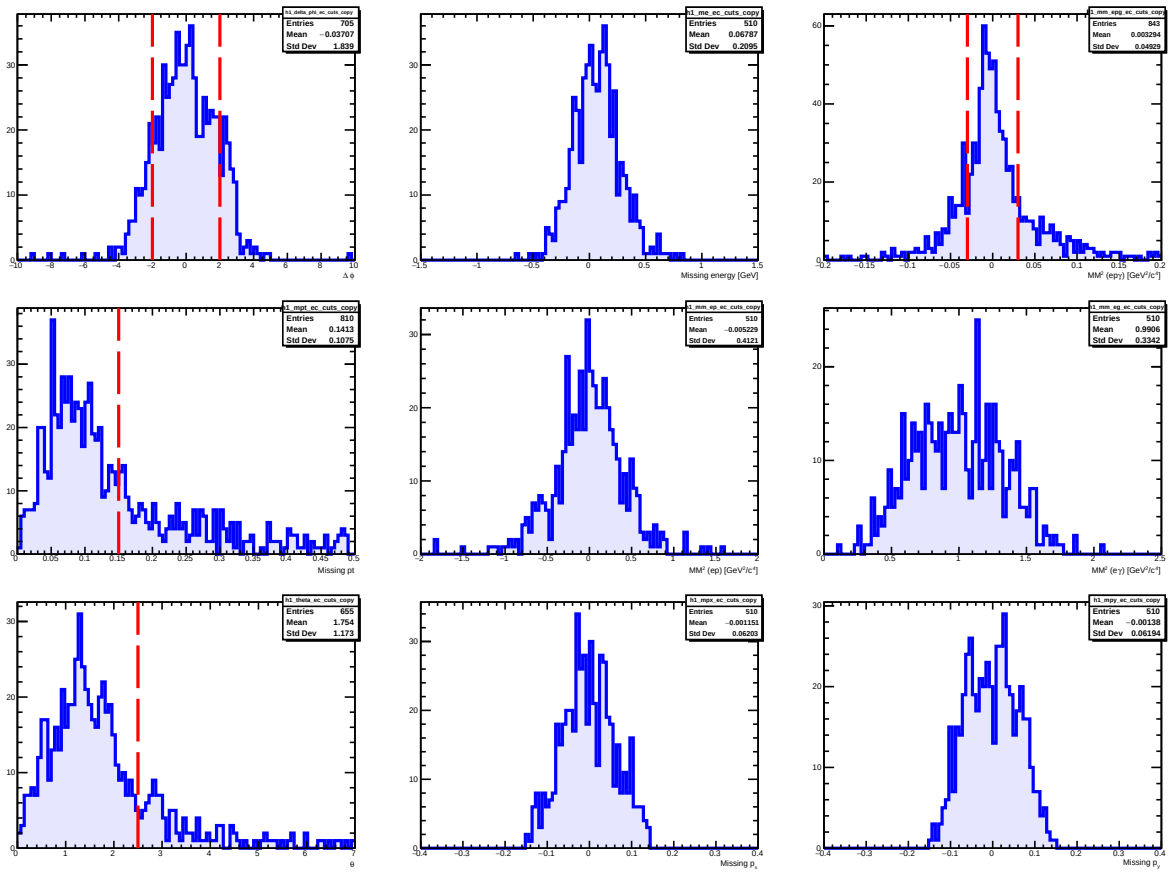

FIGURE 4.9 – Part B - EC carbon DVCS event distributions of the coplanarity $\Delta\phi$, cone angle $\theta_{\gamma,epX}$, missing masses squared, missing energy and momentum (p_x and p_y) and missing transverse momentum $p_{\perp,X}(ep\gamma X)$. The vertical line are the narrow cuts applied to study the center of the exclusivity variable distributions.

The offsets found in the hydrogen DVCS event selection in $MM_X^2(e\gamma)$ and the missing energy are also observed in the carbon sample, as well as a shift of 0.4-0.5 GeV^2/c^4 in $MM_X^2(ep)$ for the IC topology. An offset of about 0.2 GeV^2/c^4 is also present in the eg6 ^{4}He DVCS analysis [44]. The difference of shift values between the eg1-dvcs carbon and eg6 ^{4}He data could be linked to the different calibrations and corrections applied between the two experiments.

Sets of cuts are chosen using the measured shifted centers and widths similar to the cuts of the eg6 ^{4}He analysis and after several iterations, the final set of exclusivity cuts is calculated using 2 standard deviations below and above the mean value of the distributions. Figure 4.10 and 4.11 show the exclusivity variables after this new set of cut is calculated for the IC and EC topology respectively.

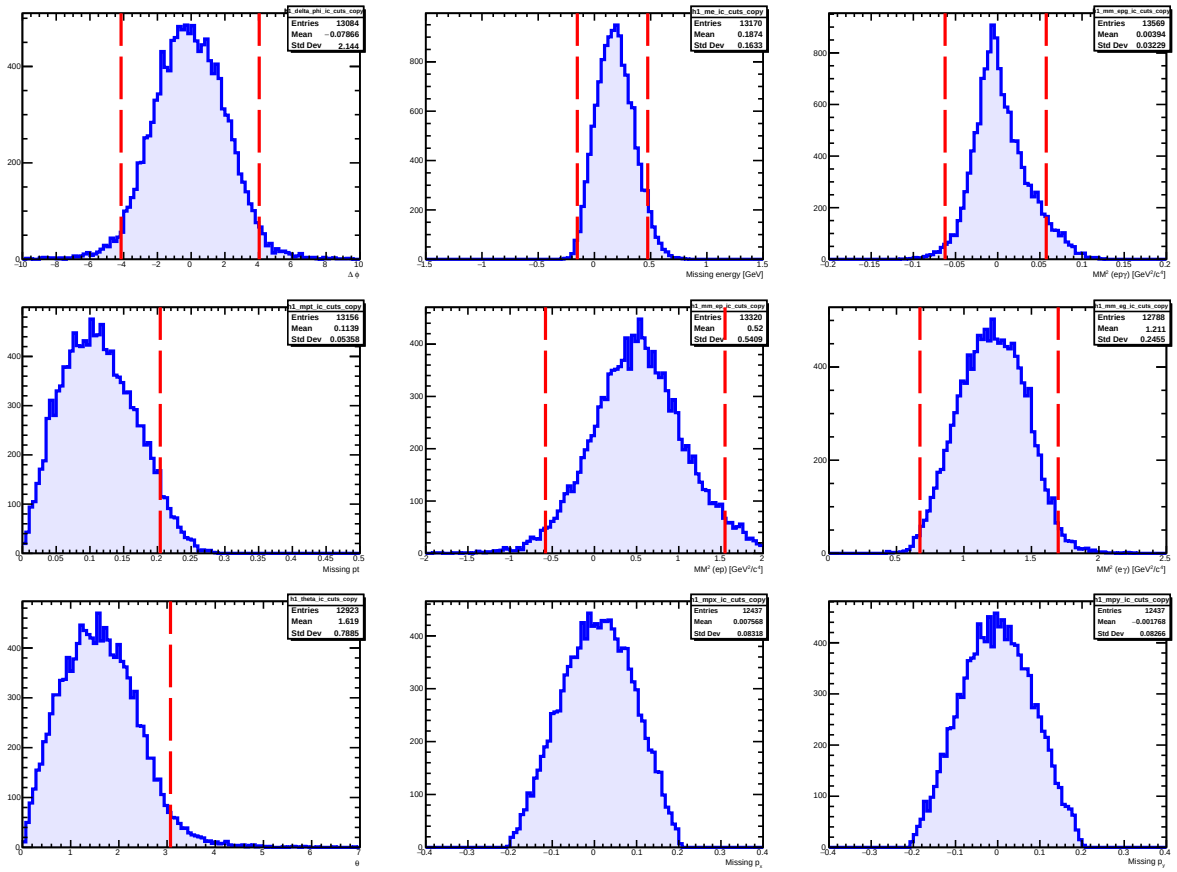

FIGURE 4.10 – Part B - IC carbon DVCS event distributions of the coplanarity $\Delta\phi$, cone angle $\theta_{\gamma,epX}$, missing masses squared, missing energy and momentum (p_x and p_y) and missing transverse momentum $p_{\perp,X}(ep\gamma X)$. Each distribution show the events passing the exclusivity cuts except the one of the variable being drawn (cuts are the vertical red lines).

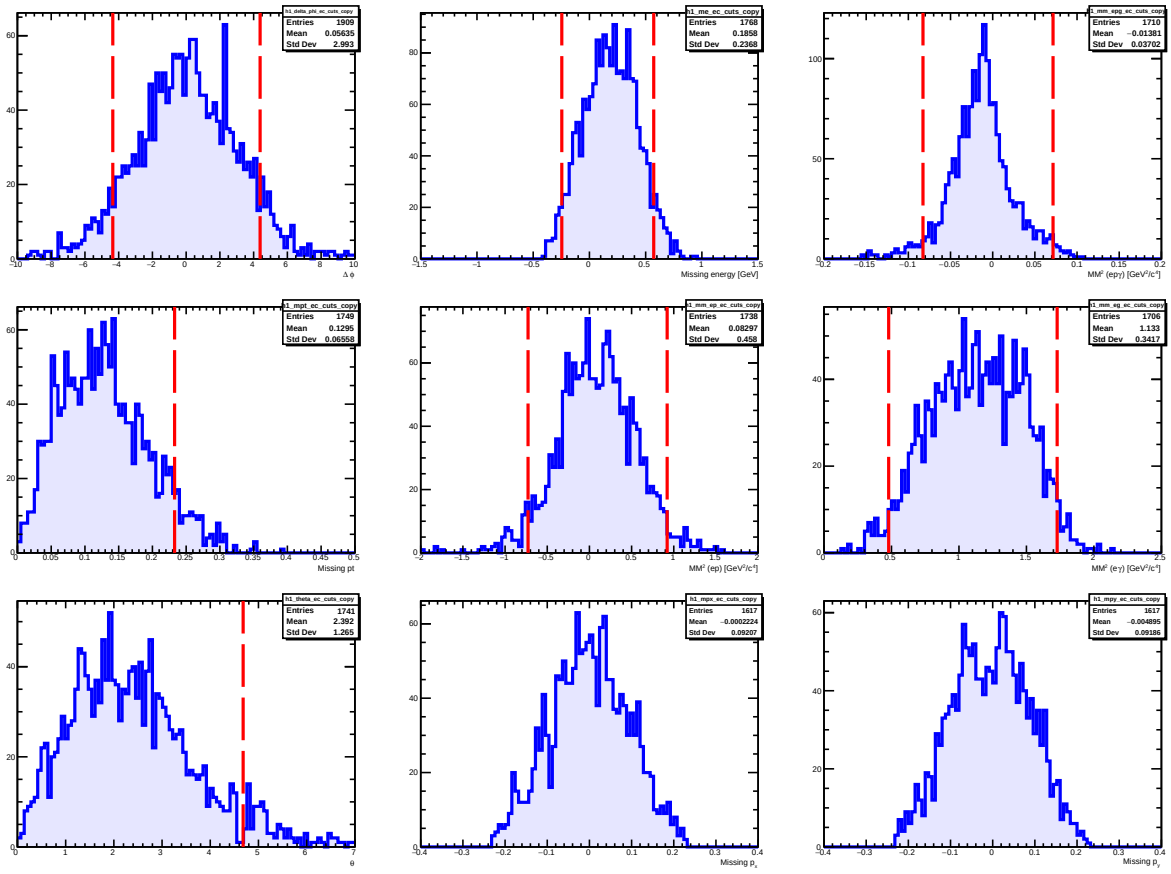

FIGURE 4.11 – Part B - EC carbon DVCS event distributions of the coplanarity $\Delta\phi$, cone angle $\theta_{\gamma,epX}$, missing masses squared, missing energy and momentum (p_x and p_y) and missing transverse momentum $p_{\perp,X}(ep\gamma X)$. Each distribution show the events passing the exclusivity cuts except the one of the variable being drawn (cuts are the vertical red lines).

4.5

Nitrogen Exclusivity Cuts

4.5.a – Hydrogen Events Subtraction

In order to select nitrogen DVCS events, the hydrogen events must be removed from the NH_3 data. This process will be done using the previously introduced set of hydrogen exclusivity cuts. The hydrogen cuts are calculated using the results of Gaussian fits on exclusivity variables and selecting events within 3σ.

However, hydrogen events might still lie beyond the $\pm 3\sigma$ cut. In order to remove most of the hydrogen contamination from the data, the hydrogen cuts are studied at different sigmas on the NH_3 data with the carbon exclusivity cuts applied. Figure 4.12 shows the results of varying the hydrogen cuts on the $MM_X^2(ep)$ distribution. With a subtraction at 3σ, a small peak at $MM_X^2(ep) = 0$ Gev^2/c^4 is still present. Cutting at 4σ reduces the peak, however a bump is still visible. Finally, the 5σ subtraction greatly suppressed the hydrogen peak and will be adopted for this analysis.

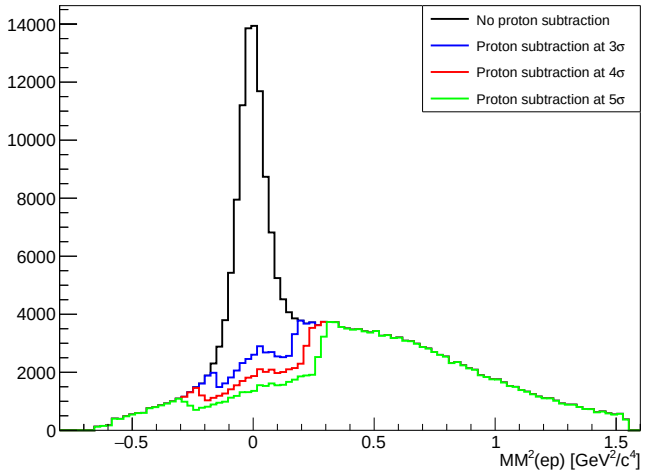

FIGURE 4.12 – Part B - IC distribution of $MM_X^2(ep)$ with the carbon exclusivity cuts applied. The colored lines represent different σ values used to subtract the hydrogen events: the black line is the distribution without any proton subtraction, the blue line is the distribution with protons subtracted at 3σ, the red line is at 4σ and the green line is at 5σ.

4.5.b – *Distribution Centers Study*

After the hydrogen subtraction and following the same procedure used to find the carbon exclusivity cuts, the center of each distribution is studied by applying narrow cuts on $\Delta\phi$, $\theta_{\gamma,epX}$, $MM^2_X(ep\gamma)$ and $p_{\perp,X}(ep\gamma X)$ (see figures 4.13 and 4.14). Some of the cuts applied for this center study are smaller than the 5σ hydrogen cuts used for the subtraction, therefore the holes appearing in some of the distributions are the artifact of this subtraction and render an exact and a precise reading of the distributions means complicated. Nonetheless, the observed shifts in the missing energy, $MM^2_X(e\gamma)$ and $MM^2_X(ep)$ (for the IC) are consistent with the effect found in the carbon event selection. The confirmation of similar shifts between the nitrogen and carbon events allows for the use of the previously calculated carbon exclusivity cuts as a starting point in the determination of the nitrogen exclusivity cuts.

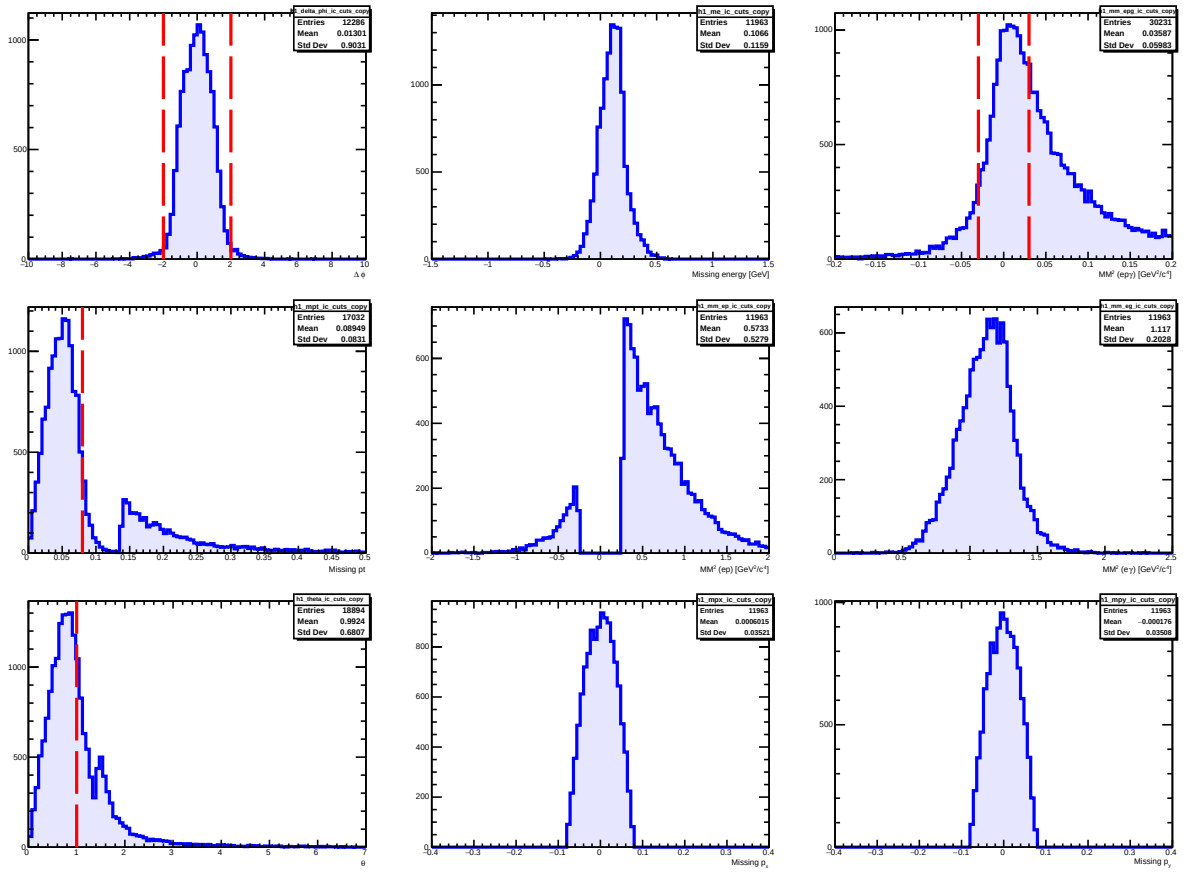

FIGURE 4.13 – Part B - IC distributions of the coplanarity $\Delta\phi$, cone angle $\theta_{\gamma,epX}$, missing masses squared, missing energy and momentum (p_x and p_y) and missing transverse momentum $p_{\perp,X}(ep\gamma X)$. The vertical line are the narrow cuts applied to study the center of the exclusivity variable distributions.

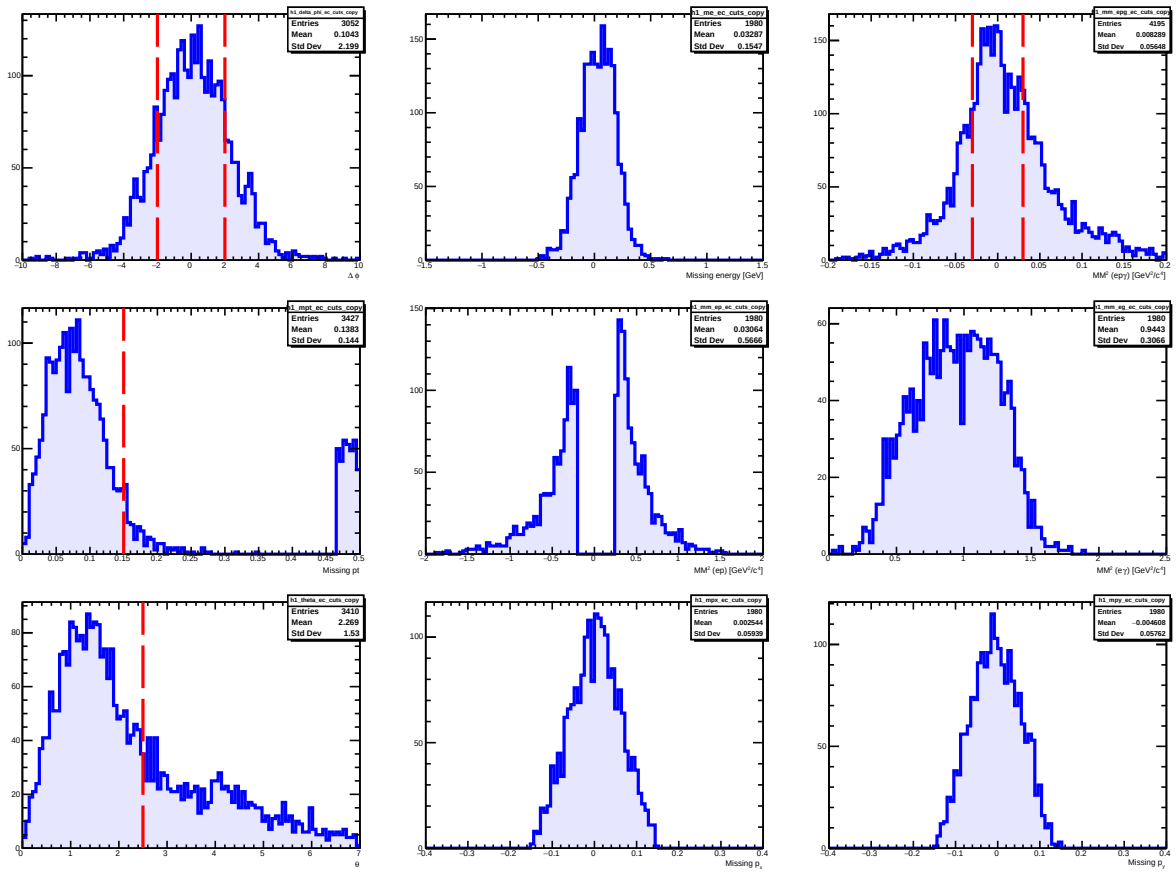

FIGURE 4.14 – Part B - EC distributions of the coplanarity $\Delta\phi$, cone angle $\theta_{\gamma,epX}$, missing masses squared, missing energy and momentum (p_x and p_y) and missing transverse momentum $p_{\perp,X}(ep\gamma X)$. The vertical line are the narrow cuts applied to study the center of the exclusivity variable distributions.

Finally, with the carbon exclusivity cuts as a starting point and after several iterations, the nitrogen events are kept within 2 standard deviations of the mean of each exclusivity variable distributions. Tables 4.3 and 4.4 summarize the calculated nitrogen exclusivity cuts, which are displayed in figures 4.15, 4.16, 4.17 and 4.18 .

Variable	IC	
	Part A	Part B
$\Delta\phi$ [°]	[-4.485, 4.669]	[-4.376, 4.349]
Missing Energy [GeV]	[-0.173, 0.478]	[-0.148, 0.487]
MM^2 (epγ) [GeV^2/c^4]	[-0.0663, 0.0562]	[-0.0626, 0.0595]
$p_{\perp,X}(ep\gamma X)[GeV]$	< 0.197	< 0.201
MM^2 (ep) [GeV^2/c^4]	[-0.572, 1.528]	[-0.531, 1.568]
MM^2 (epγ) [GeV^2/c^4]	[0.633, 1.701]	[0.678, 1.733]
$\theta(\gamma, epX)$ [°]	< 3.167	< 3.030

TABLE 4.3 – Nitrogen cuts for the IC photon topology and differentiated for part A and B of the experiment.

Variable	EC	
	Part A	Part B
$\Delta\phi$ [°]	[-4.689, 4.926]	[-5.114, 5.347]
Missing Energy [GeV]	[-0.216, 0.537]	[-0.223, 0.529]
MM^2 (epγ) [GeV^2/c^4]	[-0.0932, 0.0805]	[-0.0931, 0.0851]
$p_{\perp,X}(ep\gamma X)[GeV]$	< 0.231	< 0.214
MM^2 (ep) [GeV^2/c^4]	[-0.785, 1.007]	[-0.804, 1.179]
MM^2 (epγ) [GeV^2/c^4]	[0.441, 1.758]	[0.476, 1.742]
$\theta(\gamma, epX)$ [°]	< 5.468	< 5.315

TABLE 4.4 – Nitrogen cuts for the EC photon topology and differentiated for part A and B of the experiment.

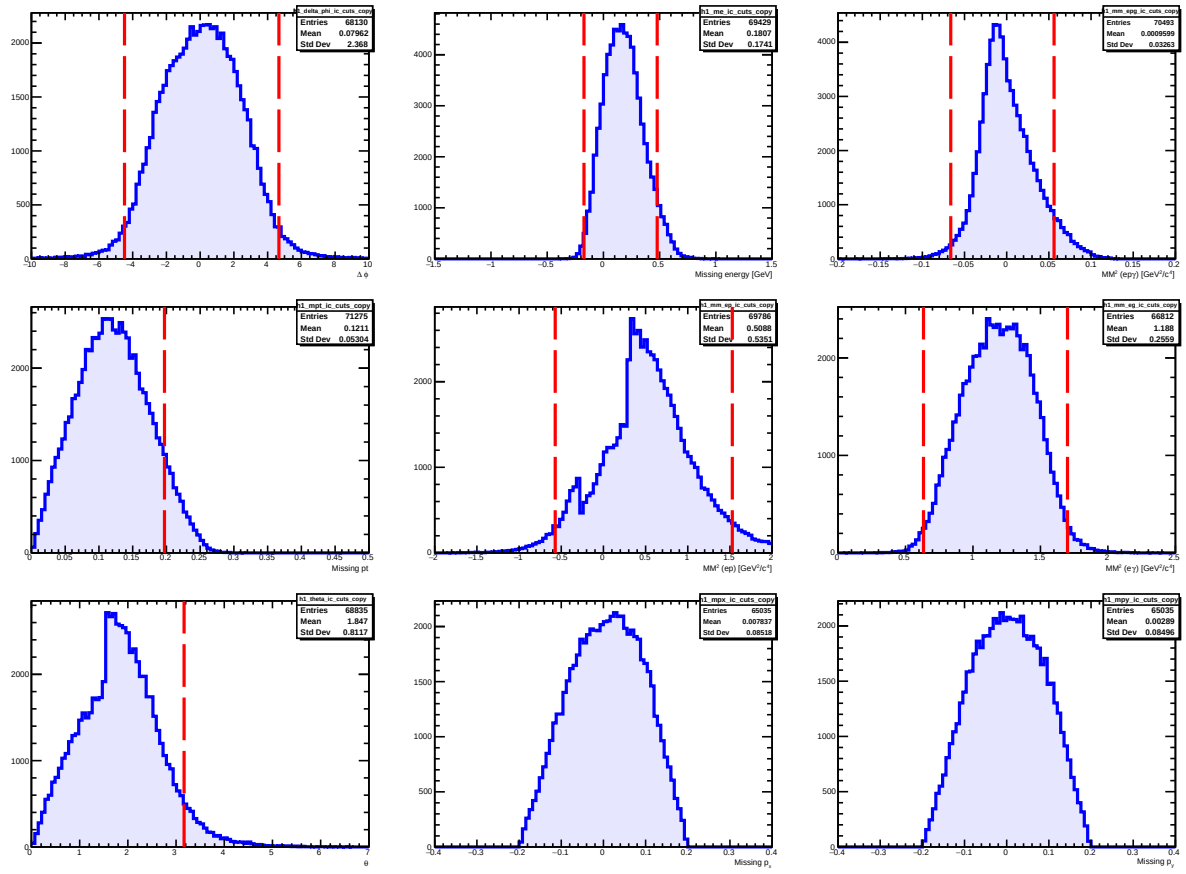

FIGURE 4.15 – Part A - IC nitrogen DVCS event distributions of the coplanarity $\Delta\phi$, cone angle $\theta_{\gamma,epX}$, missing masses squared, missing energy and momentum (p_x and p_y) and missing transverse momentum $p_{\perp,X}(ep\gamma X)$. Each distribution shows the events passing the exclusivity cuts except the one of the variable being drawn (cuts are the vertical red lines).

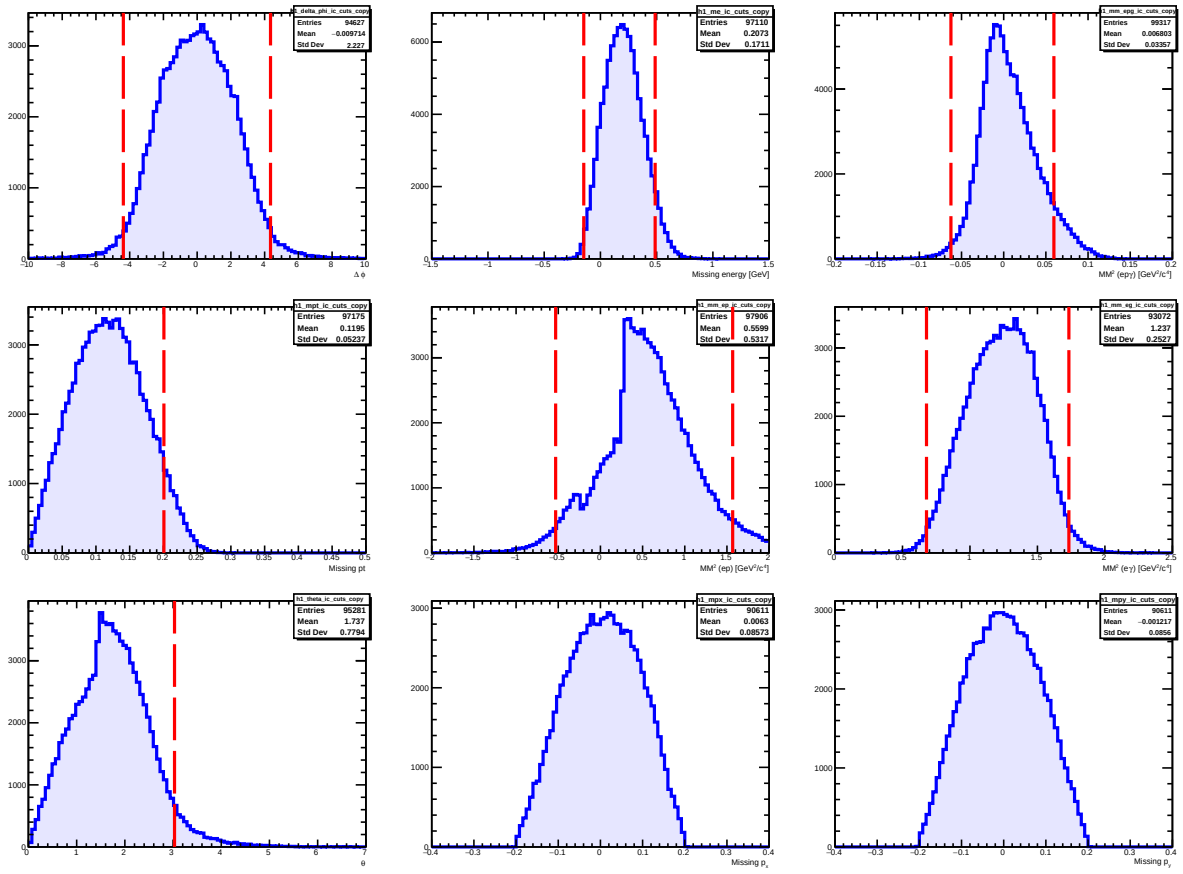

FIGURE 4.16 – Part B - IC nitrogen DVCS event distributions of the coplanarity $\Delta\phi$, cone angle $\theta_{\gamma,epX}$, missing masses squared, missing energy and momentum (p_x and p_y) and missing transverse momentum $p_{\perp,X}(ep\gamma X)$. Each distribution shows the events passing the exclusivity cuts except the one of the variable being drawn (cuts are the vertical red lines).

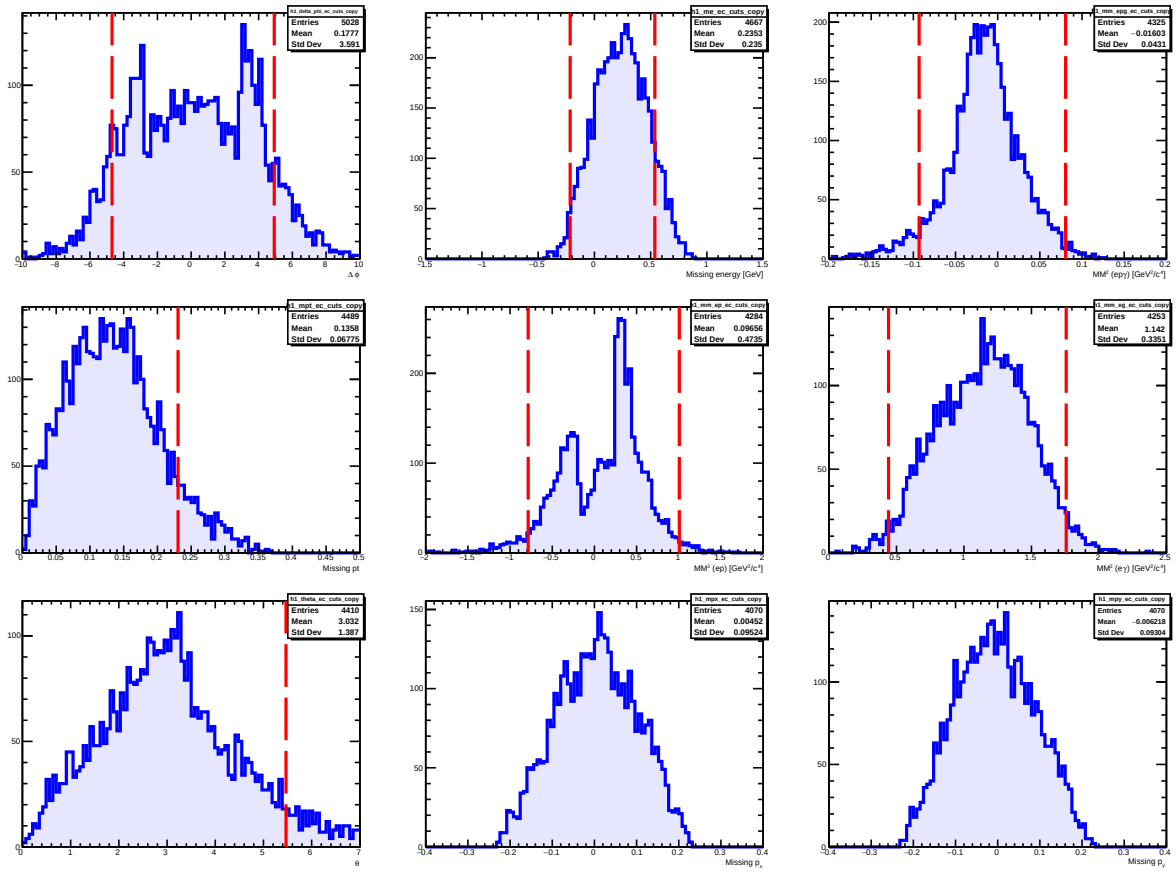

FIGURE 4.17 – Part A - EC nitrogen DVCS event distributions of the coplanarity $\Delta\phi$, cone angle $\theta_{\gamma,epX}$, missing masses squared, missing energy and momentum (p_x and p_y) and missing transverse momentum $p_{\perp,X}(ep\gamma X)$. Each distribution shows the events passing the exclusivity cuts except the one of the variable being drawn (cuts are the vertical red lines).

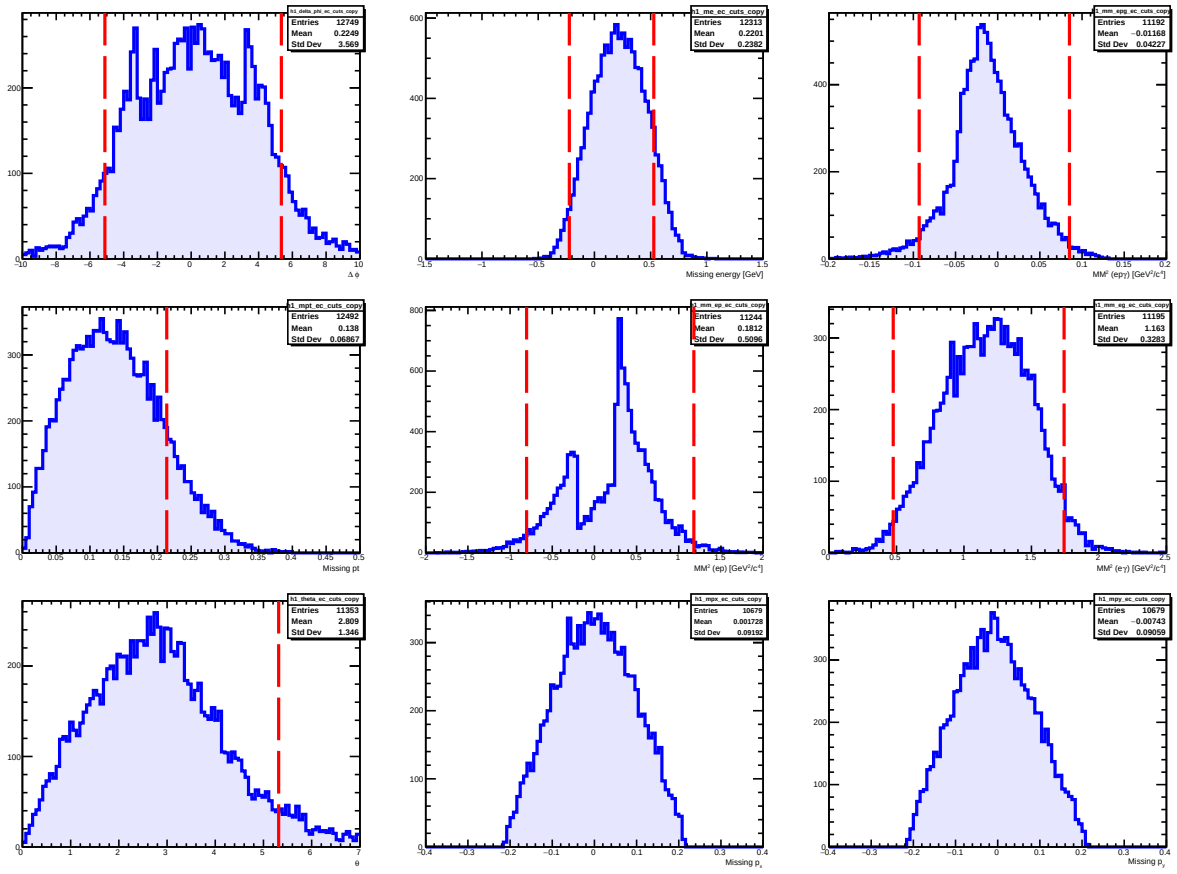

FIGURE 4.18 – Part B - EC nitrogen DVCS event distributions of the coplanarity $\Delta\phi$, cone angle $\theta_{\gamma,epX}$, missing masses squared, missing energy and momentum (p_x and p_y) and missing transverse momentum $p_{\perp,X}(ep\gamma X)$. Each distribution shows the events passing the exclusivity cuts except the one of the variable being drawn (cuts are the vertical red lines).

CHAPTER 5

Results

The following chapter will detail the procedure used to calculate the Beam Spin Asymmetries (BSA) using incoherent nitrogen DVCS events identified in the previous chapter. First, the kinematic coverage, as well as the binning used to calculate the BSAs, will be discussed; followed by the calculation of nitrogen BSAs and Generalized EMC effect ratios. Finally, the results will be compared to the published ^{4}He DVCS and a comparison to DVCS results on nucleus of different numbers of nucleons will be made.

5.1

Kinematic Coverage

The number of identified DVCS events on nitrogen is about 58K for the part A of the experiment and 105K for part B. Figures 5.1, 5.2 and 5.3 show the kinematics coverage of the DVCS events (only the part B events are shown). The Q^2 as a function of x_B is delimited by the set of kinematic cuts applied: $p_e > 0.8$ GeV, $Q^2 > 1$ GeV^2 and W > 2 GeV. The electron acceptance of the CLAS detector also delimits the shape of the distribution ($21^\circ < \theta_e < 45^\circ$). Figure 5.3 shows how the DVCS variables -t and ϕ compare with respect to the detector used to measure the photon. The IC events have smaller -t values than the EC events and do not share the same ϕ coverage.

5.1.a – Binning

The BSA defined in section 1.5 depends on ϕ. Therefore, we will extract BSAs for different values of Q^2, x$_B$ and -t. Due to our limited statistics, each Q^2, x$_B$ and -t distributions will be divided in 8 bins, each containing about the same number of events. The selected binning for this analysis is detailed in table 5.1. Finally, the asymmetries for each Q^2, x$_B$ and -t bin will be plotted as a function of 10 bins of ϕ.

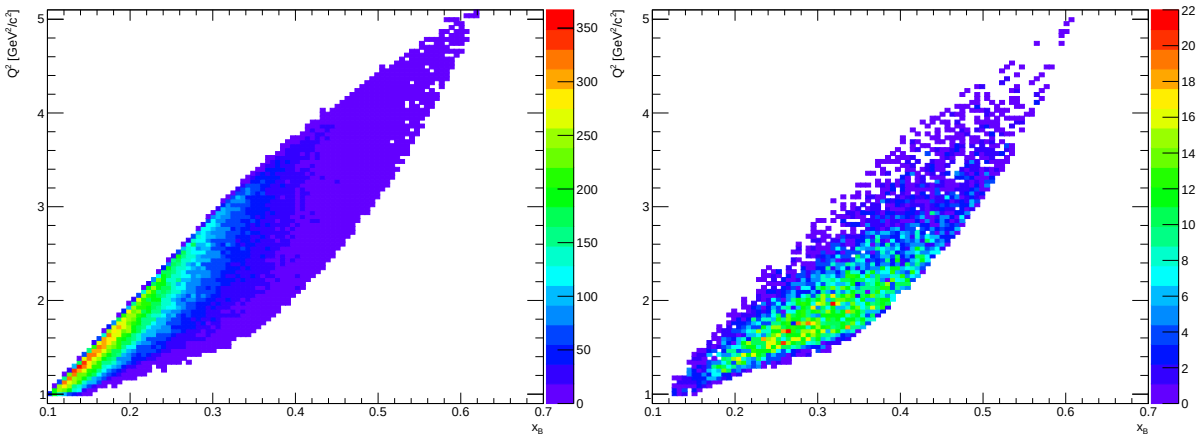

FIGURE 5.1 – Distributions Q^2 as a function of x_B for the DVCS events of part B. Left: Events with photons being detected by the IC. Right: Events with photons being detected by the EC.

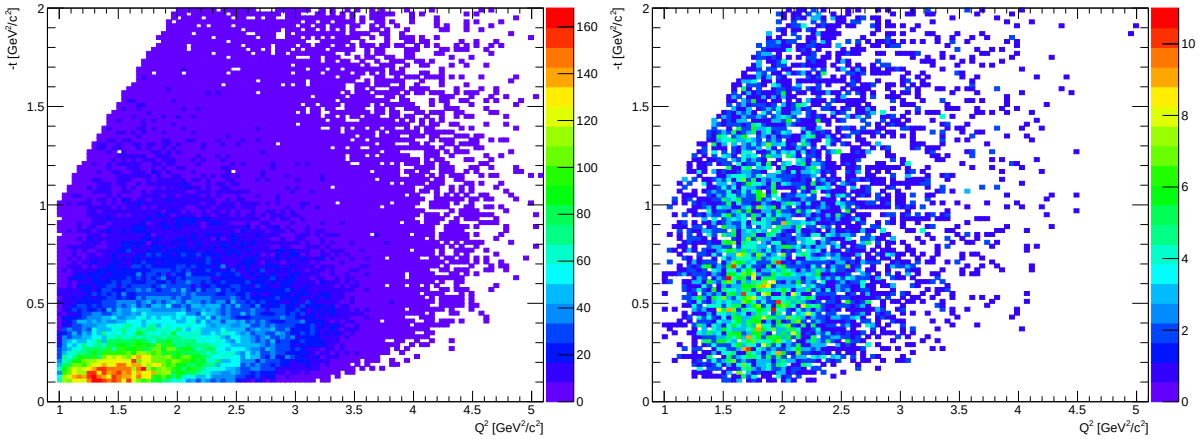

FIGURE 5.2 – Distributions -t as a function of Q^2 for the DVCS events of part B. Left: Events with photons being detected by the IC. Right: Events with photons being detected by the EC.

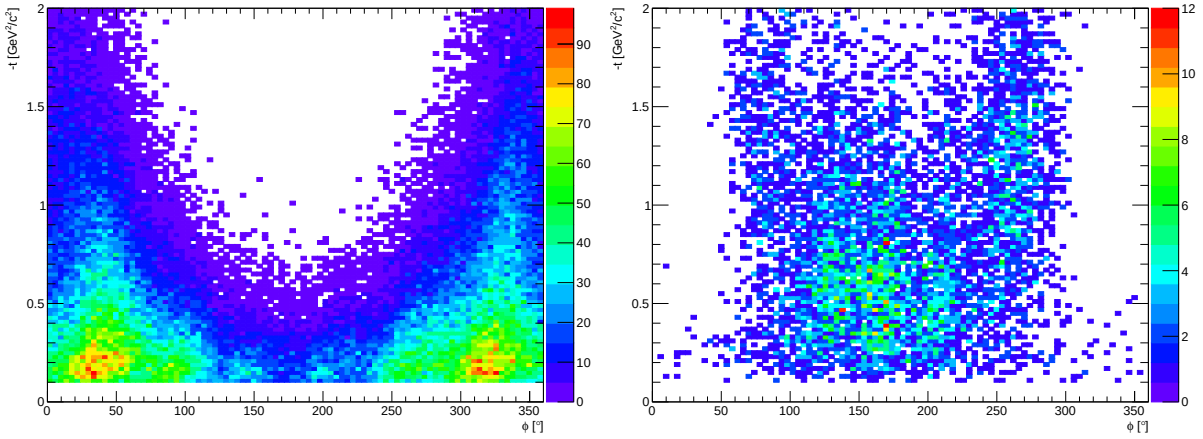

FIGURE 5.3 – Distributions -t as a function of ϕ for the DVCS events of part B. Left: Events with photons being detected by the IC. Right: Events with photons being detected by the EC.

Bin number	Q^2 [GeV^2/c^2]	x_B	-t [GeV^2/c^2]
1	[1.0, 1.35]	[0.1, 0.17]	[0.1, 0.17]
2	[1.35, 1.6]	[0.17, 0.2]	[0.17, 0.24]
3	[1.6, 1.8]	[0.2, 0.23]	[0.24, 0.32]
4	[1.8, 2.0]	[0.23, 0.26]	[0.32, 0.42]
5	[2.0, 2.3]	[0.26, 0.29]	[0.42, 0.56]
6	[2.3, 2.6]	[0.29, 0.33]	[0.56, 0.77]
7	[2.6, 3.1]	[0.33, 0.39]	[0.77, 1.13]
8	[3.1, 5.0]	[0.39, 0.6]	[1.13, 3.5]

TABLE 5.1 – Definition of the 1-dimensional binning in Q^2, x_B and -t.

5.2

Nitrogen Beam Spin Asymmetries

The BSA, also called A_{LU}, is defined as:

$$A_{\mathrm{LU}} = \frac{1}{P_B}\frac{N^+ - N^-}{N^+ + N^-} \tag{5.1}$$

where P_B is the average polarization of the electron beam and $N^{\pm}$ is the number of events for each beam helicity configuration (positive or negative). The proton eg1-dvcs analysis calculated the polarization of the beam using the Hall B Møller polarimeter. The polarization was found to be 0.86 ± 0.03 for part A and 0.837 ± 0.017 for part B [68].

Figures 5.4, 5.5 and 5.6 show the incoherent nitrogen BSA for the distributions Q^2-ϕ, x_B-ϕ and -t-ϕ. Each bin is fitted using the following formula:

$$A_{\mathrm{LU}} = \frac{\alpha \sin(\phi)}{1 + \beta \cos(\phi)} \tag{5.2}$$

where α and β are the fitting coefficients. The formula corresponds to the expected shape of the BSAs and the fitting coefficients relate to the H CFFs (see section 1.5) which can be calculated after a phenomenological analysis [72].

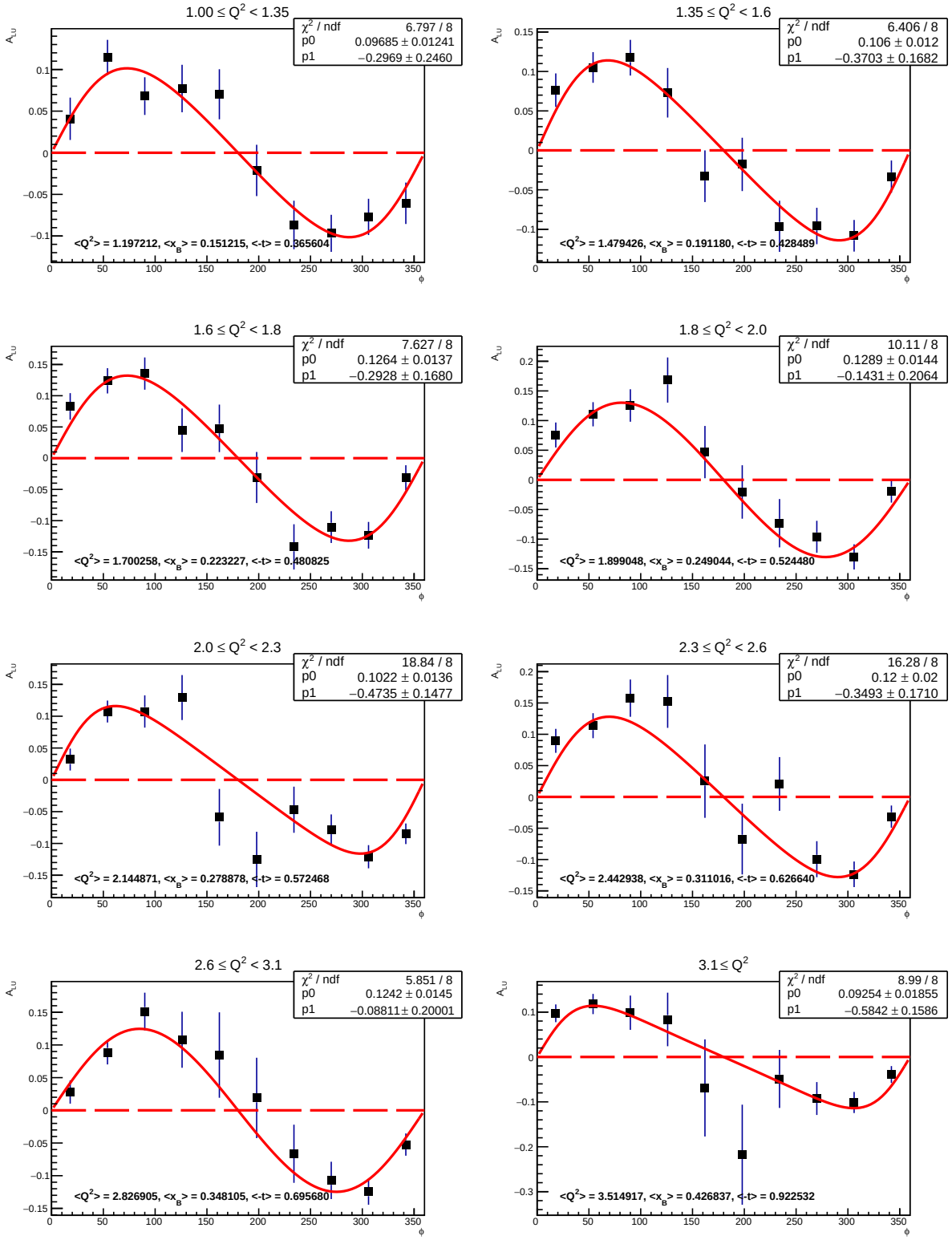

FIGURE 5.4 – Incoherent nitrogen A_{LU} as a function of ϕ for 8 bins of Q^2. The blue lines are the statistical errors, and the red curve is the result of the fit.

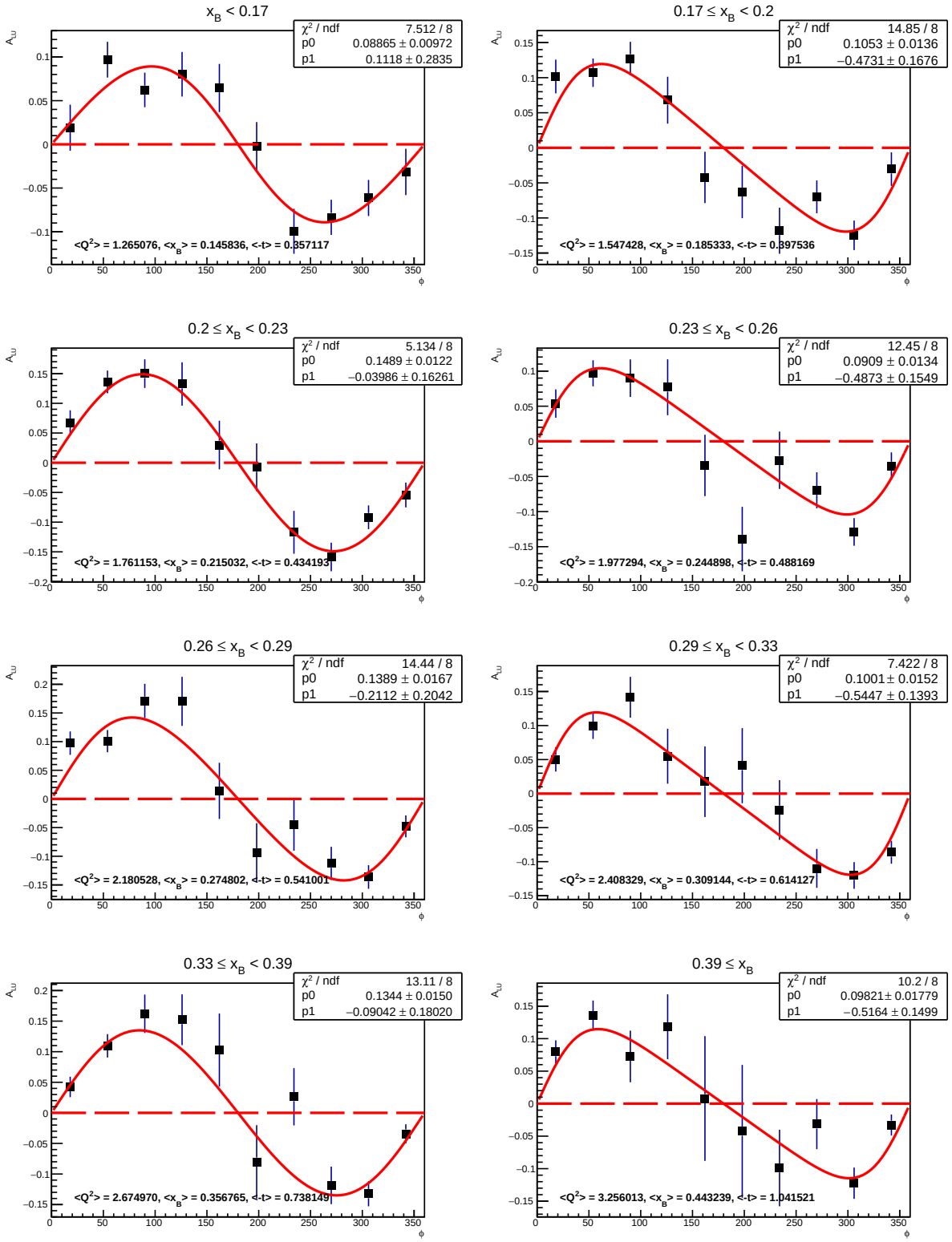

FIGURE 5.5 – Incoherent nitrogen A_{LU} as a function of ϕ for 8 bins of x_B. The blue lines are the statistical errors, and the red curve is the result of the fit.

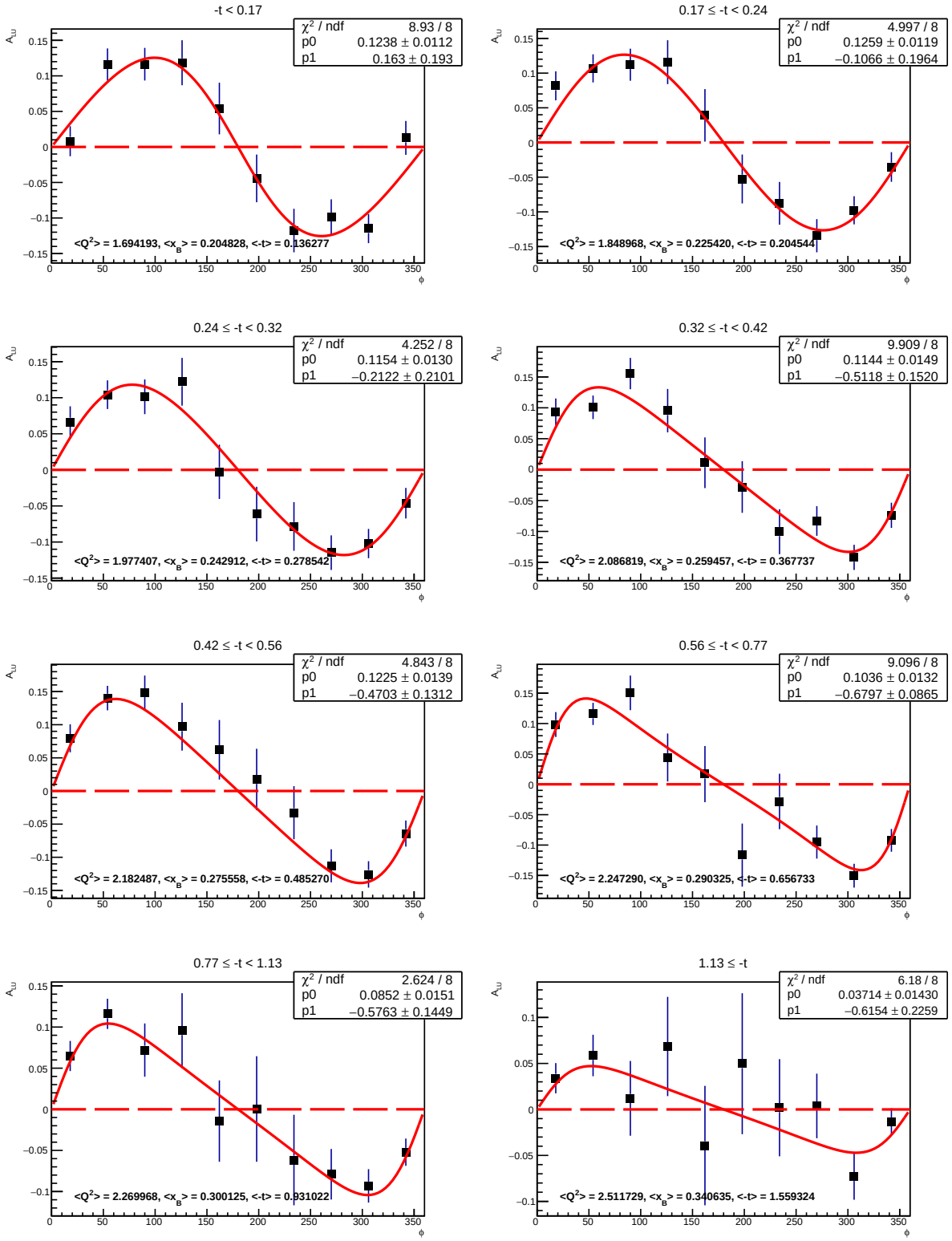

FIGURE 5.6 – Incoherent nitrogen A_{LU} as a function of ϕ for 8 bins of -t. The blue lines are the statistical errors, and the red curve is the result of the fit.

The fit in equation 5.2 allows to extract the A_{LU} at $\phi = 90^\circ$ for each bins in Q^2, x_B and -t. In figures 5.7, 5.8 and 5.9, $A_{LU}(90^\circ)$ - also called BSA amplitudes - are compared with the ^{4}He DVCS analysis [44]. The mean value of the amplitudes is obtained by linearly fitting each result, and the nitrogen amplitudes are found to be about 30% smaller than the helium-4 amplitudes. While the amplitude as a function of Q^2 and x_B appears to be linear, a decrease is noticeable in the -t distribution for which we probe larger values than ^{4}He. The number of nitrogen events is also larger than the number of helium-4 events, hence the nitrogen analysis was done using smaller bins with greater statistics which is reflected in the smaller error bars obtained.

We can notice in figure 5.8 an oscillating behavior of the nitrogen points. This effect is due to the fit which privileges the cosine term in equation 5.2. This instability is the result of the local fitting method used which does not work well in some of the BSA (i.e. in the bin $2.0\text{GeV}^2/c^4 < Q^2 < 2.3\text{GeV}^2/c^4$ of figure 5.4) and finds several local minima, This effect is discussed in detail in [72].

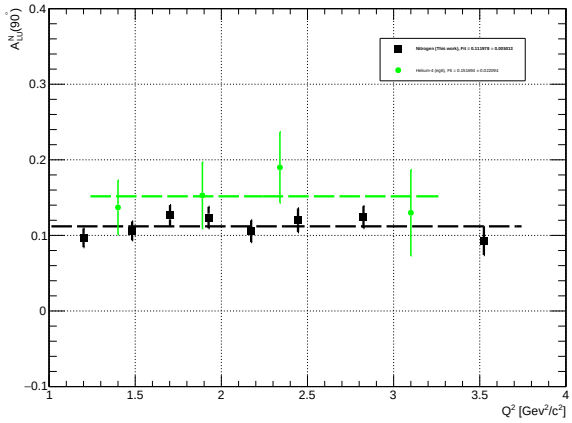

FIGURE 5.7 – The amplitude of the asymmetry A_{LU} (at $\phi = 90^\circ$) as a function of Q^2. The black points are the nitrogen events and the green points are the helium-4 events.

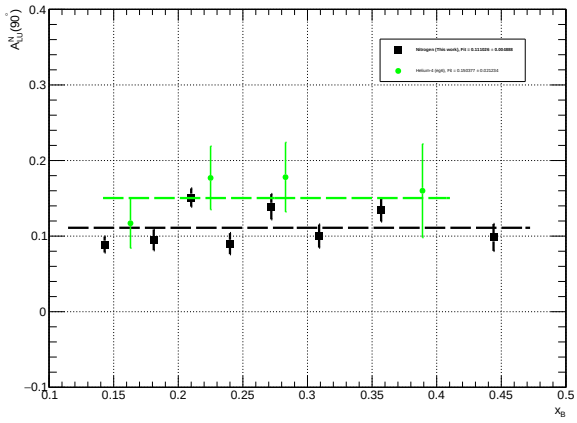

FIGURE 5.8 – The amplitude of the asymmetry A_{LU} (at $\phi = 90^\circ$) as a function of x_B. The black points are the nitrogen events and the green points are the helium-4 events.

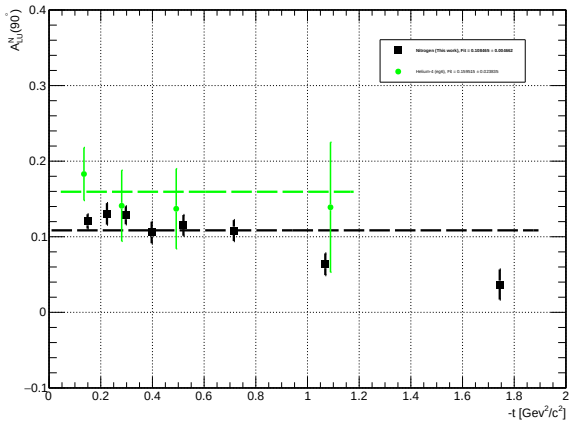

FIGURE 5.9 – The amplitude of the asymmetry A_{LU} (at $\phi = 90^\circ$) as a function of -t. The black points are the nitrogen events and the green points are the helium-4 events.

5.3

Generalized EMC ratios

As mentioned in section 1.3, the ratio of DIS cross-sections of bound nucleons and free nucleons is not equal to unity. This result, known as the EMC effect, shows the effect of the nuclear medium on bound nucleon. Using the BSAs of DVCS events, a similar test can be made using the ratio of bound nucleon (nitrogen) and free nucleon (hydrogen).

Since the eg1-dvcs experiment allowed the measurement of BSA on hydrogen and nitrogen, the ratio $A_{LU}^{A}/A_{LU}^{p}(90^\circ)$ can be obtained without any further corrections. First, the hydrogen BSA is extracted using the same binning as the nitrogen analysis. Finally, the ratios are calculated and are shown in figures 5.10, 5.11 and 5.12. These ratios are also compared to the results of the eg6 helium-4 DVCS experiment.

Compared to the amplitudes showed in the previous section, the points of the Generalized EMC ratio between the nitrogen and the helium are closer. One of the reasons that would require further study to explain this behavior, is related to the data set of the free proton used to calculate the ratios. The eg6 ^{4}He result used interpolation of the published data from the e1-dvcs2 CLAS experiment, while this analysis used the data from the same experiment. The methods used to extract the A_{LU}^{p} are also different between the helium and nitrogen analysis. Since the helium-4 result rely on the proton asymmetries from a different experiment, the amplitude of the proton BSAs had to be extracted by extrapolating the results to match the binning used in the ^{4}He analysis. While this work re-applies the same procedure, used to calculate the nitrogen BSAs, on the hydrogen events, and respects the same binning.

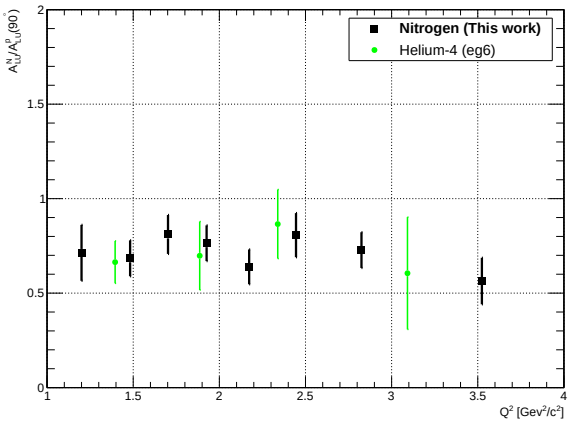

FIGURE 5.10 – The ratio of asymmetry amplitude $A_{LU}^A / A_{LU}^p(90^\circ)$ as a function of Q^2. The black points are the nitrogen events and the green points are the helium-4 events.

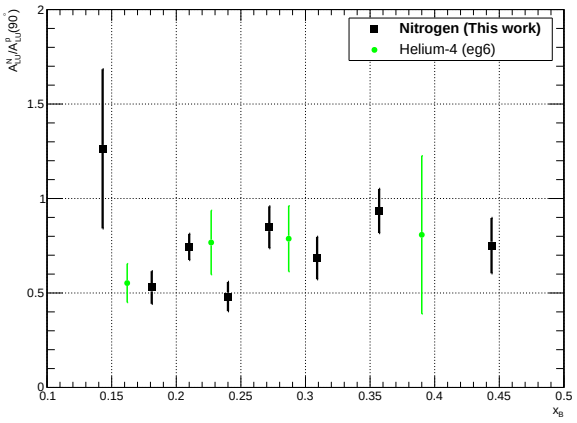

FIGURE 5.11 – The ratio of asymmetry amplitude $A_{LU}^A / A_{LU}^p(90^\circ)$ as a function of x_B. The black points are the nitrogen events and the green points are the helium-4 events.

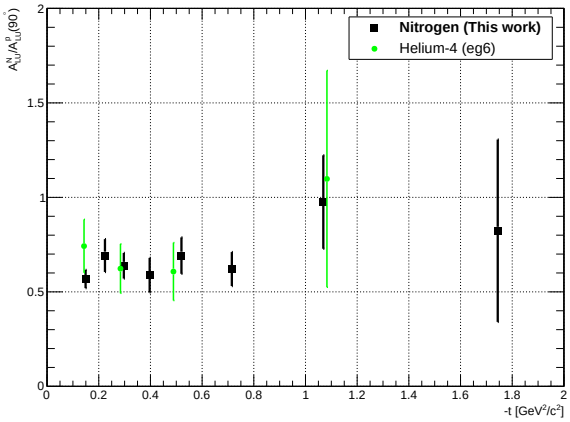

FIGURE 5.12 – The ratio of asymmetry amplitude $A_{LU}^A / A_{LU}^p(90^\circ)$ as a function of -t. The black points are the nitrogen events and the green points are the helium-4 events.

5.4

Nuclear Dependence

The EMC effect shows a correlation between the slope value of EMC ratios and the nucleus density (see figure 1.8). A similar correlation is found when comparing the mean value of the asymmetry's amplitudes as a function of the density expressed as $A^{-1/3}$ (see figure 5.13). As $A^{-1/3}$ increases, the amplitude of the BSAs increases as well. This observation highlights an EMC like effect in the ratio of the DVCS asymmetries between bound nucleon and free proton, and offers a new way to study the impact of the nuclear medium on bound nucleon.

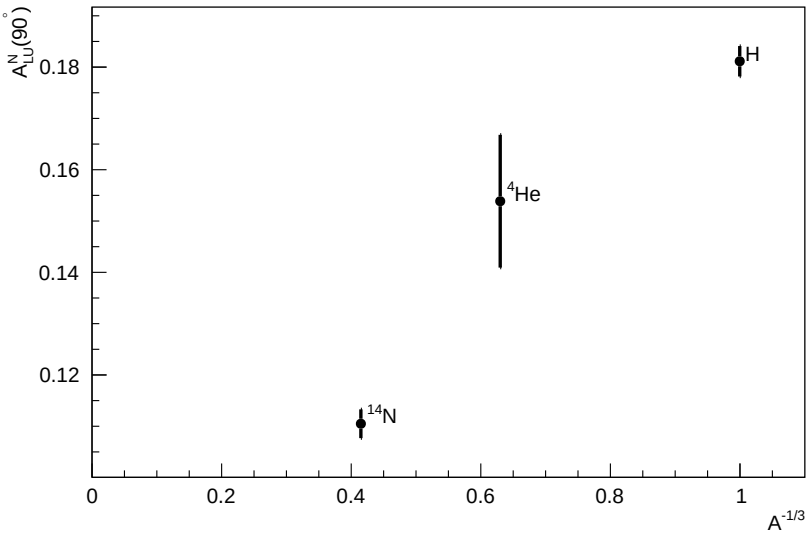

FIGURE 5.13 – The mean value of A_{LU}^{A} amplitudes as a function of the nucleus density expressed as $A^{-1/3}$.

Conclusion

The EMC effect revealed that our current understanding of the bound nucleon structure is incomplete. After 35 years of experiments and theoretical work, the EMC effect still remains unsolved. However, a number of experimental programs measured this effect on different nuclei and found a correlation between the nuclear density and the strength of the EMC effect. The nuclear GPDs framework - via nuclear DVCS measurements - is one of the new approaches used to study the nuclear medium and its effect on the nucleons.

This thesis presented the measurements of incoherent DVCS off nitrogen using the CLAS detector at Jefferson Laboratory. The analysis was performed using the NH_3 data which was initially taken to measure DVCS off polarized protons. While the proton channel has been analyzed and published, the nitrogen channel was not exploited. An experimental and theoretical review of the lepton-nucleon scattering was made with the emphasis on the EMC effect and the DVCS. A brief overview of the accelerator and the experimental setup was also presented. The analysis is divided in three main parts: first, the identification of final state particles was performed, followed by the determination of cuts ensuring the exclusivity of the DVCS process, and finally the extraction of BSAs. The nitrogen BSA results are then compared to the published helium-4 results.

The extracted nitrogen BSAs show smaller amplitudes when compared to helium-4 which are smaller than on the free proton. These two results have been also compared to the free protons results, and the mean values of the nuclear BSA amplitudes are found to be lower than those of the free proton. We notice also a correlation between the nucleus density and the amplitude of the BSAs: as the nuclear density decreases, the amplitude of the BSA decreases as well. This result confirms this new nuclear effect and give a first indication about its A dependence.

In the near future, this experimental program will be extended at Jefferson Laboratory which recently doubled its electron beam energy to reach 12 GeV. This increase in energy was accompanied with the upgrade of the CLAS detector, now called CLAS12. The CLAS12 program has a number of proposed run groups aimed at the measurement of nuclear DVCS. These future results will benefit from the higher luminosity available in CLAS12 and the extended kinematic coverage offered by the higher beam energy.

Résumé en français

Introduction

Les protons et les neutrons sont les composants de la matière et représentent 99% de la masse de l'univers visible. Jusqu'au début des années 1930, le proton était considéré comme une particule ponctuelle et élémentaire. Cependant, les expériences de diffraction de Frisch et Stern ont mesuré le moment magnétique du proton, et ont trouvé un résultat incompatible avec une particule ponctuelle. Dans les années 1950, ce résultat a été confirmé par les expériences de diffusion élastique d'électrons de Hofstadter qui ont mesuré les distributions spatiales électromagnétiques, desquels ont été déduites la taille du proton ($\sim 10^{-13}$ cm).

Suite aux expériences de Hofstadter, les sondes électromagnétiques ont été largement utilisées pour étudier la structure du proton. À la fin des années 1960, un nouveau type de diffusion d'électron a été réalisé: la diffusion profondément inélastique (DIS). En augmentant l'énergie des faisceaux de lepton, ces nouvelles expériences ont pu sonder de petites distances à l'intérieur du nucléon et ont conduit à la découverte des constituants des nucléons, les quarks. Les protons et les neutrons ne sont plus considérés comme des particules élémentaires de la matière, mais plutôt comme des particules composées de quarks liés par les gluons, le boson de jauge de l'interaction forte. Les expériences DIS permettent l'extraction des fonctions de distributions de parton (PDF), qui sont les densités de probabilité de trouver un parton portant une certaine fraction de l'impulsion longitudinale du nucléon.

L'interaction forte confine les quarks dans le nucléon et, à plus grande échelle, lie les nucléons dans les noyaux atomiques. Après une série de mesures DIS sur différents noyaux, les propriétés des quarks dans les nucléons liés se sont révélées différentes de celles des quarks à l'intérieur d'un nucléon libre. Nommé d'après l'expérience qui a mesuré en premier ce comportement, l'effet EMC (*European Muon Collaboration*) dévoile des phénomènes à l'intérieur du noyau affectant les propriétés des quarks et la manière dont ils composent les nucléons. Aujourd'hui, l'effet EMC continue d'être étudié et divers modèles théoriques tentent d'expliquer ce comportement. Néanmoins, à ce jour, les zones d'ombre persistent et nous n'avons pas de bonne compréhension de ces effets nucléaires.

Un nouvel ensemble de fonctions de structure, appelé distributions de parton généralisées (GPDs), ont été introduites à la fin des années 1990 et corrèlent l'impulsion longitudinal d'un parton avec sa position transversale. Les GPDs sont extraites de réactions exclusives, telles que la diffusion Compton profondément virtuelle (DVCS, $ep \rightarrow e'p'\gamma$).

Bien que des programmes de physique approfondis visant à mesurer les DVCS sur le proton aient été effectués au sein de différents laboratoires tels que le *Jefferson Laboratory*, peu de résultats existent sur les noyaux plus lourds. Les mesures des GPDs sur les noyaux pourraient constituer une approche différente pour étudier l'effet EMC et comprendre la structure sous-jacente des nucléons à l'intérieur du noyau.

Situé aux États-Unis, le *Jefferson Laboratory* est conçu pour étudier les quarks à l'intérieur du nucléon. Au moment de l'expérience, le faisceau d'électrons polarisés de 6 GeV alimentait 3 halls d'expérimentation (A, B et C) abritant chacun un spectromètre. Le détecteur CLAS du Hall B était un spectromètre à large acceptance, conçu pour mesurer plusieurs particules dans l'état final à grands angles. La mesure des GPDs est le sujet d'un programme de physique approfondi au *Jefferson Laboratory* et plusieurs résultats DVCS ont été publiés à l'aide des données CLAS.

Ce manuscrit est organisé en cinq chapitres :

- Le chapitre 1 est une introduction à la diffusion de leptons sur les nucléons avec un accent sur l'étude de la structure des nucléons à l'intérieur du noyau (effet EMC). La dernière partie de ce chapitre détaille les propriétés des GPDs et la réaction DVCS utilisée pour y accéder ;
- Le chapitre 2 décrit l'appareil expérimental utilisé par l'expérience eg1-dvcs. Une introduction de l'accélérateur est faite, suivie d'une présentation du détecteur CLAS ;
- Le chapitre 3 répertorie toutes les coupes utilisées pour identifier l'électron, le proton et le photon qui sont les particules de l'état final du DVCS ;
- Le chapitre 4 résume la procédure appliquée pour identifier les événements du DVCS incohérents sur l'azote en utilisant une cible NH_3. La méthode utilisée pour identifier et soustraire les événements hydrogène est discutée, avant que les coupes pertinentes assurant l'exclusivité de la réaction ne soient appliquées ;
- Le chapitre 5 conclut avec l'extraction des résultats des asymétries DVCS de l'azote. Les résultats sont également comparés aux mesures DVCS sur l'hélium-4.

Motivations physiques

Les constituants des nucléons ont été historiquement nommés partons par Feynman, et un modèle théorique est né de leur découverte. Le modèle des partons a décrit avec succès comment les partons sont combinés et forment les nucléons. En définitive, une nouvelle théorie quantique des champs - appelée chromodynamique quantique (QCD) - a été développée pour expliquer les mécanismes de l'interaction forte, la force liant les quarks chargés de couleur avec leurs bosons de jauge - les gluons. L'une des principales propriétés de la QCD est la liberté asymptotique et détermine quand la théorie des perturbations (pQCD) peut être utilisée. À des énergies comparables à la

masse du nucléon, la constante de couplage de QCD α_s est grande et pQCD ne peut pas être appliqué ; tandis qu'à des énergies plus élevées, α_s devient suffisamment petit pour que pQCD soit utilisé. Une deuxième propriété de la QCD est le confinement de couleur. Le potentiel QCD augmente avec la distance jusqu'à ce que l'énergie soit suffisamment élevée pour créer un quark-antiquark. Par conséquent, les quarks ne peuvent pas être isolés et doivent être combinés afin de créer des objets de couleur neutre.

Le premier type de réaction utilisant des leptons pour sonder les nucléons est les processus de diffusion élastique (ES) (voir figure Fr.1). Lors de cette réaction, le nucléon final est intact et les informations obtenues permettent l'extraction de fonctions, appelées facteurs de formes. Les facteurs de forme de Sachs encodent les distributions spatiales de charge électrique (G_E) et de magnétisation (G_M) d'un nucléon.

En augmentant l'énergie du lepton incident, des distances plus petites que la taille du nucléon peuvent être sondées. Au de la de la limite $Q^2 > 1\ GeV^2/c^2$, le processus est appelé diffusion inélastique profonde (DIS) (voir figure Fr.2) . Dans ce processus, le nucléon se casse et crée un état final X indéfini composé de plusieurs particules. Le calcul de section efficace de DIS donne accès aux fonctions de distribution de partons (PDFs) représentant la probabilité de trouver un parton ayant une fraction x de l'impulsion totale du nucléon.

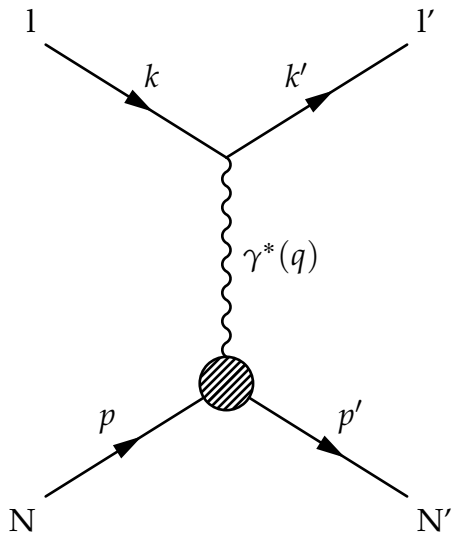

FIGURE FR.1 – Diagramme de Feynman d'une diffusion élastique d'un lepton sur un nucléon.

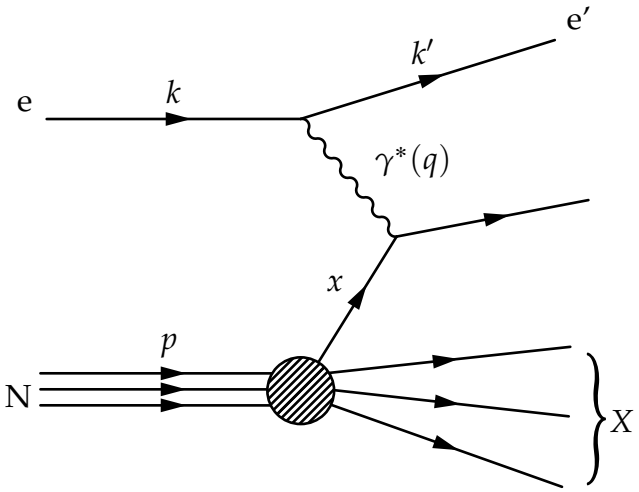

FIGURE FR.2 – Diagramme de Feynman d'une diffusion profondément inélastique d'un électron sur un nucléon.

La *European Muon Collaboration* (EMC) a mesuré les sections efficaces du DIS à l'aide d'un faisceau de muons, allant de 100 GeV à 280 GeV, sur des cibles de fer et de deutérium. L'énergie de liaison des nucléons à l'intérieur du noyau est de l'ordre de quelques MeV et est bien inférieure à la masse d'un nucléon (proche de 1 GeV), par conséquent la comparaison entre les sections efficaces DIS nucléaires et la section efficace DIS un même nombre de nucléons libres peut être naïvement considéré comme similaire, et leur rapport devrait tendre vers l'unité. En 1983, la collaboration EMC a publié le rapport $\mathcal{F}_2^{Fe}/\mathcal{F}_2^{D}$ et observé une pente descendante en fonction de x_B. Ce résultat inattendu démontre la différence de structure des nucléons entre les nucléons à l'intérieur des noyaux et les nucléons libres. Au cours des 35 dernières années, plusieurs programmes expérimentaux ont mesuré un comportement similaire pour diverses cibles nucléaires au CERN, à Desy, au Fermilab, au SLAC et au JLab.

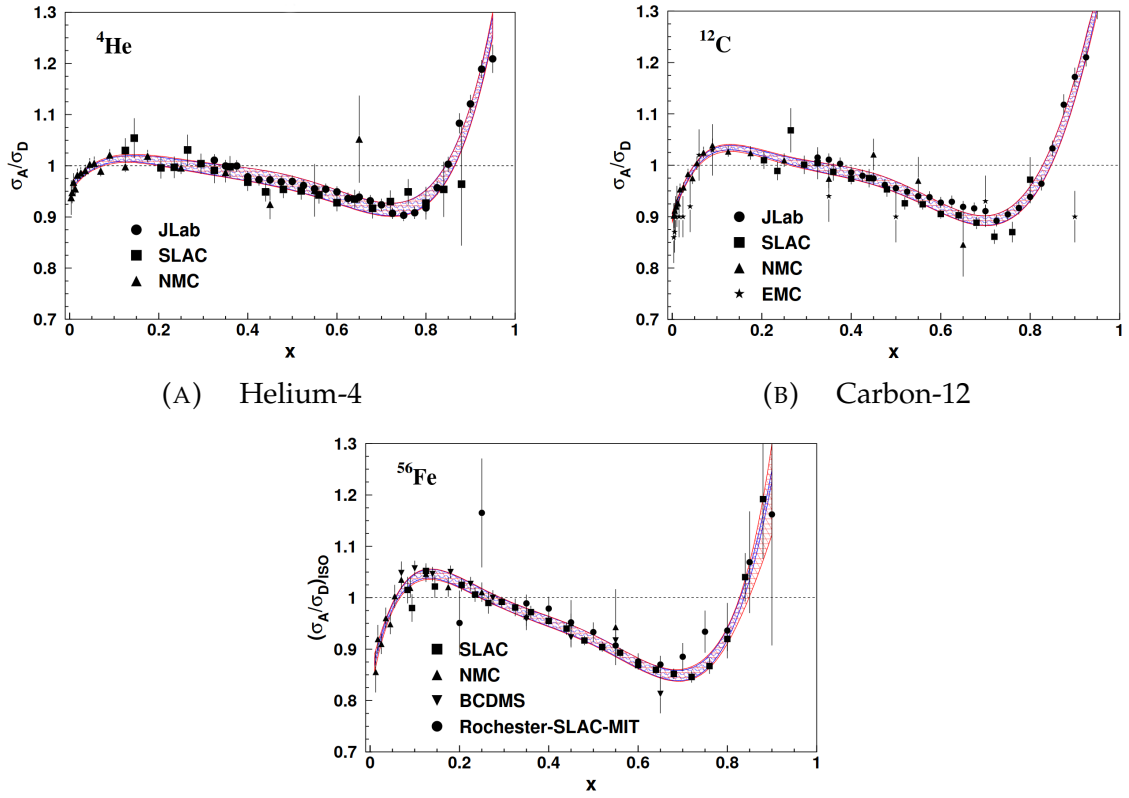

(A) Helium-4 (B) Carbon-12

(C) Iron-56

FIGURE FR.3 – Rapport entre les sections efficaces DIS de différents noyaux (^4He, ^{12}C et ^{56}Fe) et la section efficace du deutérium. Les barres d'erreur représentent les incertitudes statistiques et systématiques. Le bandeau rouge l'erreur de l'ajustement global des données. Figures de [11].

Un nouveau cadre théorique, introduit au début des années 1990, corrèle l'impulsion longitudinale d'un parton et sa position transversale à l'intérieur du nucléon : les distributions généralisées de parton (GPD). Il s'agit de fonctions de structure universelles accessibles via des procédés de diffusion profonde exclusive, tel que l'électroproduction d'un photon réel, la diffusion Compton profondément virtuelle (DVCS) : $l(k) + N(p) \rightarrow l'(k') + N'(p') + \gamma(q')$. Lors de la réaction DVCS, le parton sondé émet un photon (réel) et est réabsorbé par le nucléon.

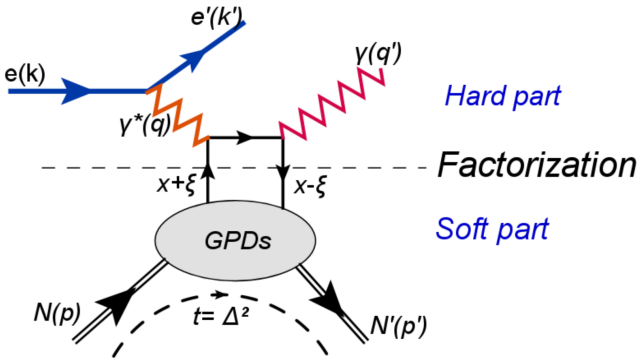

FIGURE FR.4 – Diagramme de Feynman d'une diffusion Compton profondément virtuelle.

Dans le cas du proton (particule de spin 1/2), il existe quatre GPDs qui conservent la chiralité : $H^q(x,\xi,t)$, $E^q(x,\xi,t)$, $\tilde{H}^q(x,\xi,t)$ and $\tilde{E}^q(x,\xi,t)$. $H^q(x,\xi,t)$ et $\tilde{H}^q(x,\xi,t)$ représentent les GPDs lorsque l'hélicité du nucléon est préservée, tandis que $E^q(x,\xi,t)$ et $\tilde{E}^q(x,\xi,t)$ décrivent un renversement d'hélicité. De plus, $H^q(x,\xi,t)$ et $E^q(x,\xi,t)$ sont définies par la somme des états d'hélicité des quarks et des nucléons,et sont donc indépendantes de l'hélicité des quarks ; ils sont appelés GPDs non polarisés. $\tilde{H}^q(x,\xi,t)$ et $\tilde{E}^q(x,\xi,t)$ désignent les GPDs polarisés dépendant de l'hélicité et sont exprimées par la différence des états d'hélicité du quark et du nucléon.

Les GPDs dépendent de trois variables : x, ξ et t. $x+\xi$ est la fraction de l'impulsion longitudinale portée par le quark initial heurté, $x-\xi$ est fraction de l'impulsion longitudinale portée par le quark final réabsorbé, et t est l'impulsion au carré de l'impulsion transférée entre le quark initial et final. ξ et t sont accessibles expérimentalement avec la réaction DVCS, en revanche la variable x ne peut pas être extraite et est intégrée dans l'amplitude DVCS. Cette intégration rend l'intégrale complexe, et pour chaque GPD, une fonction complexe dépendante en ξ et t peut être définie. Ces fonctions sont nommées Facteurs de Forme Compton (CFFs).

Outre le DVCS, un autre processus doit être inclus dans le calcul de l'amplitude de diffusion : la réaction de Bethe-Heitler (BH). Dans ce processus, un photon est émis par l'électron incident ou diffusé, conduisant à un état final similaire $ep \to e'p'\gamma$. Au twist supérieur, les amplitudes de la diffusion peuvent être décomposées, en une somme d'harmoniques de Fourier qui seront utilisés pour calculer les CFFs.

L'accès à spécifique CFF dépend des conditions expérimentales. Dans le cas de la diffusion d'un faisceau polarisé sur une cible non polarisée, deux quantités peuvent être extraites : $\sigma_{\text{unpol}} = \sigma^+ + \sigma^-$ et $\sigma_{\text{pol}} = \sigma^+ - \sigma^-$, où les signes $+$ et $-$ représentent des hélicités de faisceau opposées. La section efficace σ_{unpol} donne accès à la partie réelle de l'amplitude, tandis que σ_{pol} est sensible à la partie imaginaire. Ce travail permettra d'extraire les asymétries de spin du faisceau (BSA) :

$$A_{\text{LU}} = \frac{\sigma^+ - \sigma^-}{\sigma^+ + \sigma^-} \tag{5.3}$$

Le détecteur CLAS au *Jefferson Laboratory*

Le *Jefferson Laboratory* a été établi au milieu des années 1980 en tant que le *Continuous Electron Beam Accelerator Facility* (CEBAF) pour étudier la matière nucléaire et sa structure fondamentale. Le CEBAF était l'un des premiers accélérateurs à grande échelle à utiliser la technologie des cavités résonnante radiofréquences supraconductrices pour accélérer les électrons. L'accélérateur était capable de fournir un faisceau d'électrons de 6 GeV à trois halls d'expérimentation différents (A, B et C) simultanément (voir figure Fr.5).

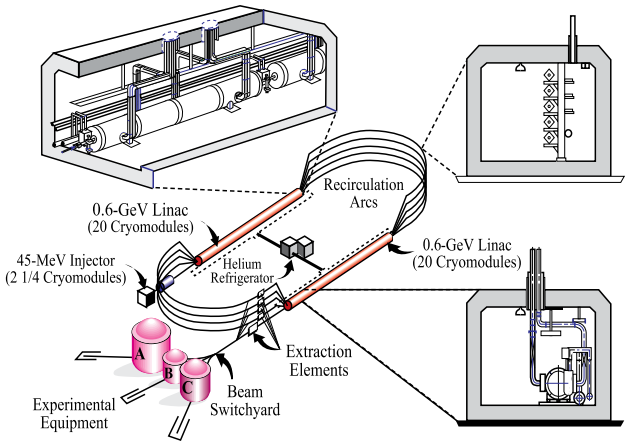

FIGURE FR.5 – Diagramme de CEBAF au *Jefferson Laboratory*

Chaque hall expérimental abrite des instruments uniques et dispose de programmes de physique dédiés. Les Halls A et C sont chacun équipés de deux spectromètres à bras s'étendant vers l'extérieur de la cible qui tourne autour d'elle en fonction de l'angle des particules mesurées. Le détecteur CLAS était situé dans le Hall B et avait une plus grande accptance. Il était capable d'identifier et de mesurer plusieurs particules à l'état final avec une luminosité de l'ordre de 10^{34} cm^{-2}s^{-1}.

Le détecteur CLAS était adapté pour couvrir une large gamme de mesures. Afin de reconstituer les particules, des informations clés sont obtenues à partir de différents détecteurs (voir figure Fr.6) :

- Les trajectoires des particules chargées sont obtenues à partir des chambres à dérives (DC) situées à l'intérieur d'un champ magnétique généré par un aimant supraconducteur de forme toroïdale ;
- Les énergies des électrons, des pions et des photons peuvent être mesurés avec les calorimètres électromagnétiques (EC) ;
- Lorsque les deux valeurs précédentes ne suffisent pas à dissocier le type de particules entre deux candidats (par exemple entre un électron et un pion négatif), les compteurs Cherenkov (CC) peuvent aider à les distinguer ;

- Les compteurs à scintillateur (SC) sont situés au-delà des chambres à dérive et offrent une couverture similaire. Ils mesurent précisément le temps d'arrivée des particules au détecteur, et permettent l'identification de différents hadrons (π, K et p) lorsque l'information obtenue est corrélée avec les impulsions obtenues par les DCs.

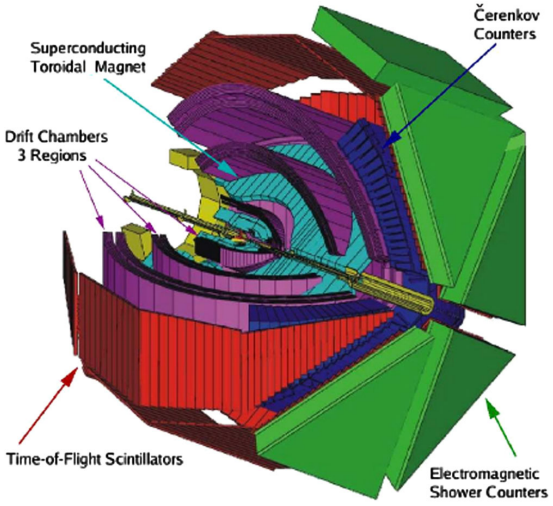

FIGURE FR.6 – Diagramme du détecteur CLAS.

Une cible polarisée à l'ammoniac (NH_3) a été ajoutée à l'appareil expérimental afin de mesurer les événements DVCS à partir de protons polarisés longitudinalement. Les photons des évènements DVCS émis à petits angles sont mesurés à l'aide du calorimètre interne (IC) situé en aval de la cible et proche du faisceau.

Analyse

L'expérience eg1-dvcs a pris des données de janvier à septembre 2009 en utilisant la cible NH_3. Le but de l'expérience initiale étant de mesurer la réaction DVCS sur des protons polarisés, 10% des données ont été prises sur une cible de carbone afin d'estimer le fond d'azote. Cette analyse applique les mêmes coupures utilisées par l'analyse du proton afin d'identifier les particules de l'état final [68].

Une fois les évènements candidats du DVCS identifiés, une correction de l'impulsion est appliquée ainsi qu'une série de coupures garantissant que la cinématique des événements est cohérente avec DVCS, et supprime également les événements de fond tels que les résonances hadroniques.

En dernier lieu, les événements DVCS sont sélectionnés en appliquant des coupures sur un ensemble de variables d'exclusivité. Puisque toutes les particules finales sont mesurées, la conservation de l'impulsion et de l'énergie doit être respectée. Par conséquent, chaque variable a une valeur attendue qui servira de point de départ pour déterminer les coupures assurant l'exclusivité de la réaction.

Un total de sept variables d'exclusivité est utilisé afin de d'assurer l'exclusivité de la réaction DVCS : $MM_X^2(ep)$, $MM_X^2(e\gamma)$, $MM_X^2(ep\gamma)$, $p_{\perp,X}$, l'énergie manquante, la coplanarité $\Delta\phi$ et l'angle du cône $\theta_{\gamma,epX}$. La coplanarité est défini comme l'angle entre les plans $\left(\vec{P}_p, \vec{P}_\gamma\right)$ et $\left(\vec{P}_p, \vec{P_{\gamma^*}}\right)$ qui doit être égal à zéro pour les événements DVCS. L'angle de cône $\theta_{\gamma,epX}$ est l'angle entre le photon reconstruit, calculé en utilisant l'électron et le proton mesurés, et le photon détecté. Pour un événement DVCS, $\theta_{\gamma,epX}$ doit être aussi égal à zéro.

Afin d'isoler les événements d'azote des données NH_3, les événements d'hydrogène doivent être identifiés et soustraits. La même procédure que l'analyse originale du DVCS sur les protons polarisés est appliqué. Avant de soustraire les événements hydrogène des données NH_3, une étude pour déterminer les coupures d'exclusivité sur les données carbone a été réalisée (voir figure Fr.7). Les données carbone offrent deux avantages : il n'y a pas de protons dans l'échantillon et le carbone est un noyau de taille similaire à l'azote. Par conséquent, les coupes d'exclusivité du carbone peuvent être appliquées ultérieurement à l'azote.

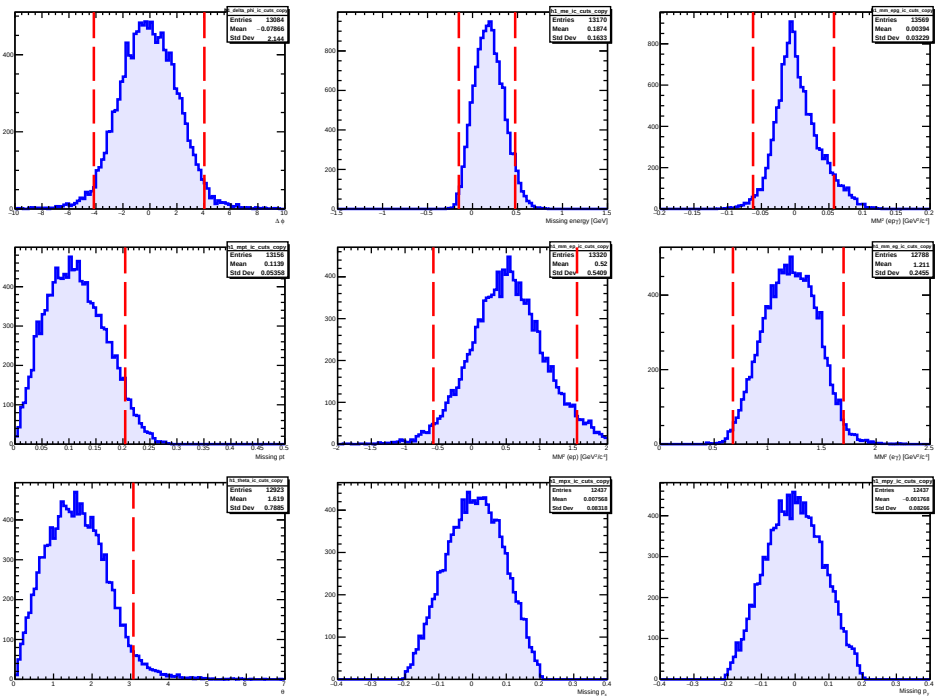

FIGURE FR.7 – Distributions des variables d'exclusivité des évènements DVCS incohérents sur le carbone. Chaque distribution montre une variable avec toutes les coupures d'exclusivité sauf celle tracée (la ligne rouge est la coupure pour la variable tracée).

Les événements hydrogène doivent être supprimés des données NH_3. Ce processus sera effectué en utilisant l'ensemble de coupures d'exclusivité de l'hydrogène précédemment introduit. Les coupures hydrogène sont calculées en utilisant les résultats d'ajustements gaussiens sur les variables d'exclusivité et en sélectionnant des événements à moins de 3σ. Cependant, les événements hydrogène pourraient encore se situer au-delà de la coupure à 3σ. Afin d'éliminer la majeure partie de la con-

tamination de l'hydrogène dans les données, les coupures hydrogène sont étudiées à différents sigma sur les données NH_3 avec les coupures d'exclusivité du carbone appliquées (voir figure Fr.8). La soustraction des évènements hydrogène à 5σ a grandement supprimé le pic d'hydrogène et est adoptée pour cette analyse.

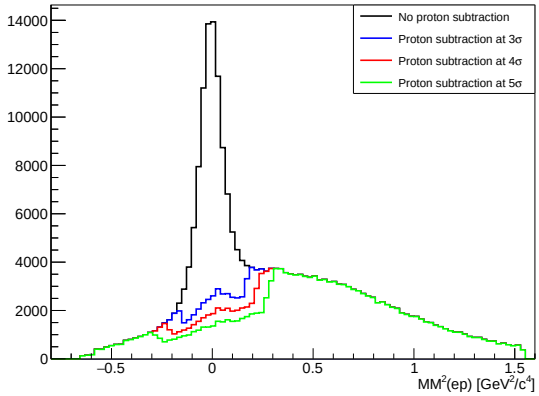

FIGURE FR.8 – Distribution $MM_X^2(ep)$ des données NH_3 avec les coupures d'exclusivité du carbone. Les lignes colorées représentent les différentes valeurs du σ utilisé pour soustraire les évènements hydrogène.

En utilisant les coupes d'exclusivité du carbone comme point de départ et après plusieurs itérations, les événements d'azote sont maintenus à moins de 2 écarts-types de la moyenne des distributions de chaque variable d'exclusivité (voir figure Fr.9).

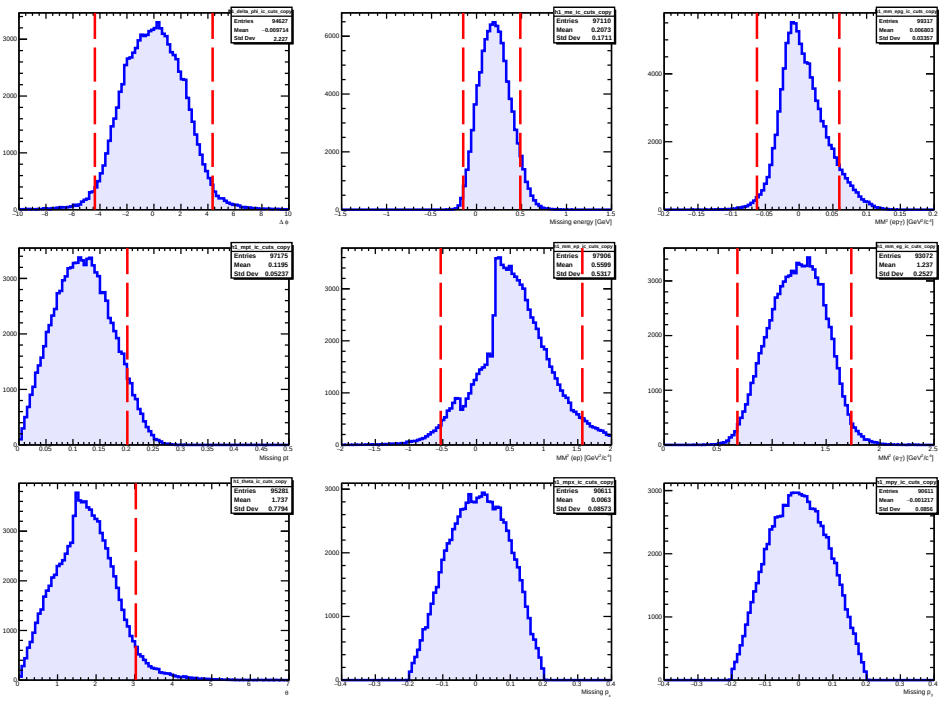

FIGURE FR.9 – Distributions des variables d'exclusivité des évènements DVCS incohérent sur l'azote. Chaque distribution montre une variable avec toute les coupures d'exclusivité sauf celle tracée (la ligne rouge est la coupure pour la variable tracée).

Résultats

Nous extrayons les BSAs pour différentes valeurs de Q^2 , x_B et -t. En raison de notre statistique limitée, chaque distribution Q^2 , x_B et -t sera divisée en 8 bins, chacun contenant à peu près le même nombre d'événements.

Une BSA, aussi noté A_{LU}, est définie comme :

$$A_{\mathrm{LU}} = \frac{1}{P_B}\frac{N^+ - N^-}{N^+ + N^-} \tag{5.4}$$

où P_B est la polarisation moyenne du faisceau d'électrons et N est le nombre d'événements pour chaque configuration d'hélicité du faisceau (positive ou négative). L'analyse proton eg1-dvcs a calculé la polarisation du faisceau à l'aide du polarimètre Hall B Møller.

La figure Fr.11 montre les BSAs de DVCS incohérent sur l'azote pour les differents bins en Q^2. Chaque bin est ajusté en utilisant la formule suivante : $A_{\mathrm{LU}} = \frac{\alpha \sin(\phi)}{1 + \beta \cos(\phi)}$

L'ajustement des données, en utilisant l'équation ci-dessus, permet d'extraire les A_{LU} à $\phi = 90^\circ$ pour chaque bin dans Q^2, x_B et -t. Dans la figure Fr.10, les $A_{\mathrm{LU}}(90^\circ)$ - également appelées amplitudes des BSAs - sont comparées à l'analyse DVCS incohérent sur ^{4}He. La valeur moyenne des amplitudes est obtenue en ajustant linéairement chaque résultat, et les amplitudes d'azote sont environ 30% plus petites que les amplitudes d'hélium-4. Le nombre d'événements azote est également supérieur au nombre d'événements hélium-4, ce qui se reflète dans des bins plus fins avec des barres d'erreur plus petites.

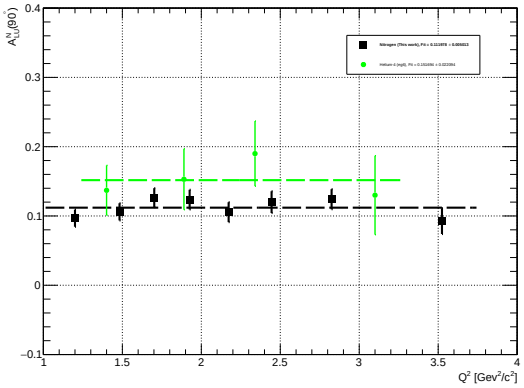

FIGURE FR.10 – Les amplitudes des asymétries A_{LU} (à $\phi = 90^\circ$) en fonction de Q^2. Les points noirs sont les évènements azotes et les points verts sont les évènements hélium-4.

Les résultats de l'expérience EMC ont démontré un effet du milieu nucléaire sur la structure des nucléons liés. En utilisant les BSAs d'événements DVCS, un test similaire peut être effectué en utilisant le rapport du nucléon lié (azote) et du nucléon libre

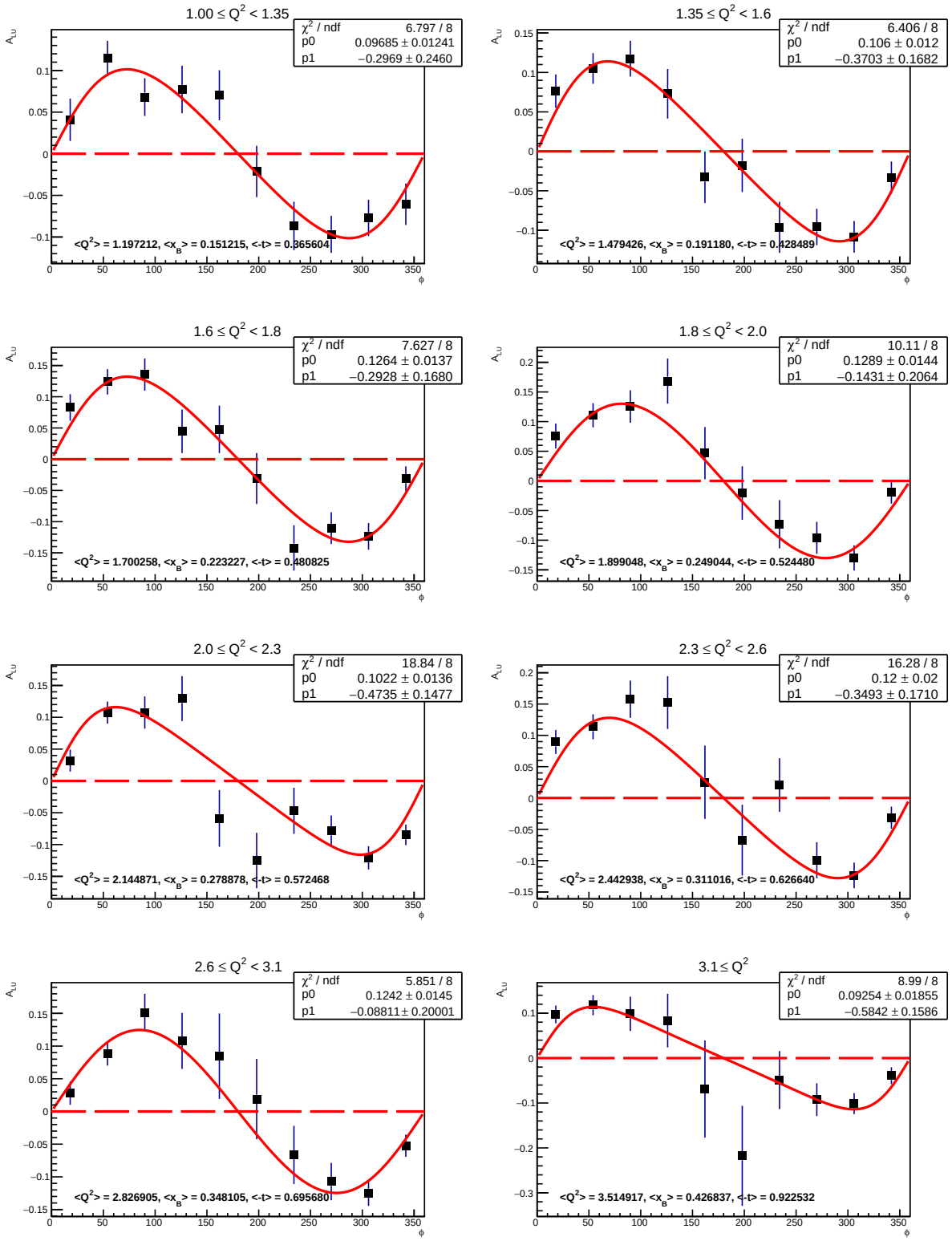

FIGURE FR.11 – A_{LU} d'évènements DVCS incohérent azote en fonction de ϕ et pour 8 bins en Q^2. Les lignes bleues sont les erreurs statistiques, et la courbe rouge est la courbe ajustée aux données.

(hydrogène). L'expérience eg1-dvcs ayant permis de mesurer la BSA sur l'hydrogène et l'azote, le rapport $A_{LU}^{A}/A_{LU}^{p}(90^{\circ})$ peut être obtenu sans aucune correction supplémentaire. Tout d'abord, les BSAs de l'hydrogène sont extraits en utilisant le même *binning* que l'analyse d'azote. Enfin, les ratios sont calculés et sont présentés dans la figure Fr.12. Ces rapports sont également comparés aux résultats DVCS sur l'hélium-4.

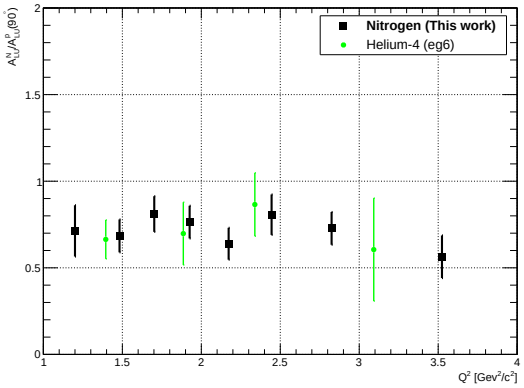

FIGURE FR.12 – Rapport $A_{LU}^{A}/A_{LU}^{p}(90^{\circ})$ en fonction de Q^2. Les points noirs sont les évènements azotes et les points verts sont les évènements hélium-4.

Comparé aux simples amplitudes montrées précédemment, les points du rapport généralisé EMC entre l'azote et l'hélium sont plus proches. L'une des raisons qui nécessiterait une étude plus approfondie pour expliquer ce comportement est liée aux données du proton libre utilisé pour calculer les rapports. Le résultat de l'hélium-4 a utilisé une interpolation des données publiées de l'expérience CLAS *e1-dvcs2*, alors que cette analyse a utilisé les données de la même expérience.

L'effet EMC montre une corrélation entre la valeur de pente des rapports EMC et la densité de noyau. Une corrélation similaire est trouvée en comparant la valeur moyenne des amplitudes de l'asymétrie en fonction de la densité exprimée par $A^{-1/3}$ (voir figure Fr.13). Au fur et à mesure que $A^{-1/3}$ augmente, l'amplitude des BSA augmente également. Cette observation met en évidence un effet de type EMC dans le rapport des asymétries DVCS entre le nucléon lié et le proton libre, et offre une nouvelle façon d'étudier l'impact du milieu nucléaire sur le nucléon lié.

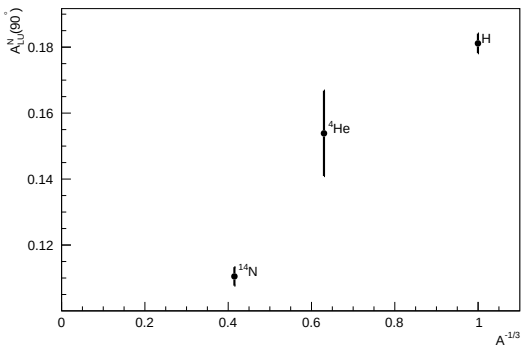

FIGURE FR.13 – Valeurs moyennes des amplitudes A_{LU}^{A} en fonction de la densité nucléaire $A^{-1/3}$.

Conclusion

L'effet EMC a révélé que notre compréhension actuelle de la structure des nucléons liés est incomplète. Après 35 ans d'expérimentations et de travaux théoriques, l'effet EMC n'est toujours pas résolu. Cependant, un certain nombre de programmes expérimentaux ont mesuré cet effet sur différents noyaux et ont trouvé une corrélation entre la densité nucléaire et la force de l'effet EMC. Le cadre des GPDs nucléaires - via des mesures DVCS nucléaires - est l'une des nouvelles approches utilisées pour étudier le milieu nucléaire et son effet sur les nucléons. Ce manuscrit a présenté les mesures de DVCS incohérent sur l'azote à l'aide du détecteur CLAS du *Jefferson Laboratory*. L'analyse a été effectuée en utilisant les données NH_3 qui ont été initialement prises pour mesurer le DVCS sur des protons polarisés. Bien que le canal proton fût analysé et publié, le canal azote n'a pas été exploité.

Une revue expérimentale et théorique de la diffusion lepton-nucléon a été faite en mettant l'accent sur l'effet EMC et le DVCS. Un bref aperçu de l'accélérateur et du dispositif expérimental a également été présenté. L'analyse est divisée en trois parties principales : l'identification des particules à l'état final a été réalisée, suivie de la détermination des coupes assurant l'exclusivité du procédé DVCS, et enfin l'extraction des BSAs. Les résultats de BSA pour l'azote sont ensuite comparés aux résultats publiés pour l'hélium-4.

Les BSAs de l'azote extraites montrent des amplitudes plus faibles que celles de l'hélium-4. Ces deux résultats ont également été comparés aux résultats des protons libres, et les valeurs moyennes des amplitudes des BSAs nucléaires se sont avérées inférieures à celles du proton libre. On remarque également une corrélation entre la densité de noyaux et l'amplitude des BSAs : à mesure que la densité nucléaire diminue, l'amplitude de la BSA diminue également. Ce résultat confirme un nouvel effet nucléaire et donne une première indication sur sa dépendance en A.

Dans un avenir proche, ce programme expérimental sera étendu au *Jefferson Laboratory* qui a récemment doublé l'énergie de son faisceau d'électrons pour atteindre 12 GeV. Cette augmentation d'énergie est accompagnée par la mise à niveau du détecteur CLAS, désormais appelé CLAS12. Le programme CLAS12 propose un certain nombre de mesures visant à étudier le DVCS nucléaire. Ces futurs résultats bénéficieront de la luminosité plus élevée de CLAS12, ainsi qu'une couverture cinématique étendue offerte par l'augmentation de l'énergie du faisceau.

Bibliography

[1] R. Frisch and O. Stern. Über die magnetische Ablenkung von Wasserstoffmolekülen und das magnetische Moment des Protons. I. *Zeitschrift für Physik*, 85(1):4–16, Jan 1933. 13

[2] R. Hofstadter. Electron Scattering and Nuclear Structure. *Rev. Mod. Phys.*, 28:214–254, Jul 1956. 13

[3] R.P. Feynman. The behavior of hadron collisions at extreme energies. *Conf. Proc. C*, 690905:237–258, 1969. 15

[4] R. Hofstadter and R. W. McAllister. Electron Scattering from the Proton. *Phys. Rev.*, 98:217–218, Apr 1955. 17, 18

[5] M. N. Rosenbluth. High Energy Elastic Scattering of Electrons on Protons. *Phys. Rev.*, 79:615–619, Aug 1950. 17

[6] E. B. Hughes, T. A. Griffy, M. R. Yearian, and R. Hofstadter. Neutron form factors from inelastic electron-deuteron scattering. *Phys. Rev.*, 139:B458–B471, Jul 1965. 18

[7] Curtis G. Callan, Jr. and David J. Gross. High-energy electroproduction and the constitution of the electric current. *Phys. Rev. Lett.*, 22:156–159, 1969. 21

[8] Yuri L. Dokshitzer. Calculation of the Structure Functions for Deep Inelastic Scattering and e+ e- Annihilation by Perturbation Theory in Quantum Chromodynamics. *Sov. Phys. JETP*, 46:641–653, 1977. 21

[9] P. A. Zyla et al. Review of Particle Physics. *PTEP*, 2020(8):083C01, 2020. 22, 23

[10] J.J. Aubert, G. Bassompierre, K.H. Becks, et al. The ratio of the nucleon structure functions F2N for iron and deuterium. *Physics Letters B*, 123(3):275 – 278, 1983. 23

[11] S. Malace, D. Gaskell, D. W. Higinbotham, and I. C. Cloët. The challenge of the EMC effect: Existing data and future directions. *International Journal of Modern Physics E*, 23(08):1430013, 2014. 24, 112

[12] J. Seely, A. Daniel, D. Gaskell, et al. New Measurements of the European Muon Collaboration Effect in Very Light Nuclei. *Phys. Rev. Lett.*, 103:202301, Nov 2009. 24, 25, 26

[13] P. Amaudruz, M. Arneodo, A. Arvidson, et al. A re-evaluation of the nuclear structure function ratios for D, He, 6Li, C and Ca. *Nuclear Physics B*, 441(1):3 – 11, 1995. 24, 28, 29, 30

[14] J. Gomez, R. G. Arnold, P. E. Bosted, et al. Measurement of the A dependence of deep-inelastic electron scattering. *Phys. Rev. D*, 49:4348–4372, May 1994. 24, 25, 28, 29, 30

[15] A. Airapetian, N. Akopov, Z. Akopov, et al. Erratum to: "Nuclear effects on R=σ_L/σ_T in deep-inelastic scattering": [Phys. Lett. B 475 (2000) 386–394]. *Physics Letters B*, 567(3):339 – 346, 2003. 24

[16] M. Arneodo, A. Arvidson, B. Badelek, et al. The structure function ratios F2C/F2D and F2C/F2D at small x. *Nuclear Physics B*, 441(1):12 – 30, 1995. 24

[17] M. Arneodo, A. Arvidson, B. Badeek, et al. The A dependence of the nuclear structure function ratios. *Nuclear Physics B*, 481(1):3 – 22, 1996. 24

[18] M. Arneodo, A. Arvidson, J.J. Aubert, et al. Measurements of the nucleon structure function in the range 0.002 < x < 0.17 and 00.2 < Q2 < 8 GeV2 in deuterium, carbon and calcium. *Nuclear Physics B*, 333(1):1 – 47, 1990. 24

[19] A. Bodek, N. Giokaris, W. B. Atwood, et al. Electron Scattering from Nuclear Targets and Quark Distributions in Nuclei. *Phys. Rev. Lett.*, 50:1431–1434, May 1983. 24

[20] A.C. Benvenuti, D. Bollini, G. Bruni, et al. Nuclear effects in deep inelastic muon scattering on deuterium and iron targets. *Physics Letters B*, 189(4):483 – 487, 1987. 24, 28, 29, 30

[21] John Arrington, Aji Daniel, Donal Day, et al. A detailed study of the nuclear dependence of the EMC effect and short-range correlations. *Phys. Rev. C*, 86:065204, 2012. 25

[22] N. Fomin, J. Arrington, R. Asaturyan, et al. New Measurements of High-Momentum Nucleons and Short-Range Structures in Nuclei. *Phys. Rev. Lett.*, 108:092502, Feb 2012. 26, 27

[23] O. Hen, D. W. Higinbotham, G. A. Miller, et al. The EMC Effect and High Momentum Nucleons in Nuclei. *International Journal of Modern Physics E*, 22(07):1330017, 2013. 26, 27

[24] S. V. Akulinichev, S. Shlomo, S. A. Kulagin, and G. M. Vagradov. Lepton-Nucleus Deep-Inelastic Scattering. *Phys. Rev. Lett.*, 55:2239–2241, Nov 1985. 28

[25] P R Norton. The EMC effect. *Reports on Progress in Physics*, 66(8):1253–1297, jul 2003. 28

[26] J Ashman, B Badelek, Guenter Baum, et al. A measurement of the ratio of the nucleon structure function in copper and deuterium. *Zeitschrift für Physik C Particles and Fields*, 57(2):211–218, 1993. 28, 29, 30

[27] GL Li, KF Liu, and GE Brown. Role of nuclear binding in the emc effect. *Physics Letters B*, 213(4):531–536, 1988. 28

[28] M. Ericson and A.W. Thomas. Pionic corrections and the EMC enhancement of the sea in iron. *Physics Letters B*, 128(1):112 – 116, 1983. 28

[29] D. M. Alde, H. W. Baer, T. A. Carey, et al. Nuclear dependence of dimuon production at 800 GeV. *Phys. Rev. Lett.*, 64:2479–2482, May 1990. 29

[30] C. A. Aidala et al. The SeaQuest Spectrometer at Fermilab. *Nucl. Instrum. Meth. A*, 930:49–63, 2019. 29

[31] R P Bickerstaff and A W Thomas. The EMC effect-with emphasis on conventional nuclear corrections. *Journal of Physics G: Nuclear and Particle Physics*, 15(10):1523–1569, oct 1989. 29

[32] Daniel de Florian, Rodolfo Sassot, Marco Stratmann, and Werner Vogelsang. Extraction of Spin-Dependent Parton Densities and Their Uncertainties. *Phys. Rev. D*, 80:034030, 2009. 29, 35

[33] CE Carlson and TJ Havens. Quark distributions in nuclei. *Physical Review Letters*, 51(4):261, 1983. 29, 30

[34] D F Geesaman, K Saito, and A W Thomas. The Nuclear EMC Effect. *Annual Review of Nuclear and Particle Science*, 45(1):337–390, 1995. 29

[35] KE Lassila and UP Sukhatme. The emc effect at all x in the quark cluster model. *Physics Letters B*, 209(2-3):343–346, 1988. 30

[36] F.E. Close, R.G. Roberts, and G.G. Ross. The effect of confinement size on nuclear structure functions. *Physics Letters B*, 129(5):346 – 350, 1983. 29

[37] A. V. Kotikov, B. G. Shaikhatdenov, and Pengming Zhang. Application of the rescaling model at small Bjorken x values. *Phys. Rev. D*, 96:114002, Dec 2017. 30

[38] Francis Edwin Close, RL Jaffe, RG Roberts, and Graham G Ross. Change of confinement scale in nuclei: Predictions for structure functions confront electroproduction data. *Physical Review D*, 31(5):1004, 1985. 30

[39] A. V. Radyushkin. Nonforward parton distributions. *Phys. Rev. D*, 56:5524–5557, Nov 1997. 31

[40] A.V. Belitsky, D. Müller, and A. Kirchner. Theory of deeply virtual compton scattering on the nucleon. *Nuclear Physics B*, 629(1):323 – 392, 2002. 31, 37, 39

[41] A. V. Belitsky and D. Müller. Exclusive electroproduction revisited: Treating kinematical effects. *Phys. Rev. D*, 82:074010, Oct 2010. 31

[42] John C. Collins and Andreas Freund. Proof of factorization for deeply virtual compton scattering in qcd. *Phys. Rev. D*, 59:074009, Feb 1999. 31

[43] Xiang-Dong Ji and Jonathan Osborne. One loop corrections and all order factorization in deeply virtual Compton scattering. *Phys. Rev. D*, 58:094018, 1998. 31

[44] Mohammad Hattawy. Deeply Virtual Compton Scattering off Helium-4, Thèse de doctorat dirigée par M. Guidal. *Paris XI, PhD thesis*, 2015. 31, 40, 79, 87, 103

[45] M. Diehl. Generalized parton distributions. *Phys. Rept.*, 388:41–277, 2003. 32, 33

[46] Michel Guidal, Hervé Moutarde, and Marc Vanderhaeghen. Generalized Parton Distributions in the valence region from Deeply Virtual Compton Scattering. *Rept. Prog. Phys.*, 76:066202, 2013. 34, 36, 37, 38

[47] Xiang-Dong Ji. Off forward parton distributions. *J. Phys. G*, 24:1181–1205, 1998. 34

[48] Xiang-Dong Ji. Gauge-Invariant Decomposition of Nucleon Spin. *Phys. Rev. Lett.*, 78:610–613, 1997. 34

[49] Xiang-Dong Ji. Deeply virtual Compton scattering. *Phys. Rev. D*, 55:7114–7125, 1997. 35

[50] Matthias Burkardt. Impact parameter space interpretation for generalized parton distributions. *Int. J. Mod. Phys. A*, 18:173–208, 2003. 35

[51] Raphael Dupre, Michel Guidal, and Marc Vanderhaeghen. Tomographic image of the proton. *Phys. Rev. D*, 95(1):011501, 2017. 35

[52] A. V. Belitsky and A. V. Radyushkin. Unraveling hadron structure with generalized parton distributions. *Phys. Rept.*, 418:1–387, 2005. 36

[53] Alessandro Bacchetta, Umberto D'Alesio, Markus Diehl, and C. Andy Miller. Single-spin asymmetries: The Trento conventions. *Phys. Rev. D*, 70:117504, 2004. 37

[54] A. Airapetian, N. Akopov, Z. Akopov, et al. Nuclear-mass dependence of azimuthal beam-helicity and beam-charge asymmetries in deeply virtual compton scattering. *Phys. Rev. C*, 81:035202, Mar 2010. 40, 41, 42

[55] R. Dupré et al. Measurement of deeply virtual Compton scattering off Helium-4 with CLAS at Jefferson Lab. 2021. 41, 42

[56] S. Liuti and S. K. Taneja. Microscopic description of deeply virtual compton scattering off spin-0 nuclei. *Phys. Rev. C*, 72:032201, Sep 2005. 41, 42

[57] Sara Fucini, Sergio Scopetta, and Michele Viviani. Incoherent deeply virtual Compton scattering off ^{4}He. *Phys. Rev. C*, 102:065205, 2020. 41

[58] Sara Fucini, Sergio Scopetta, and Michele Viviani. Catching a glimpse of the parton structure of the bound proton. *Phys. Rev. D*, 101:071501, Apr 2020. 41, 42

[59] V. Guzey. Neutron contribution to nuclear deeply virtual compton scattering asymmetries. *Phys. Rev. C*, 78:025211, Aug 2008. 42

[60] Christoph W Leemann, David R Douglas, and Geoffrey A Krafft. The continuous electron beam accelerator facility: Cebaf at the jefferson laboratory. *Annual Review of Nuclear and Particle Science*, 51(1):413–450, 2001. 44

[61] Reza Kazimi, Kevin Beard, Jay Benesch, et al. Cebaf injector achieved world's best beam quality for three simultaneous beam with a wide range of bunch charges. Technical report, Thomas Jefferson National Accelerator Facility, Newport News, VA (US), 2004. 44

[62] Bernhard A Mecking, G Adams, S Ahmad, et al. The cebaf large acceptance spectrometer (clas). *Nuclear Instruments and Methods in Physics Research Section A: Accelerators, Spectrometers, Detectors and Associated Equipment*, 503(3):513–553, 2003. 45, 47, 48, 49, 55

[63] MD Mestayer, DS Carman, B Asavapibhop, et al. The clas drift chamber system. *Nuclear Instruments and Methods in Physics Research Section A: Accelerators, Spectrometers, Detectors and Associated Equipment*, 449(1-2):81–111, 2000. 49, 50

[64] M Amarian, Geram Asryan, Kevin Beard, et al. The clas forward electromagnetic calorimeter. *Nuclear Instruments and Methods in Physics Research Section A: Accelerators, Spectrometers, Detectors and Associated Equipment*, 460(2-3):239–265, 2001. 50, 51

[65] G Adams, V Burkert, R Carl, et al. The clas cherenkov detector. *Nuclear Instruments and Methods in Physics Research Section A: Accelerators, Spectrometers, Detectors and Associated Equipment*, 465(2-3):414–427, 2001. 51, 52

[66] ES Smith, T Carstens, J Distelbrink, et al. The time-of-flight system for clas. *Nuclear Instruments and Methods in Physics Research Section A: Accelerators, Spectrometers, Detectors and Associated Equipment*, 432(2-3):265–298, 1999. 52, 53

[67] CD Keith, M Anghinolfi, M Battaglieri, et al. A polarized target for the clas detector. *Nuclear Instruments and Methods in Physics Research Section A: Accelerators, Spectrometers, Detectors and Associated Equipment*, 501(2-3):327–339, 2003. 54, 55

[68] A. Biselli, S. Pisano, G. Smith, et al. Measurements of single- and double-spin asymmetries for deeply virtual compton scattering with a polarized electron beam and a longitudinally polarized proton target. *CLAS Analysis Note 2014-104*, 2014. 57, 69, 75, 76, 79, 80, 81, 82, 83, 84, 99, 115

[69] A Kim. Good file list from file rate study. *EG1-DVCS Technical Note 22*, 2012. 59

[70] P Bosted and A Kim. Beam(x, y)and target center z from raster adcs. *EG1-DVCS Technical Note 2*, 2010. 59

[71] P Bosted. Fiducial cuts based on ic shielding. *EG1-DVCS Technical Note 17*, 2011. 65

[72] Raphaël Dupré, Michel Guidal, Silvia Niccolai, and Marc Vanderhaeghen. Analysis of Deeply Virtual Compton Scattering Data at Jefferson Lab and Proton Tomography. *Eur. Phys. J. A*, 53(8):171, 2017. 99, 103

université PARIS-SACLAY

ÉCOLE DOCTORALE
Particules, hadrons, énergie et noyau : instrumentation, imagerie, cosmos et simulation (PHENIICS)

Titre : Étude de la structure du nucléon avec CLAS à Jefferson Lab : Diffusion Compton Profondément Virtuelle sur l'azote

Mots clés : Diffusion d'électrons, Quarks, GPDs, DVCS, Réactions exclusives, Structure du nucléon

Résumé : L'une des plus importantes questions non résolues de la chromodynamique quantique (QCD) est la formation des noyaux et la nature de l'interaction nucléon-nucléon à partir de ses degrés de libertés fondamentaux : les quarks et les gluons. En particulier, la modification de la structure en quark des nucléons dans le milieu nucléaire (effet EMC) est toujours un mystère plus de 30 ans après sa découverte. Nous proposons d'étudier ce problème à l'aide du formalisme des distributions de partons généralisées (GPD). Les GPDs sont des fonctions de structure corrélant l'impulsion longitudinale et la position transversale des partons. Les GPDs sont accessibles via des réactions exclusives comme la diffusion Compton profondément virtuelle (DVCS). L'étude du DVCS dans les noyaux est une nouvelle façon d'étudier les interactions entre les quarks dans le milieu nucléaire. Le DVCS sur l'helium-4 a été mesuré au Jefferson Lab (aux États-Unis), utilisant le détecteur CLAS et un faisceau d'électrons polarisé à 6 GeV. Ce travail approfondit notre connaissance des noyaux en analysant la réaction DVCS incohérent sur l'azote. Les données utilisées sont celles de l'expérience CLAS qui ont mesuré avec succès le processus DVCS sur des protons polarisés et utilisant une cible polarise d'ammoniac (NH_3). Ce travail détaillera la procédure utilisée pour soustraire le background proton de la cible d'ammoniac afin d'analyser le canal DVCS incohérent sur l'azote. Les asymétries faisceau-spin du processus DVCS incohérent sur l'azote seront présentées et comparées aux résultats de l'helium-4.

Title : Nucleon structure studies with CLAS at Jefferson Lab : Deeply Virtual Compton Scattering on nitrogen

Keywords : Electron scattering, Quarks, GPDs, DVCS, Exclusive reactions, Nucleon structure

Abstract : One of the most important unresolved questions of quantum chromo-dynamic (QCD) is the formation of nuclei and the nature of the nucleon-nucleon interaction in term of fundamental degrees of freedom, i.e. quarks and gluons. In particular, the modification of the nucleon structure function in the nuclear medium (EMC effect) is still a mystery 30 years after its discovery. We propose to study this question using the Generalized Parton Distribution (GPD) framework. The GPDs are structure functions correlating the longitudinal momentum and transverse position of partons. The GPDs are accessible through exclusive reactions such as the Deeply Virtual Compton Scattering (DVCS). The study of DVCS on nuclei is a new way to study the interactions between quarks in the nuclear medium. DVCS on helium-4 was measured at Jefferson Lab (USA) using the CLAS detector and the 6 GeV polarized electron beam. This work extends our knowledge of nuclei by analyzing the incoherent DVCS process on nitrogen. We used the CLAS experiment data which successfully measured the DVCS process on polarized protons, using an ammonia (NH_3) polarized target. This work will detail the procedure used to subtract the proton background from the ammonia target in order to analyze the incoherent DVCS channel on nitrogen. Beam-spin asymmetries of the incoherent DVCS process on nitrogen will be presented et compared to the helium-4 results.

Maison du doctorat de l'Université Paris-Saclay
2ème étage aile ouest, Ecole normale supérieure Paris-Saclay
4 avenue des Sciences,
91190 Gif sur Yvette, France